EUROPEAN ORGANIZATION FOR NUCLEAR RESEARCH

MASS SPECTROSCOPY OF HEAVY BOSONS

AND

SPIN-PARITY ANALYSIS WITH A NEW INSTRUMENT

Inaugural Dissertation
for the Acquisition of the
Degree of Doctor of Science,
presented to the
Faculty of Science of the University of Bern
by

Peter Schübelin,
Belp

Accepted by the Faculty of Science
at the request of Prof. Dr. J. Geiss,
based on the assessment of Prof. Dr. Ch. Peyrou

Dean: Prof. Dr. M. Lüscher

12 December 1967.

Printed at CERN, Geneva 1968

UNIV.
LEIDEN
BIBL.

To the late G.E. Chikovani

whose guidance and friendship

made this work possible

Digitized by the Internet Archive
in 2026

https://archive.org/details/IA41546623_0048

ABSTRACT

The boson mass spectrum has been investigated in the reaction $\pi^- + p \rightarrow p + X^-$ in the region $0.5 < M_X < 2.5$ GeV by means of the CERN Missing Mass Spectrometer, using the Jacobian peak method. Three new heavy bosons referred to as S, T and U mesons (M_S = 1929 MeV, M_T = 2195 MeV, M_U = 2382 MeV) have been found. Their experimental widths are equal to the experimental resolution, of the order of 25 MeV.

The mass region of the R meson has been investigated with large statistics. It is shown that the R meson is split into three, perhaps four peaks (M_{R_1} = 1630 MeV, M_{R_2} = 1700 MeV, M_{R_3} = 1748 MeV, M_{R_4} = 1830 MeV) each of them with width equal to the experimental resolution.

The A_2 meson, first observed in bubble chambers, has been measured with high statistics. It has been found to be split into two peaks of equal width and height in all samples of good experimental resolution (16 to 18 MeV), whilst no splitting has been seen in samples with larger resolution. In order to determine the still controversial spin-parity of the A_2 meson, a novel additional instrument to the Missing Mass Spectrometer has been developed and built: a digitized wide-gap wire chamber system with dimensions 1.5×1.5 m^2. The advantages of the new instrument are: excellent multiparticle efficiency, good measuring precision, and the possibility of being operated in an on-line experiment. With this instrument, an analysis of decay particles was possible. The Dalitz plot of the A_2 mass region favours the 2^+ spin-parity assignment over 2^- and 1^+.

* * *

CONTENTS

		Page
Section 1 : MISSING-MASS SPECTROMETER		1
1.1	Basic method	1
1.2	Instrumentation and experimental set-up	2
1.3	Summary of the results	4
1.4	Evidence for a two-peak structure in the A_2 meson	4
1.5	Evidence for structure in the R meson	7
1.6	Discovery of the heavy bosons (mass > $2m_{nucleon}$)	9
Section 2 : DEVELOPMENT OF A NOVEL SYSTEM FOR ANALYSIS OF DECAY PROPERTIES OF HEAVY BOSONS		13
2.1	Limitations of the MMS	13
2.2	Methods for J^P determination in $A_2^- \to \rho^0 \pi^-$	13
2.3	Novelties in our approach to the determination of J^P of the A_2	18
2.4	Theory of spark mechanism	20
2.5	Principles of operation of a wide-gap wire chamber	24
2.6	Construction and operation of a prototype chamber	24
2.7	Construction and tests of large-area chambers	26
2.8	The read-out	27
2.9	Read-out electronics	27
2.10	Multispark events	28
2.11	Definitions and track reconstruction	29
2.12	Technical results from a test-run of the boson spectrometer	31
2.13	Solutions to some technical difficulties in the development	33
Section 3 : DALITZ PLOT OF THE A_2 MESON REGION OBTAINED WITH THE NEW SYSTEM		34
3.1	Method	34
3.2	Experimental conditions	35
3.3	Selection of events	35
3.4	Spin-parity analysis	36
3.5	Biases	37
3.6	Conclusions	37
REFERENCES		39

1. MISSING-MASS SPECTROMETER

1.1 Basic method

In 1963, a new method was proposed[1] to investigate systematically the mass spectrum of charged bosons in the reaction

$$\underset{(1)}{\pi^-} + \underset{(2)}{p} \rightarrow \underset{(3)}{p} + \underset{(4)}{X^-} \qquad (1.1)$$

with high statistics and good mass resolution. The momentum p_1 of the incident pion with mass m_1 is known from beam settings. Particle 2, the proton with mass m_2, is the target particle, of which the momentum p_2 is zero. When the reaction has taken place, the outgoing proton has a momentum p_3 while flying away at a scattering angle θ_3 with respect to the beam direction. X^- is a boson resonance or a multipion system of mass m_4 and momentum p_4. In order to determine the effective mass of X^-, i.e. the missing-mass of the recoil proton, it is enough to measure its energy and momentum. The effective mass of the X^- is given by

$$M_{eff}(X^-) = [(E_1 + m_2 - E_3)^2 - p_1^2 - p_3^2 + 2p_1 p_3 \cdot \cos\theta_3]^{1/2} , \qquad (1.2)$$

where E_1 and E_3 are the energies of the incident pion and the recoil proton, respectively. From kinematics one sees that recoil protons are emitted in the lab. system only up to an angle θ_3^{max} which is determined by p_1 and m_4 (Fig. 1a). This angle θ_3^{max} is called the "Jacobian peak angle". Since the mass lines around the Jacobian peak angle are more or less flat, (Fig. 1b), a lab. angular distribution of recoil protons is equivalent to a mass spectrum of X^-. In other words, it is not necessary to have a very precise measurement of the proton momentum p_3.

As will be seen later, it is important to note that the angle θ_3^* in the c.m. system corresponding to the Jacobian peak angle θ_3^{max} lies around 170°, i.e. not far away from the backward direction

Though kinematics allow a very direct measurement of a mass spectrum, this is not yet sufficient to make an experiment feasible, since only 1% of all protons fall inside the Jacobian peak for isotropic distribution in the c.m. system.

Another effect very much enhances the kinematic peak, namely the mechanism of the peripheral resonance production. The production cross-section of X^- has been found to be an exponential of the form

$$\frac{d\sigma}{dt} = K \cdot e^{-a|t|} \qquad (1.3)$$

where t is the four-momentum transfer of the proton

$$t = (\underline{p_3} - \underline{p_2})^2$$

and the constant "a" is about equal to 8 $(GeV/c)^{-2}$ under our conditions. Since $|t|$ and $\cos \Theta^*$ are proportional, a strong forward emission of the X^- in the c.m. follows, which implies a strong backward emission of the recoil proton, e.g. into the Jacobian peak region (between 150°-180° under our conditions). This dynamical effect enhances the fraction of events in the Jacobian peak to 20%-30%, depending on p_1 and M_X (Fig. 2).

If we summarize the situation, we see that knowledge of the momentum of the incident pion, an identification of the recoil proton, a precise measurement of its angle, and a rough determination of its momentum interval allow us to determine the mass of X^-.

1.2 Instrumentation and experimental set-up

In Fig. 3, the experimental set-up of the CERN Missing-Mass Spectrometer (MMS) is shown[2]. The MMS has been in operation from 1964 until the end of 1966 at the CERN Proton Synchrotron at beam momenta p_1 = 3.0 GeV/c - 13.0 GeV/c exploring the mass region $0.5 < M_X < 2.5$ GeV.

The instrument consists of four parts:

- beam elements
- a telescope for the recoil proton
- a detector for the decay particles of X^-
- a data acquisition system with on-line computer.

1.2.1 Beam. Two hodoscopes H1 and H2, each consisting of five scintillators, define the direction of the incident particles. A Čerenkov counter Č between the two hodoscopes discriminates against incident particles other than pions (K^-,p^-).

1.2.2 Recoil proton. The direction of the recoil proton is measured by four sonic spark chambers SCI,...,SCIV with an angular resolution $\Delta\theta \simeq \pm 3$ mrad at $p_3 = 500$ MeV/c. The space between the chambers is filled with He bags to reduce multiple scattering of the proton. The momentum interval of the proton is defined by three large-area scintillators R_1, R_2, $\overline{R_3}$, requiring coincidence of R_1, R_2, and anticoincidence of $\overline{R_3}$. The space between R_2 and $\overline{R_3}$ is filled with five additional large-area scintillation counters subdividing the total momentum interval into five equal subintervals of 30 MeV/c width.

Furthermore, the velocity of the recoil proton is measured by the time-of-flight (TOF) method. A T-counter in front of the target defines time $t = 0$; R_1 and R_2 measure TOF 1 and TOF 2, respectively, in two independent circuits. An appropriate adjustment of the coincidence between T and R_1, R_2, $\overline{R_3}$ allows rejection of π's and K's.

1.2.3 Decay particles. An additional trigger condition requires at least one charged particle in a counter behind the target, called the V counter. In order to count the number of charged decay particles, a 72-element scintillator matrix (160 × 160 cm^2) is mounted behind the V-counter, covering a solid angle of ±20°. The matrix is not able to measure precise angular distributions, since it has a poor spacial precision (mean cell size equals 10 × 10 cm^2). On the other hand, it has an excellent time resolution, i.e. a small accidental background.

1.2.4 Data acquisition system and on-line computer. The information from the spark chambers and from all counters and hodoscopes is stored in fast scalers (25 Mc) and pattern units, respectively. After each event, 73 24-bit scalers (or equivalent) are transferred to an SDS 920 computer, which has a memory of 8 kilowords and a cycle of 8 μsec.

The transfer time equals about 600 μsec per event. The computer buffers the information and writes it onto magnetic tape, 15 events per record.

The system is capable of handling up to 15 events per PS burst (spill 250 msec) but in actual runs it was never saturated (maximum 10 events per burst).

In parallel the computer is sampling events, and performs different technical checks between the bursts. Statistics on the performance of the system can be written out on a paper-tape on request, and give detailed diagnostics on the technical behaviour of the set-up.

The magnetic tapes containing about 50000 events are analysed on a large CERN computer, the CDC 3800. In the last stage of the experiment, it was even possible to feed our data via a data link directly into the CERN CDC 6600; this machine performed a complete analysis on all the data, and certain results could be seen on a television screen situated inside the experimental area. Such a visual on-line output is seen in Fig. 4.

1.3 Summary of the results

The boson mass spectrum between 500 and 2500 MeV was measured with the described instrument using reaction (1.1).

The total spectrum, with background subtracted, is seen in Fig. 5[3]. In this thesis, only those parts of the spectrum where the author participated fully in the data-taking and the analysis will be described.

1.4 Evidence for a two-peak structure in the A_2 meson[4,5]

The total A_2 mass spectrum, obtained in six days of running in January 1967 is shown in Fig. 6. A Breit-Wigner fit to this data gives the parameters

$$M = 1.307\ (\pm\ 0.016)\ \text{GeV}$$

$$\Gamma = 0.090\ (\pm\ 0.015)\ \text{GeV}\ .$$

The experimental mass resolution Γ_{exp} (full width) depends strongly on p_3, as seen in Fig. 7. The resolution is best at the "Jacobian peak" [Γ_{exp} = 16 ($\pm$ 3) MeV at p_3 = 500 MeV/c]. We have therefore divided the total data in the A_2 region into five subsamples, one for each range interval, covering 30 MeV/c each. These are shown in Fig. 8.

Dips in the centre of the A_2 are seen in the best resolution samples, namely range intervals 3 and 4, the width of the dips being about equal to Γ_{exp}. A weaker effect is seen in range interval 2, and no effect in the intervals 1 and 5 where Γ_{exp} is substantially broader.

The two best resolution samples (range intervals 3 and 4) have been added in Fig. 9, in finer bins of $\Delta\theta = 0.1°$, corresponding to $\Delta M = 4.0$ MeV. A significant hole is seen at the centre of the A_2 peak, with a width again compatible with Γ_{exp}. Within statistics this effect behaves equally in the subsamples for A_2 decaying into $\rho^-\pi^0$ (i.e. one charged decay product) and A_2 decaying into $\rho^0\pi^-$ (i.e. three charged decay products).

Already in our earlier data[4], a dip in the centre of the A_2 meson had been observed (May 1965 and October 1965). These data, taken at $p_1 = 6$ and 7 GeV/c are shown in Fig. 10. Between these two earlier runs, the spectrometer, including the beam, has been completely dismantled and redesigned. In each run, the proton telescope was operated in a different way and at a different angle setting:

May 1965 (Fig. 10a): $p_1 = 6.0$ GeV/c "tapered absorber" and time-of-flight; $\theta = 55°$.

Oct. 1965 (Fig. 10b): $p_1 = 7.0$ GeV/c "flat absorber" and time-of-flight; $\theta = 52°$, new spark chambers.

The sum of our earlier data is shown in Fig. 10c. When fitted with a Breit-Wigner curve, we obtain the parameters:

$$M = 1.283\ (\pm\ 0.016)\ \text{GeV}$$

$$\Gamma = 0.099\ (\pm\ 0.015)\ \text{GeV}\ .$$

The addition of the new A_2 (Fig. 9) to the earlier A_2 spectrum (Fig. 10c) was done by centring the over-all A_2 peaks to their average central mass of 1.295 GeV, since the absolute value of the beam momentum p_1 was only known to ±2%, which is equivalent to ±16 MeV in mass. The total A_2 obtained in this way is shown in Fig. 11. A pronounced splitting is seen; the centre of the hole is at 1.297 GeV, the width of about 15 MeV being compatible with the resolution. The three lowest points are 6 standard deviations from the top.

We have fitted the data of Fig. 11 with several different hypotheses about the shape of the A_2 peak. The background has an experimentally known shape and an amplitude free to adjust itself within the experimental errors. Γ_{exp} has been folded into all fits.

1.4.1 <u>One peak.</u> A single Breit-Wigner curve of the form

$$A(M) = \frac{(M_0\Gamma)^{1/2}}{M_0^2 - M^2 - i\Gamma M_0} \; ; \qquad \Gamma = \frac{M_0}{M}\left(\frac{q}{q_0}\right)^{2\ell+1} \cdot \Gamma_0 \qquad (1.4)$$

(where q is the momentum of the ρ and π in the A_2 centre of mass, ℓ is the $\rho\pi$ angular momentum and was set to $\ell = 2$), with free centre value M_0 and width Γ_0 (i.e. two free parameters apart from the one for the height of the background). The resulting parameters are:

$$M_0 = 1.297\ (\pm\ 0.016)\ \text{GeV}$$

$$\Gamma_0 = 0.088\ (\pm\ 0.015)\ \text{GeV}\ ,$$

with a low confidence level $P\ (\chi^2) = 0.1\%$, taken in an interval of $\pm\ \Gamma/2$.

1.4.2 <u>Two independent peaks.</u> Two incoherent BW curves of the form used in Section 1.4.1 with free centres, widths, and relative heights (i.e. five free parameters for the two peaks) give a reasonably good fit $[P(\chi^2) = 20\%]$ with the parameters:

$$M_1 = 1.275\ (\pm\ 0.016)\ \text{GeV}, \quad \Gamma_1 = 0.020\ (\pm\ 0.010)\ \text{GeV};$$

$$M_2 = 1.318\ (\pm\ 0.016)\ \text{GeV}, \quad \Gamma_2 = 0.022\ (\pm\ 0.010)\ \text{GeV};$$

where the widths and heights of the two peaks come out equal within one standard deviation.

1.4.3 "Dipole"[6-8]. A good fit $P(\chi^2) = 70\%$ is obtained, using a simple two-parameter expression which contains a priori the apparent symmetry of the A_2 structure (equal widths and heights of the two peaks):

$$N(M) \sim \frac{\Gamma^2 (M - M_o)^2}{\left\{ (M - M_o)^2 + \frac{1}{4}\Gamma^2 \right\}^2} \qquad (1.5)$$

with

$$M_o = 1.296 \pm 0.016 \text{ GeV}$$

and

$$\Gamma = 0.030 \pm 0.003 \text{ GeV} .$$

This expression can be interpreted as a "dipole" in the $\rho\pi$ scattering amplitude. With this interpretation, the A_2 would obey a non-exponential decay law. Spin-parity analysis of the two A_2 peaks should give equal results in this case.

It has to be pointed out that two interfering Breit-Wigner curves -- a well-known phenomenon of interfering resonant states -- give as good a confidence level as the dipole, but more parameters are needed (5 and 2, respectively). It is interesting to note that the phase adjusts itself to 180°.

1.5 Evidence for structure in the R meson

After the report on the R(1675) boson[9] observed in the reaction $\pi^- + p \to p + R^-$ at the incident pion momentum of 6, 12, and 13 GeV/c, we have obtained a quantity of new data at 7, 11.5, and 12 GeV/c sufficient for the study of the mass distributions in histograms with bins of 10 MeV, instead of 40 MeV bins originally presented [4,10]. For this work we have used only the data obtained in the runs characterized by steady beam conditions, and the optimal mass-resolution in the region of 1700 MeV. The combined sample contains data from four runs:

i) a 12 GeV/c run, November 1965

ii) a 7 GeV/c run, December 1965

iii) a 12 GeV/c run, January 1966

iv) a 11.5 GeV/c run, autumn 1966.

Three narrow peaks with masses 1632 ± 15 MeV, 1700 ± 15 MeV, and 1748 ± 15 MeV are observed, referred to as R_1, R_2, and R_3. A fourth peak, referred to as R_4, is seen at a mass of 1830 ± 15 MeV in a way which is not statistically significant (Fig. 12).

To make sure that the peaks are not connected with the angular position of the spark chambers or counters, in autumn 1966 we set the proton telescope at 54° with respect to the beam, in comparison with 52° and 55° in the 7 and 12 GeV/c runs, respectively; a one-degree shift corresponds to a shift of about 25 MeV in mass.

The individual pieces of data are shown in Fig. 13. The appearance of the enhancements at the given masses, within ± 10 MeV, is evident. If the peak positions were not due to real resonances, for example if the mass values were connected with the value of p_1, then the shift from 12 to 11.5 GeV/c would cause all of them to shift about 50 MeV down.

1.5.1 Comparison with bubble chamber data. Owing to the similarity of our mass spectrum in the R region to that observed by Danysz et al.[11], it seems reasonable to discuss the G-parities of our peaks by comparing the two independent sets of data.

Danysz et al.[11] observed two peaks in the $\rho\pi\pi$ neutral system at masses 1717 ± 7 MeV and 1832 ± 6 MeV which could be the $R_2(1700)$ and the observed small enhancement we see around 1830 MeV. $R_1(1630)$ can be the small bump in the $\rho\pi\pi$ system which can also be seen in the data of Ref. 11. At the same mass there was a 2π peak observed by Crennell et al.[12] and Forino et al.[13].

The $R_3(1750)$ is not seen in the $\rho\pi\pi$ data. A reasonable explanation would be that R_3 has opposite G-parity to the R_1, R_2, and the 1830 peaks, i.e. that it is a G = -1 object corresponding to the broad 3π enhancement in this mass band observed by Armenise et al.[14].

1.5.2 Comparison with the quark L-excitation model[15]. It is interesting to note that on the basis of the L-excitation model of a charged quark-antiquark (or any fermion-antifermion) pair in a D-wave (L = 2, I = 1), one expects four states, three of them with G = +1, and a singlet with G = -1, since $G = (-1)^{L+S+I}$. The expected mass-square separation ΔM^2 which follows from the spin-orbit formula:

$$\Delta M^2 = \frac{1}{2} a^2 \left[J(J+1) - L(L+1) - S(S+1) \right] \qquad (1.6)$$

is given by:

$$\begin{array}{lcccc} 2S+1L_J & = & {}^3D_1 & {}^3D_2 & {}^1D_2 \quad {}^3D_3 \\ \Delta M^2 & = & -3 & -1 & 0 \quad +2 \ . \end{array} \tag{1.7}$$

Assuming the splitting is due purely to $\vec{L}\cdot\vec{S}$ coupling, let us suppose that we are dealing with four objects, whose quantum numbers and masses J^{PG}(mass) are: $1^{-+}(1630)$, $2^{-+}(1700)$, $2^{--}(1750)$, $3^{-+}(1820)$. Here, the relative mass-square separation is $(1.7 \pm 0.3) : 1 : (2.2 \pm 0.3)$, to be compared with $2 : 1 : 2$ expected from the above $L \cdot S$ mass splitting.

We assume that the separation between R_1 and R_3 corresponds to three units of $L \cdot S$ splitting. This gives the unit mass-square separation a^2 to be:

$$a^2 = \frac{1.748^2 - 1.630^2}{3} = 0.11 \text{ GeV}^2 \ . \tag{1.8}$$

Using $a^2 = 0.11$, we expect the masses of the other two members of the quadruplet: $M_{R_2}^2 = M_{R_1}^2 + 2a^2 = (1707)^2$, and similarly $M_{R_4}^2 = (1832)^2$, to be compared with the observed $M_{R_2} = 1700 \pm 15$ and $M_{R_4} = 1830 \pm 15$ MeV. Although in view of many mesonic states found, such coincidences are not improbable, and the agreement is suggestive (Fig. 14).

If we assume the linear rather than the mass-square dependence in Eq. (1.6) by replacing ΔM^2 with ΔM, the numerical agreement is not as good, but it is still not far outside the margin of error on the mass separation between each pair of peaks, which we take to be ±10 MeV. The linear unit separation becomes $a = 34$ MeV and the observed separation becomes $(1.5 \pm 0.2) : 1 : (1.7 \pm 0.2)$. We have taken the mass values of the R_1 and R_3 peaks as our standards, to obtain the unit separation, because they are the best defined ones and reproducible from run to run (see Fig. 13).

1.6 Discovery of three heavy bosons (mass > $2m_{\text{nucleon}}$)[16]

The mass spectrum of singly charged bosons of I = 1 or 2 has been investigated in the reaction

$$\pi^- + p \to p + X^-$$

in the mass region $1.2 < M_X < 2.45$ GeV with the missing-mass spectrometer at an incident π^- momentum of 12.00 ± 0.12 GeV/c, and in the momentum transfer region $0.22 < |t| < 0.43$ $(\text{GeV/c})^2$. A hydrogen threshold Čerenkov counter was inserted in the pion beam to separate the K^--induced events.

Three hitherto unreported heavy bosons have been observed in a mass region where bubble chamber results are inconclusive because of insufficient statistics. We shall refer to them as S, T, and U. Their masses M, physical widths Γ, and differential cross-section $d\sigma/dt$ are given below:

S: $M = 1929 \pm 14$ MeV $\qquad 0 \leq \Gamma \leq 35$ MeV

$\langle d\sigma/dt \rangle = 35 \pm 10$ microbarns at $0.22 < |\bar{t}| < 0.36$ $(\text{GeV/c})^2$.

Evidence for the S boson is presented in Fig. 15a, where the effect is observed with a statistical significance of 4.6 standard deviations.

T: $M = 2195 \pm 15$ MeV $\qquad 0 \leq \Gamma \leq 13$ MeV

$\langle d\sigma/dt \rangle = 19 \pm 10$ microbarns at $0.22 < |\bar{t}| < 0.36$ $(\text{GeV/c})^2$.

Evidence for the T boson is presented in Fig. 15b, where the effect is observed with a statistical significance of 5 standard deviations.

U: $M = 2382 \pm 24$ MeV $\qquad 0 \leq \Gamma \leq 30$ MeV

$\langle d\sigma/dt \rangle = 42 \pm 10$ microbarns at $0.28 < |\bar{t}| < 0.36$ $(\text{GeV/c})^2$.

Evidence for the U boson is presented in Fig. 16, where the effect is observed with a statistical significance of 6 standard deviations.

1.6.1 Statistical significance and upper limits to the physical widths. The statistical significance of S, T, and U peaks has been established by the following procedure:

i) First an attempt is made to fit the missing-mass distribution with a straight line which is a good approximation to the phase space in the mass band used in the analysis. In Figs. 15a, 15b, and 16, the straight-line hypothesis is rejected, with the confidence level $P(\chi^2) \lesssim 10^{-4}$.

ii) Removal of the points at the S, T, and U masses gives the straight-line fit with a confidence level $P(\chi^2) \geq 30\%$. This proves the existence of the peaks, with the statistical significance given above.

iii) The mass resolutions of the spectrometer in the S, T, and U regions obtained by a Monte Carlo calculation are: $\Gamma_{res} = 22 \pm 2$ MeV, 39 ± 2 MeV, and 62 ± 3 MeV. The observed peaks are fitted with a Gaussian of the width equal to our calculated resolution Γ_{res} plus a straight line. This gives a confidence level $P(\chi^2) \geq 30\%$ for all three peaks. From this we can conclude that their physical widths are compatible with zero.

iv) Instead of fitting the peaks with fixed values of Γ_{res}, we make the best fit with the experimental width Γ_{exp} as a parameter. Comparing Γ_{exp} and Γ_{res}, we derive the upper limits to the physical widths: $\Gamma_S \leq 35$, $\Gamma_T \leq 13$, and $\Gamma_U \leq 30$.

Fitting these peaks with a Breit-Wigner shape has no meaning because the physical widths are equal or smaller than our instrumental resolution. The different decay modes as indicated in the figures should not be taken too seriously since the errors on these quantities might be considerable.

1.6.2 Checks against systematic errors. Our belief that the peaks are not produced by systematic errors in our instrument comes from the fact that all three peaks are observed in three independent runs, made under different experimental conditions.

i) Run in May 1965: the spectrometer operated in the "tapered absorber mode": the proton telescope was centred at 52° to the beam direction.

ii) Run in November 1965: spectrometer operated in "flat absorber mode": at 55°. New sonic spark chambers were introduced.

iii) Run in January 1966: spectrometer operated in "flat absorber mode": at 52°. A new large proton range counter R_4 was introduced with different photomultiplier configuration.

An example of the cumulative nature of the evidence is given in Fig. 17 for the T boson.

Two important physical properties of the new resonances must be mentioned:

i) All three resonances have a narrow physical width Γ, the measured width being compatible with the experimental resolution Γ_{exp}. The interesting question arises, whether the narrow width is a common feature of heavy bosons.

ii) The mass of both the T meson and the U meson is larger than two nucleon masses. This means that a nucleon-antinucleon total cross-section experiment might see them. Indeed, Cool et al.[17] (BNL) see significant enhancements in $\bar{p}p$ and $\bar{p}d$ total cross-section in the momentum range 1.0 to 3.3 GeV/c at 2380 ± 10 MeV in the I = 0 state, and 2190 ± 5 MeV and 2345 ± 10 MeV in the I = 1 state.

But the difficulty when comparing their results with ours is in the appreciably larger width of their peaks (full width = 85 MeV and 140 MeV for the two I = 1 states, respectively). Goldhaber[18] suggests the existence of resonance clusters at the T and U mass, and that the MMS is specifically sensitive to one resonance out of each cluster, due to production mechanism.

* * *

2. DEVELOPMENT OF A NOVEL SYSTEM FOR ANALYSIS OF DECAY PROPERTIES OF HEAVY BOSONS

2.1 Limitations of the MMS

The instrument described in Section 1.2 allowed us to explore the boson mass spectrum, i.e. to measure central mass values M, widths Γ, and the shape of objects, differential cross-sections $d\sigma/dt$, and in a crude way the branching ratios for charged decay modes.

However, our scintillator matrix with its poor spatial resolution (element size about 10×10 cm^2) did not offer the possibility to get enough information about the decay products of X^-; it could not obtain good branching ratios and was completely unable to determine spin J and parity P of X^-.

2.2 Methods for J^P determination in $A_2^- \to \rho^0 \pi^-$

We give here a short description of the two most frequently used methods of determining the J^P of the meson, having in mind the reaction

$$A_2^- \to \rho^0 \pi^- \quad (2.1)$$
$$\hookrightarrow \pi^+ \pi^-$$

2.2.1 Analytic representation of the angular decay distribution of bosons. This is given by the solution of the eigenvalue equation of the differential spin operator, namely the spherical harmonics $Y_\ell^m(\vartheta,\varphi)$ where $\ell = 0, 1, 2 \ldots$ and $m = -\ell, -\ell + 1, \ldots, +\ell - 1, +\ell$.

For the $Y_\ell^m(\vartheta,\varphi)$ the well-known relation holds:

$$Y_\ell^m(\vartheta,\varphi) = \Theta_{\ell,m}(\vartheta) \cdot \Phi_m(\vartheta) \quad (2.2)$$

where

$$\Theta_{\ell,m}(\vartheta) = (-1)^m \sqrt{\frac{(2\ell+1)\,(\ell - |m|)!}{2(\ell + |m|)!}} \cdot P_\ell^m(\cos\vartheta)$$

and

$$\Phi_m(\varphi) = \frac{1}{\sqrt{2\pi}} \cdot e^{im\varphi} \quad .$$

Let us suppose that we produce an A_2 meson of spin 2, negative parity, and complete polarization along the z-axis, decaying into $\rho\pi$. Under these specific assumptions, the total spin-function of the A_2 can be written as:

$$\begin{aligned} \psi_2^2(A_2)^- = a \cdot Y_1^1 \psi_1^1(\rho) \\ + b[Y_3^1 \psi_1^1(\rho) \cdot \alpha_1 + Y_3^2 \psi_1^0(\rho) \cdot \alpha_2 \\ + Y_3^3 \psi_1^{-1}(\rho)] \, , \end{aligned} \tag{2.3}$$

where the first term describes the $\ell = 1$ state of the $\rho\pi$ system, the second one the $\ell = 3$ state, and the α_i are Clebsch-Gordan coefficients. Under the same assumptions but with the opposite intrinsic parity, the total wave function of the A_2 has the form

$$\psi_2^2(A_2)^+ = \alpha_1' \cdot Y_2^2 \psi_1^0(\rho) + \alpha_2' \cdot Y_2^1 \psi_1^1(\rho) \tag{2.4}$$

corresponding to an $\ell = 2$ state.

From this we find the expression for the angular distribution of the decay:

$$\begin{aligned} N^-(\Theta) = \psi_2^2(A_2)^{-*} \psi_2^2(A_2)^- = |a|^2 \cdot Y_1^{1*} Y_1^1 \\ + |b|^2 \cdot (Y_3^{1*} Y_3^1 \cdot \alpha_1^2 + Y_3^{2*} Y_3^2 \cdot \alpha_2^2 + Y_3^{3*} Y_3^3 \cdot \alpha_3^2) \\ + a^* \cdot b \cdot Y_1^{1*} Y_3^1 \cdot \alpha_1 + a \cdot b^* \cdot Y_1^1 Y_3^{1*} \cdot \alpha_1 \end{aligned} \tag{2.5}$$

for the negative parity case, and

$$N^+(\Theta) = \alpha_1'^2 Y_2^{2*} Y_2^2 + \alpha_2'^2 Y_2^{1*} Y_2^1 \tag{2.6}$$

for the positive one.

In general, the contributions from high ℓ-terms are small because of the centrifugal barrier and can be neglected. If one does not assume that the A_2 meson is fully polarized, analogous terms for the other polarization states show up. The total wave function is then a superposition of all possible terms with unknown weights. For unknown spin, polarization, and parity, the situation becomes rather complicated, and extremely good statistics are needed to fit all free parameters.

2.2.2 Dalitz plot. In order to deduce the method and idea of the Dalitz plot, some considerations on the matrix element and on phase-space have to be given.

Let us consider the multipion production reaction for developing expressions for the matrix element and phase space:

$$\pi + p \rightarrow p + n\pi \,. \tag{2.7}$$

(The $n\pi$ system can be resonant or not.) The connection between initial state ψ_i and final state ψ_f of this reaction is given by Fermi's Golden Rule:

$$W = \frac{2\pi}{h} |\langle\psi_f| H |\psi_i\rangle|^2 \cdot R_n(E) \,, \tag{2.8}$$

where W is the transition probability from ψ_i to ψ_f, caused by a perturbation H of the Hamiltonian. $R_n(E)$ is the phase space, a function of the total energy E, and the number n of pions in the final state, while

$$\langle\psi_f| H |\psi_i\rangle$$

is the matrix element M. Equation (2.8) can be written in such a way that $|M|^2$ and $R_n(E)$ are Lorentz invariant. In strong interactions, $|M|^2$ is generally completely unknown.

The explicit form of $R_n(E)$ is given by

$$R_n(E) = \int \prod_{i=1}^{n} [d^4 q_i \, \delta(q_i^2 - m_i^2)] \cdot \delta^4 \sum_{i=1}^{n} (q_i - Q) \; ; \qquad (2.9)$$

$\underline{q_i}$ is the four-vector of the i^{th} pion:

$$q_i = (\vec{p_i}, E_i) \; ; \quad \text{length: } q_i^2 = E_i^2 - p_i^2$$

$\underline{Q}$ is the four-vector of the initial state:

$$Q = (\vec{P}, E)$$

$$\vec{p} = \sum_{i=1}^{n} \vec{p_i} \; ; \qquad E = \sum_{i=1}^{n} E_i \; .$$

$R_n(E)$ gives the total volume in momentum space available for n pions of total energy E. The term $\delta(q_i^2 - m^2)$ requires that all i particles be on the mass shell (by convention we have limited E_i to positive values).

We will now discuss in more detail the three-pion final states. In order to make possible the following analysis, the three-pion effective mass has to lie in a narrow mass interval (in our case this interval will be the mass region of the A_2 meson from 1.26 GeV to 1.36 GeV). The kinetic energies of the three pions in the c.m. system are T_1, T_2, and T_3, respectively. The Dalitz plot representation is a scatter plot of the kinetic energies of any two out of the three particles in a Cartesian coordinate system. Momentum and energy conservation confine the points to an area within a closed curve touching the two axes. From energy-momentum conservation one sees that, given the kinetic energies of two pions, the situation is uniquely specified. Such a distribution is called a Dalitz plot.

One advantage of this representation is the following: equal areas on the Dalitz plot correspond to equal probabilities in the Lorentz phase space. This means that phase space predicts a uniform distribution of points on a Dalitz plot. Apart from the experimental biases and statistical fluctuations, a non-uniform distribution gives some information regarding spin, isospin, parity, and form factors. In other words, the point density is proportional to $|M|^2$, where the square of the matrix element contains all the physical information.

In many cases, it is useful to introduce a slightly different form of the Dalitz plot, namely one where the effective mass squared of any two pions from three-body final states is plotted along the x and y areas of a Cartesian coordinate system. The effective mass of n particles is defined by

$$M^2_{eff} = \left(\sum_{i=1}^{n} E_i \right)^2 - \left(\sum_{i=1}^{n} \vec{p}_i \right)^2 . \qquad (2.10)$$

This is called an effective mass plot and will be used in the analysis of our data. Phase space alone predicts a uniform population on this plot as well as on the original Dalitz plot.

Let us now discuss the effective mass plot in a mass interval where a resonance is sitting on top of some background (having already the A_2 region in mind). The background can be a free three-pion one corresponding to a uniform point distribution, or it can be resonant within two pions corresponding to a non-uniform background of the Dalitz plot. The resonance itself will never produce a uniform distribution. The general amplitude M is limited by the specification of the isospin, spin, and parity of the 3π final state, eventual intermediate decay state, and by Bose statistics. The amplitude M may be thought of as the sum of products of the form

$$M = M_I \cdot M_F \cdot M_{JP} . \qquad (2.11)$$

M_I carries the isotopic spin dependence, the energy-momentum dependence is in the "form-factor" M_F, and M_{JP} carries the spin J and the parity P. If

M_I and M_F can be evaluated, the density distribution of the effective mass plot is directly linked to the spin and parity of the resonance.

2.3 Novelties in our approach to the determination of J^P of the A_2

From the last paragraph, it is seen that a Dalitz plot is much more convenient and promising when determining J^P of the A_2 than the analysis of the angular distributions, but one needs the momenta of the decay particles. These are usually measured by magnetic analysis. The difficulty in our case was that no automatic track-measuring instrument operating in a strong magnetic field was available or easy to invent. But we found another possibility of determining the momenta of the decay particles, which is described below.

If one selects events where the A_2^- is decaying into $\pi^+\pi^-\pi^-$, and if one finds possibilities of measuring precisely the laboratory angles of the three charged decay pions, one can calculate their momenta by applying four-momentum conservation to the whole reaction, including the recoil proton (1C fit).

These considerations led us to an instrument having the following suitable specifications:

- good reconstruction precision to achieve a good mass resolution
- high multiparticle efficiency
- digitized read-out system -- for on-line operation
- good spatial resolution -- to resolve close particle trajectories
- large solid-angle acceptance
- fairly good time resolution -- to avoid beam particles
- low dead-time -- to obtain high statistics
- simplicity.

To fulfil the above conditions, one can think of a scintillator matrix with small elements. Down to "spaghetti-counters" of $3 \times 3 \times 700$ mm^3, technical problems have been solved, for instance by Lindenbaum et al.[19] at BNL. In our case, the number of elements necessary to cover a large area such as 150×150 cm^2 would have been prohibitive. A matrix of Geiger counters does not have a good enough multispark efficiency, since spurious tracks and breakdowns are difficult to avoid. A small-gap chamber of large area cannot be operated in the track-following mode: breakdown will occur

perpendicular to the electrodes since the capacity of the chamber is so high that the HV pulse does not have a rise-time short enough to work in the track-following mode. Furthermore, its multiparticle efficiency is low, since the chamber is shunted by one track which is perpendicular to the electrodes so that inclined tracks can no longer be seen.

Wide-gap chambers, either in the track-following or in the streamer mode, had not yet been digitized.

We decided to digitize a wide-gap chamber[20-35] operating in the track-following mode. The choice of wide gaps was dictated by the following reasons:

- The efficiency of a wide-gap chamber against spurious sparks, e.g. those produced by δ rays, is high, since the probability of the occurrence of a 10 cm long string of ionized atoms not caused by the passage of a charged particle is extremely small. A string of ions with about one electron per cm is necessary for building up the spark channel.
- It has a high multispark efficiency, since the statistical fluctuation of the number of charges along a long trajectory is less than along a short one.
- It reduces considerably the number of read-out devices if one compares it with a system of narrow-gap chambers asking for the same over-all multispark efficiency and safety against spurious tracks.
- The spark follows the trajectory from electrode to electrode, also for inclined tracks up to 45°, and is not perpendicular to the electrodes as in the case of small-gap chambers. This gives the precision improvements.

Automatic read-out systems[36-57] had been developed and were already in use with ordinary narrow-gap chambers. Three useful types of automatic read-out systems for wide-gap chambers existed:

- image digitizing (Vidicon, Superorthicon system)
- the ferrite core system
- magnetostrictive read-out system.

The first possibility has the advantage that it can give full information along the whole track, which is especially valuable in a magnetic field, but a lot of development work is still necessary. The ferrite core system

has the advantage of great flexibility for multispark events, and also the advantage of small spark currents (~ mA), but each wire has to be connected to the computer by a cable, e.g. a four-plane chamber of 1.5 × 1.5 m^2 sensitive surface and a wire spacing of 1 mm would need 6000 cables. Furthermore, a uniform flipping threshold is difficult to achieve for a large core assembly. Therefore we have chosen the magnetostrictive read-out system.

2.4 Theory of spark mechanism

In order to have a better understanding of our instrument, we shall discuss the theory of gas breakdown in some detail[57].

At the beginning of this century, Townsend[59,60] studied the variation of current between parallel plane electrodes in a gas as a function of an applied electric field. He observed that with increasing voltage the current first increases until it reaches a plateau corresponding to the photo-current produced at the cathode, for example by external UV illumination. As the field is further increased, a rapid rise of current is observed (Fig. 18). Townsend explained this fact as gas ionization due to electron collision. Photoelectrons leaving the cathode give a sufficient amount of energy to ionize the gas atoms of molecules; the released electrons then continue the ionization process: an avalanche is formed. A coefficient α can be introduced to define the number of secondary electrons produced in the path of a single electron travelling a distance of 1 cm (α = Townsend's first ionization coefficient). The current i flowing in the gap is then given by

$$i = i_o \cdot e^{\alpha d} \qquad (2.12)$$

where d(cm) is the gap length.

Numerous measurements of α in various gases (such as helium, neon, argon, nitrogen) have been carried out by Townsend and his colleagues from 1900 onwards. A full discussion of the results and the various effects observed in different gases has been given by Loeb[61].

Figure 19 shows some curves obtained by Kruithof and Penning[62] for neon and neon-argon mixtures.

It is of interest to note that the α-values for pure helium or argon are smaller than for a helium gas with small argon mixtures. This effect may be explained by ionization of argon atoms (ionization potential 15.8 V) by metastable neon atoms (excitation potential 16.53 V) (Penning effect).

Over a certain voltage range, formula (2.1) coincided well with measurements. But for a rather high voltage, the current increases more rapidly than given by equation (2.1), and therefore secondary mechanism must set in, e.g. collisions between positive ions and molecules or positive ion bombardment of the cathode.

A coefficient γ can be introduced denoting the number of secondary electrons per positive ion without referring to a specific production process (γ = Townsend's second ionization coefficient). The current can then be written:

$$i = i_0 \frac{e^{\alpha d}}{1 - \gamma(e^{\alpha d} - 1)} \quad . \tag{2.13}$$

On a basis of spark mechanism depending on positive ion bombardments of the cathode, a formation time is to be expected in accordance with the time of positive ion movement across the gap. Furthermore, the cathode material should influence the current behaviour. In oscilloscope studies of the spark development in time, much shorter formation times than expected were recorded and no dependence from the cathode material was found. Similarly, a cathode effect can hardly be involved in the growth of lightning from a cloud during a thunderstorm.

Stimulated by these disagreements, a new theory of spark formation was proposed in 1940 by Meek[63], and independently by Raether[64]. It is now generally referred to as the streamer theory, and explains the breakdown by Townsend α-mechanism, photo-ionization, and space-charge field effects caused by avalanches and streamers. It is worth while to look into this process in detail.

An ionizing particle traverses a gap between two plane electrodes, and produces in neon at ~ 1 atm about 30 free electrons per cm. A HV pulse is applied to the gap, creating an electric field $\vec{E}_0$ at t = 0. If the electric field is strong enough, the electrons produced by the ionizing particle

gain sufficient energy to ionize the gas and produce an avalanche (Figs. 20a, b, c). The positive ions move slowly towards the cathode and can be considered stationary. The head of the avalanche is moving with a speed of $\sim 10^7$ cm/sec towards the anode. Inside the avalanche, a field $\vec{E}_a$ opposite to $\vec{E}_o$ is produced. The net field inside the avalanche is smaller than $\vec{E}_o$ and decreases as the avalanche grows. The field outside the head and tail of the avalanche is larger than the applied field and increases as the avalanche grows. It is obvious that the growth of the avalanche will stop when $\vec{E}_o = -\vec{E}_a$ since there is no net field left inside the avalanche.

This is the moment $t = t_{cr}$, when a new mechanism enters the game. Inside the avalanche the ionization density is so high that a non-negligible photon flux is emitted isotropically. The photons create secondary electrons, but only those that are in a high field region (head and tail of avalanche) gain sufficient energy. There, α is large, and in a short time a lot of secondaries are produced forming a new avalanche. This process is called a streamer (Kanalaufbau) (Fig. 20d). A plasma channel along the different streamers is built up between the two electrodes through which breakdown will take place (Fig. 20e). This is called the track-following mode of operation.

Within some limits, the situation can be described by the formula[65]:

$$\vec{E}_a = \frac{4}{3} \epsilon \alpha \rho \; e^{\alpha\delta/X^2} \tag{2.14}$$

where

$\vec{E}_a$ = the electric field caused by the cascade at a distance X from the centre of the head of the cascade.
ϵ = electron charge
α = first Townsend coefficient
ρ = radius of avalanche head
δ = path covered by the avalanche.

If it is assumed that the cascade is developed along the initial trajectory, the field $\vec{E}_a$ must be at least equal to the external field $\vec{E}_o$:

$$\vec{E}_a = \frac{4}{3} \epsilon \alpha \rho \; e^{\alpha\delta/X^2} = \vec{E}_o \; e^{-t \cdot 10^7} \tag{2.15}$$

where t is the action time of the external field. For $t = 5 \times 10^{-8}$ sec, the space-charge field is about equal to the external field. Then $\rho = 0.007$ cm.

If we denote by ℓ the average distance between primary electrons (in Ne $\sim$ 0.03 cm), then if $2\rho > \ell \sin\theta$ the neighbouring clouds will overlap. This gives the order of magnitude of the critical angle θ, up to which the spark will follow the track:

$$\sin\theta < 0.007/0.03 \rightarrow \theta < 30^{\circ} \ .$$

The effective maximum angle is influenced by many other parameters. On a more empirical basis, the Meek-Raether condition indicates when the avalanche is turning into a streamer:

$$\alpha_{eff} \cdot v \cdot t_{cr} \sim 20 \qquad (2.16)$$

where α_{eff} is the local Townsend coefficient, v the avalanche velocity, and t_{cr} the critical time.

Two different operation modes of a wide-gap spark chamber must be distinguished:

i) The streamer formation is stopped when the two electrodes are connected electrically via a plasma channel through which breakdown occurs. This is only useful if the plasma channel follows the trajectory of the initial ionizing particle, e.g. in cases when the trajectory is parallel to the electric field ±45°. This is called: "track-following mode".

ii) The streamer formation is stopped (by a short enough high-voltage pulse) when it has reached a length giving light enough to be photographed. The trajectory is then seen as a series of small luminous dots (1-2 mm) or lines (3-5 mm) depending on the direction from which one views it (Fig. 21). One sees that this is a completely isotropic instrument showing even those particle trajectories which start inside the sensitive volume of the chamber (Fig. 22). A chamber of this type was constructed and operated for the first time by G.E. Chikovani and collaborators. It is called a streamer chamber.

2.5 Principles of operation of a wide-gap wire chamber

Suppose a chamber is operated in the track-following mode and consists of four wire planes: X_1, Y_1, X_2, Y_2. X_1 is rectangular to Y_1, X_2 to Y_2, and the distance X_1Y_1 equals X_2Y_2 equals d ($d \geq 5$ cm, i.e. wide gap). The planes X_1 and Y_2 are outside electrodes on ground potential. When an ionizing particle has traversed such a chamber, the HV pulse is applied to the central electrodes. Breakdown occurs along the particle trajectory in the gap X_1Y_1 and X_2Y_2 (Fig. 23). A current passes through those wires that are touched. On top of plane X_1Y_1 and X_2Y_2, outside the fiducial volume of the chamber, a magnetostrictive signal (a combination of a travelling change of magnetic field and a shock wave) is induced in the magnetostrictive wire at the place where the current-leading wire crosses it. A measurement of the time delay of this signal at the end of the magnetostrictive wire identifies the wires which lead the current. This means that the particle trajectory can be completely reconstructed. For more than one particle, an ambiguity appears: in the case of two particles for instance, two X_1 and two Y_1 wires are hit. This gives four possible points but there are only two particles. In the case of three particles, there are nine possible points per gap, but only three are belonging to true particle trajectories. The ambiguities can be resolved by forming pairs of wire planes of angles $\neq 90°$ with respect to each other.

2.6 Construction and operation of a prototype chamber

A prototype chamber has been built. It is a four-electrode system with HV on the two central electrodes and ground connection at the outside planes. All four electrodes are wire planes (phosphor-bronze wire of 0.1 mm diameter) with a wire spacing of 1 mm. Between ground and high-voltage electrodes there is a distance of 10 cm, between the two HV electrodes there is 1 cm spacing. The frames are made of araldite; plexiglas pieces give the spacing between ground and HV planes, and mylar windows close the system. The chamber is held together by plexiglas screws in each corner (perpendicular to the wire planes). The sensitive volume of one gap is $40 \times 40 \times 10$ cm^3 (Fig. 24).

The chamber is triggered on cosmic rays by three scintillator counters. A HV pulse of 100-150 kV with a rise-time of about 25 nsec (for the system chamber + generator together) is created by means of an ordinary Marx generator with an equivalent capacity of 860 pF (Figs. 25, 26). To decrease the charging time, the capacitors are charged independently; this gives a repetition rate of 200 firings per second. The HV pulse length can be regulated by a spark gap of adjustable distance connected in parallel to the chamber (shunting gap), or with resistors parallel to the chamber. The memory-time (maximum time between ionizing particle passage and trigger still giving a breakdown at the place of the trajectory) is measured by delaying the trigger pulse until visual tracks vanish. With pure henogal (70% Ne, 30% He), the memory-time is found to be about 15 μsec, which is much too long for most applications of wide-gap chambers. A clearing field does not work effectively in a wide-gap chamber due to the big collection time. The only possibility of reducing the memory-time is to add quenching gas admixtures[45,46] (electronegative gas which eats up electrons within a very short time). In order to have a high number of primary electrons and a very steep decrease in time, we add ~ 5% argon and 2×10^{-3}% of freon-12, which reduces the memory-time to ~ 2 μsec. Figure 27 shows the efficiency of the chamber versus time delay for different quencher admixtures. This memory-time is sufficiently short for a PS beam with 7×10^4 pions per burst and a spill of 250 msec.

Another important quantity is the recovery-time (minimum time between two breakdowns, without a spark at the second breakdown in the plasma channel built up by the first breakdown; lifetime of a plasma channel). It is measured by triggering the chamber with a double HV pulse. The second trigger is applied with a changeable delay. The magnetostrictive signal from the chamber is analysed with a double-beam scope. The delay is made very long (~ 20 msec) and then shortened; the recovery-time is reached since the repetition rate of the Marx generator is too low. From this we conclude that the recovery-time of the chamber is smaller than 5 msec. This is sufficient for our problems, since the dead-time of the MMS is 10 msec.

Working with this prototype chamber, the following disadvantages appeared:

- spurious breakdowns along the plexiglas screws in the corners;
- the fact that the chamber could not be opened.

2.7 Construction and tests of large-area chambers[66]

Three chambers with outer dimensions of 162 x 162 x 33 cm^3 were constructed at the Physics Department of Bern University (Fig. 28). The sensitive volume per gap is 146 x 146 x 10 cm^3. In order to reduce the forces acting on the frames, the wires were wiggled, a method invented and applied for the first time by F. Krienen, CERN. For such large frames the question of rigidity became important. The frames of the two ground electrodes were stiffened by steel profiles glued on top. The central electrode was made out of two fibreglass frames with a steel profile in between. Each wire plane was perpendicular to the neighbouring planes. In order to have chambers that can be opened, the plexiglas was cut into two pieces in each gap; one piece was glued to the HV side, the other one to the ground side. Gas leaks are prevented by rubber gaskets between the plexiglas pieces. The chambers are held together by solid clamps which are also used to keep the system in place during the experiment. The wire ends are free on one side and soldered to a copper bar on the other, so as to make HV and earth connections (Fig. 29). The same tests made previously with the prototype chamber were repeated with the large ones and all results were confirmed. As a next step, the chambers were taken to the CERN Synchro-cyclotron. A beam of $\sim 2 \times 10^5$ protons per second, but distributed over an area of ~ 500 cm^2, was available to us.

A first problem was to get rid of the high electromagnetic noise coming from the chambers, which fired scalers and pattern units within 30 m. The chambers were put into double-wall Faraday cages (wall thickness = 0.1 mm, spacing between the two walls = 1 cm). When the two walls are connected in one point and all mass cable loops are avoided, the noise can be reduced to a tolerable level.

With incident hodoscopes (small scintillator counters) a particle trajectory was defined.

With one chamber, an x- and a y-coordinate were measured. From this, a first idea about the measuring precision of the chamber was obtained: ± 1 mm. By changing the angle of the chamber with respect to the beam, the maximum angle of "trajectory following breakdown" was found to be $\sim 45°$.

A further test of the chambers was made in a 2 GeV/c, PS electron test-beam of extremely low intensity (~ 30 electrons per burst). Lead pieces of different thickness (0.5, 1, 2, 3, ... radiation lengths) were put into the beam in order to create secondaries. Two chambers were used, and the number of tracks in all four gaps was found to be equal in most cases. Furthermore, multiparticle efficiency was studied visually and judged to be good.

2.8 The read-out[66]

During all these tests and the test-run to follow, only ground electrodes were read for reasons of simplicity. Among the many possibilities for magnetostrictive read-out, the simplest one has shown best results: a hard 50/50 Co/Fe Vacoflux strip held by an aluminium support (Fig. 30). The position of the strip with respect to the support is adjustable. Signals at the end of the strip are damped by 10 cm long polyethylene tubes filled with silastic (ratio of reflection to signal = ~ 1 : 20). The signal attenuation in the wire has been found to be a factor of two per two metres. The support of the wire is fixed on the ground electrodes with plexiglas clamps, insulated by a 0.2 mm mylar sheet. Twenty turns of 0.06 mm copper wire, put directly on the strip, are used as magnetostrictive pick-up coils. This kind of coil has two important advantages:

i) since the weight of the coil is negligible, the magnetostrictive waves are not deformed and therefore the signal is very clean;

ii) the coil has a very low impedance, therefore the pulse can be amplified in a transformer at the end. The signal behind the transformer is about 2 mV high and 500 nsec wide at the base. The resolution (minimum distance of two signals still recognized as two) is 3 mm.

To read the magnetostrictive wire at both ends has the advantage of getting fully redundant information about spark location. This is very useful in multispark events.

2.9 Read-out electronics[66]

The block scheme of the electronics behind the coil is shown in Fig. 31. A master signal coming from the fast electronics of the MMS triggers a Commander (Fig. 32) which triggers the chambers and, by means of a "start"

pulse, opens the gates of the scalers which then start counting with 20 MHz. The start pulse is delayed by $\Delta T = 20$ μsec to avoid pick-up in the scalers. This time delay is measured in an additional scaler ("ΔT scaler").

As mentioned above, the magnetostriction signals from the coil are fed into a special transformer (Fig. 33). The positive output signals are transmitted to a three-stage linear amplifier (Fig. 34) with a gain of 450. The position of the maximum of these output signals (~ 2 V) is determined in a zero-crosser[5] (Fig. 35). The output signals from the zero-crosser (+8 V) are transmitted to the selector (Fig. 36). The incoming signals are distributed on several outputs (max 4) which close the gates of the corresponding scalers. After a certain time (300 μsec), all scaler gates which are still open are closed by a "stop" pulse coming from the Commander. After each "stop" pulse, information from all 41 scalers is transferred to an SDS 920. There, the information is handled in the same way as all the rest of the information from the MMS (writing on tape, sending via data-link to CDC 6600, etc.).

The time schedule for the whole system is shown in Fig. 37.

2.10 Multispark events

Each coil has four associated scalers, so four signals per coil and trigger can be stored. Since each plane has two reading coils, a maximum of eight signals per trigger and plane can be stored. With four or less signals per plane, the whole information is redundant because each spark signal is read from both sides. With more than four signals, redundancy is partially (5-7 signals) or completely lost (8 signals).

Let us discuss the case of the three sparks in one plane. The first signal in the left-hand coil corresponds to the third signal in the right-hand coil, the second to the second, and the third to the first. The sum of clock-pulses in corresponding scalers must be constant. Similar relations exist with one, two, and four sparks.

Now suppose we have five sparks per plane. The first signal in the left-hand coil has no stored corresponding signal from the right-hand coil; the same is true for the first signal in the right-hand coil. Signal number "two, left" corresponds to signal number "four, right"; signal number "three, left" to signal number "three, right"; and signal number "four, left" to signal number "two, right". Similar rules can be found with six or seven

sparks. With eight sparks, there is no redundancy at all. As a further check, the total number of sparks per coil was counted in additional scalers ("multiplicity scalers"), and this information is compared with the content of the coordinate scalers[31]. The signals for these multiplicity scalers are taken from the zero-crossers.

2.11 Definitions and track reconstruction

Suppose we have two coils separated by a distance L; v is the magnetostrictive signal velocity, and the spark distance from left-hand coil is x:

$$t_\ell + \Delta T = \frac{x}{v} \tag{2.17}$$

$$t_r + \Delta T = \frac{L-x}{v} \tag{2.18}$$

where t_ℓ and t_r are time intervals measured by the left- and right-hand scalers, respectively, and ΔT is the time interval going to the scalers. Since the trigger has a jitter, we compute the spark coordinate in a way which is independent of ΔT, whenever signals are read from both sides simultaneously. From Eqs. (1) and (2):

$$x = \frac{L - v\,(t_\ell - t_r)}{2} \,. \tag{2.19}$$

For a precise measurement of v, two artificial sparks per plane with known positions with respect to the coils are used. The velocity v was determined at the beginning and at the end of each run using the test sparks, and was found to be constant.

From Eqs. (1) and (2):

$$t_\ell + t_r = \frac{L}{v} - 2\Delta T \approx \text{const} \,, \tag{2.20}$$

which gives the possibility of finding and checking corresponding signals.

As soon as the coordinates of a track coming from the target are known in all four planes, spatial reconstruction of the track is possible, using chamber-and proton-line information. Of course, reconstruction can be done

with the chambers only, but a more precise reconstruction is obtained by using also the vertex coordinates. The frame of reference which defines the coordinates is illustrated in Fig. 38. The first plane of the first chamber at the distance y_1 from the target centre gives an x_1 coordinate, the second plane of the first chamber at a distance y_2 gives a z_2 coordinate. In the second chamber, x_3' and z_4' are measured at a distance y_3 and y_4 with respect to the target centre (the coordinate system x_3' z_4' is rotated by an angle of 15° with respect to the main coordinate system x_1, z_2 as defined by chamber 1). The vertex of the reaction has coordinates x_0, y_0, z_0.

The information can be treated as three points in space. For a straight line, given by the expression:

$$\begin{aligned} x &= a_x y + b_x \\ z &= a_z y + b_z \end{aligned} \qquad (2.21)$$

χ^2 is given by

$$\chi^2 = (x_1 - a_x y_1 - b_x)^2 + \left(\frac{x_3'}{\cos\alpha} + (a_z y_3 + b_z)\,\mathrm{tg}\,\alpha - a_x y_3 - b_x\right)^2$$

$$+ (z_2 - a_z y_2 - b_z)^2 + \left(\frac{z_4'}{\cos\alpha} - (a_x y_4 + b_x)\,\mathrm{tg}\,\alpha - a_z y_4 - b_z\right)^4$$

$$+ (x_0 - a_x y_0 - b_x)^2 + (z_0 - a_z y_0 - b_z)^2 \quad .$$

Minimizing this quadratic form with parameters a_x, b_x, a_z, b_z leads to four linear expressions:

$$\begin{aligned} a_x \cdot a_{11} + b_x \cdot a_{12} + a_z \cdot a_{13} + b_z \cdot a_{14} &= k_1 \\ a_x \cdot a_{21} + b_x \cdot a_{22} + a_z \cdot a_{23} &= k_2 \\ a_x \cdot a_{31} + b_x \cdot a_{32} + a_z \cdot a_{33} + b_z \cdot a_{34} &= k_3 \\ a_x \cdot a_{41} + a_z \cdot a_{43} + b_z \cdot a_{44} &= k_4 \end{aligned} \qquad (2.22)$$

with coefficients

$$a_{11} = y_0^2 + y_1^2 + y_3^2 + y_4^2 \, tg^2 \, \alpha$$

$$a_{12} = y_0 + y_1 + y_3 + y_4 \, tg^2 \, \alpha$$

$$a_{13} = -(y_3^2 - y_4^2) \, tg \, \alpha$$

$$a_{14} = -(y_3 - y_4) \, tg \, \alpha$$

$$a_{21} = y_0 + y_3 + y_4 \cdot tg^2 \, \alpha$$

$$a_{22} = 3 + tg^2 \, \alpha$$

$$a_{23} = -(y_3 - y_4) \, tg \, \alpha$$

$$a_{31} = -(y_3^2 - y_4^2) \, tg \, \alpha$$

$$a_{32} = +(y_3 - y_4) \, tg \, \alpha$$

$$a_{33} = -(y_0^2 + y_2^2 + y_4^2 + y_3^2 \cdot tg^2 \, \alpha)$$

$$a_{34} = -(y_0 + y_2 + y_4 + y_3 \cdot tg^2 \, \alpha)$$

$$a_{41} = -(y_3 - y_4) \, tg \, \alpha$$

$$a_{43} = y_0 + y_2 + y_4 + y_3 \cdot tg^2 \, \alpha$$

$$a_{44} = 3 + tg^2 \, \alpha$$

$$k_1 = x_0 y_0 + x_1 y_1 + \frac{x_3' y_3}{\cos \alpha} + \frac{z_4' y_4}{\cos \alpha} \cdot tg \, \alpha$$

$$k_2 = x_0 + x_1 + \frac{x_3'}{\cos \alpha} + \frac{x_4'}{\cos \alpha} \cdot tg \, \alpha$$

$$k_3 = y_0 z_0 - y_2 z_2 - \frac{z_4' \cdot y_4}{\cos \alpha} + \frac{x_3' \cdot y_3}{\cos \alpha} \cdot tg \, \alpha$$

$$k_4 = z_0 + z_2 + \frac{z_4'}{\cos \alpha} - \frac{x_3' \cdot tg \, \alpha}{\cos \alpha}$$

2.12 Technical results from a test-run of the boson spectrometer

As a next step, two wide-gap wire chambers were adapted to the "old" MMS. The combination of the old MMS and the vertex chambers is called the boson spectrometer (BS), and the set-up is shown in Fig. 39. Because of geometrical restrictions, the first chamber had to be shifted in such a way that the chamber centre and the beam no longer coincided.

2.12.1 Our on-line computer SDS 920 enabled us to print out the content of all scalers for each event (Fig. 40). For each read-out wire, the constancy of the sum "left-hand coil plus right-hand coil" could be checked. Furthermore, it was possible to maximize the efficiency of each gap by changing the shunting resistor value, and to detect faults in either one of the read-out coils.

2.12.2 In order to estimate again the precision of the chambers, a so-called "0-degree test" was made. A particle trajectory was defined by two widely spaced hodoscopes H1 and H2 (compare Fig. 39), the dimensions of which were $5 \times 5 \times 1$ mm^3. The precision of particle localization has been computed from coordinate differences in the corresponding planes.

The difference between the two x-planes is shown in Fig. 41, that of the z-planes in Fig. 42. The width of the distribution at half-height is ±1.2 mm. This measurement is also used for the geometrical calibration of the wire chamber position preceding a production run.

2.12.3 The elastic reaction

$$\underset{(1)}{\pi^-} + \underset{(2)}{p} \rightarrow \underset{(3)}{p} + \underset{(4)}{\pi^-} \qquad (2.23)$$

was used for checking the system under real conditions in order to ascertain its reconstruction precision. By measuring the angles Θ_4 and the momentum p_3 of the recoil proton, elastic events can be selected and the trajectory of the scattered pion can be computed. The distribution of elastic pions in wire chamber 1 is shown in Fig. 43. Since the associated protons are coming from all five momentum intervals, the proton angles are measured with some errors, and the momentum of the incident pion is known only within 1%, the distribution cannot be expected to be "point-like".

The elastic events are fitted with the procedure described above. The distribution of differences between fits and measured coordinates in different planes are shown in Figs. 44, 45, 46, and 47. In Fig. 48, the difference between computed and fitted angle of the scattered pion with respect to the incident beam direction is shown. The uncertainty in the angle due to errors from beam and proton side measurements is ±2.3 mrad, the measured value is ±2.0 mrad, i.e. the errors from the vertex chambers are small compared to the proton side and beam errors.

2.12.4 The memory-time of the chamber could not be shortened enough to avoid beam tracks since the trigger coming from the proton side had a delay of ~ 500 nsec. Therefore the beam region inside the chambers was made dead by a "beam killer": a styrofoam disc of 3 cm thickness and 6 cm diameter, covered by mylar and held in position by four nylon strings (the beam diameter at the chambers was about 4 cm). The efficiency of the beam killer is seen in Fig. 49.

2.13 Solutions to some technical difficulties in the development

In the January 1967 run, the following major shortcomings and faults in the wide-gap wire chambers appeared:

i) Behind each magnetostrictive signal, an oscillation was seen during about 2 μsec with one, two, or three maxima, simulating tracks. Since at that time the effect was not understood and could not be avoided, after each signal an electronic dead-time of 2 μsec was introduced. This enlarged our resolution to ~ 1 cm (the precision of ±1.25 mm is unaffected).

ii) The high-voltage pulse of 100 kV gave an extremely high radiation which was difficult to shield.

iii) The HV planes were not read, because difficulties arise if one tries to keep the HV pulse out of the electronics.

After the run we found that a chamber with a gap of 5 cm works well. This had the advantage that only 50 kV are necessary and electromagnetic radiation is therefore reduced. The oscillation behind the magnetostrictive signals can be avoided by proper damping, which improves the resolution to 3 mm. Finally, we succeeded in reading the signals from the HV planes of the 5 cm chamber through an Eddy-current transformer of the type described above but with the primary coil cast in araldite.

* * *

3. DALITZ PLOT OF THE A_2 MESON REGION OBTAINED WITH THE NEW SYSTEM

3.1 Method

Under the hypothesis that in the reaction

$$\pi^- + p \rightarrow p + X^- \tag{3.1}$$

only the decay

$$X^- \rightarrow \pi^+ \pi^- \pi^- \tag{3.2}$$

is present, the momenta $\vec{P}_i$ of the three decay pions can be computed from their angles and momentum conservation in reaction (3.1):

$$\sum_1^3 \vec{P}_i = \vec{p}_1 - \vec{p}_3 \,. \tag{3.3}$$

This method fails for coplanar pions, since in this case the three momenta are no longer linearly independent and no unique solution for them can be found. The momenta of the decay pions determine the effective mass of X^-

$$m_{X^-}^2 = \left\{ \sum_1^3 (P_i^2 + m_i^2)^{1/2} \right\}^2 - \left\{ \sum_1^3 \vec{P}_i \right\}^2 . \tag{3.4}$$

Since $\vec{p}_1$ is known, $\vec{p}_3$ is measured with the MMS and the directions of the decay pions with the wide-gap wire chamber system. The $m_{X^-}^2$ is obtained without using a magnet.

Energy conservation in reaction (3.1) gives the possibility of eliminating "wrong events", i.e. events where π^0's are involved, the decay particles are not pions, or only three charged pions are detected from a five-pion decay.

The energy difference before and after the reaction is called ΔE, given by

$$\Delta E = \sum_1^3 (P_i^2 + m_i^2)^{1/2} + (p_3^2 + m_3^2)^{1/2} - (p_1^2 + m_i^2)^{1/2} - M_2 \,. \tag{3.5}$$

This function ΔE depends on the decay particle directions, the momentum of the incident pion, and the proton momentum. It is zero for the ideal case of a three-pion decay and no measuring errors. The function ΔE is put to zero by variation of all variables, keeping the χ^2 minimum. The "wrong" events can be rejected by χ^2 cuts.

3.2 Experimental conditions

The experimental set-up is seen in Fig. 39. In a run in January 1967, A_2 mesons were produced in reaction (3.1) at an incident momentum of 7.0 GeV/c, and at a momentum transfer of $0.18 < |t| < 0.32$ $(GeV/c)^2$. During three PS-weeks*) of running, high statistics in the A_2 region were obtained with the MMS, while the vertex system was set up and tested during the first week. At the end of the second week and during most of the third week, the system was operating properly, thus giving a total of 58 hours of production run for the vertex system. In 65% of the measured events, all three pions from the A_2 went into the fiducial area of the wire chambers (solid angle $\pm 20°$).

3.3 Selection of events

The function ΔE for three charged particle events in the wire chambers is seen in Fig. 50. The peak around $\Delta E = 0$ contains the good events with $A_2^- \to \pi^+\pi^-\pi^-$, whereas most other events are in the tails. The mass spectrum for the total sample is shown in Fig. 51. After variation of the parameters and a χ^2 cut, the mass spectrum shows an enhanced A_2 peak on top of a three-body phase space (Fig. 52). The cut events are plotted in Fig. 53. They show what one would expect from a high multiplicity phase space. The small A_2 peak is due to uncertainty in the χ^2 cut, and background from events which are not $A_2 \to \pi^+\pi^-\pi^-$. If one plots the missing mass of the proton minus effective mass of the three pions [formula (2.10)], a distribution peaked around zero containing long tails is found. Events accepted by our χ^2 cut correspond to the events inside the peak, while the long tails contain the rejected events. The χ^2-cut procedure selects with high probability three charged pions in the final state. For the analysis, events inside the A_2 from 1.26 GeV to 1.36 GeV were taken from the cleaned sample (Fig. 52) leaving us with 401 events.

---

*) One PS-week corresponds to about 90 hours.

3.4 Spin-parity analysis

In Section 1.4 we proved a two-peak structure of the A_2 meson. We find that to do a statistically significant separate J^P analysis of the two A_2 peaks is not possible with our present data, and we have therefore treated the mass region from 1.26 GeV to 1.36 GeV as one peak. This is equivalent to the assumption that both peaks have the same J^P, which is not proven. This procedure also enables us to compare our data with that of the bubble chamber.

A Dalitz plot has been constructed for the cleaned sample (Fig. 54). For each of the 401 events we have plotted six points, since we cannot distinguish between the charges. The projection of the Dalitz plot is shown in Fig. 55. The density distribution as well as the radial distribution of one sextant of the Dalitz plot depend on the spin-parity of the resonance in question. We have therefore fitted our data using the theoretical distribution suitably folded to give the corresponding density in the sextant. In the analysis, an incoherent mixture of resonance and two background terms have been assumed. For the resonant term we have used the theoretical distributions of Zemach[67] for the $\rho\pi$ decay of a 3π resonance. We assume a Breit-Wigner resonance of mass M = 1.307 GeV and width Γ = 0.095 GeV[5]. For the background we assume two terms:

- a $\rho\pi$ background with a distribution uniform in the ρ band;
- a 3π background uniformly distributed over the whole Dalitz plot[68-71].

To describe the events, we have used as variables the three-pion effective mass M and the polar coordinates r and Θ within the sextant of the Dalitz plot. From r we define a new variable $S = (r/R)^2$, where R is the distance from the centre to the edge of the Dalitz plot. The quantities r, R, and Θ are shown in the insert of Fig. 56.

In order to obtain a maximum of information regarding the relative amounts of resonance and background terms, we have analysed the data using a maximum likelihood method. The likelihood is calculated as a function of the three variables M, S, and Θ. The logarithm of the likelihood is shown in Fig. 56 as a function of α_{J^P} (the percentage of resonance) and $\alpha_{\rho\pi}$ (the percentage of $\rho\pi$ background). The percentage of uniform background

$\alpha_{3\pi}$ is then given by $\alpha_{3\pi} = 100\% - \alpha_{J^P} - \alpha_{\rho\pi}$. The best likelihood for the hypothesis $J^P = 2^+$ is obtained with 50% A_2 resonance, 10% $\rho\pi$ background, and 40% uniform background. The percentage of resonance is in good agreement with the value of (50 ± 3)% obtained from the A_2 mass spectrum (Fig. 52).

We have also analysed the data with a χ^2 test to obtain the goodness of fit of our J^P hypotheses. To obtain a χ^2 we have considered the radial distribution in the sextant, since the 2^+ and 2^- hypotheses differ most strongly in the behaviour near the edge of the Dalitz plot (i.e. near S = 1). The experimental data, together with the fits for 2^+ and 2^-, are shown in Fig. 56. In both cases we have assumed 50% of resonance. The χ^2 analysis shows that $J^P = 2^+$ is favoured with a confidence level of $P(\chi^2) = 16\%$ over 2^- (P-wave) with $P(\chi^2) = 0.5\%$. For the hypotheses 1^- and 1^+ (S-wave) we find $P(\chi^2) = 0.15\%$ and 0.7%, respectively.

3.5 Biases

Two kinds of experimental biases have been examined in detail:

i) Geometrical biases due to limited solid angle of the system and losses by the beam killer in the centre of the chambers. The total loss due to geometrical cuts amounts to 35%.

ii) Since our method fails for coplanar events, they fall into the tails of the χ^2 distribution and are removed. This loss amounts to 25%.

The χ^2 fits to the corrected data have been found to be statistically indistinguishable from the uncorrected ones. A possible polarization of the A_2 has not been taken into account.

3.6 Conclusions

a) From the observation of a strong A_2 enhancement and its projection showing a clean ρ, we conclude that the feasibility of measuring effective mass and obtaining an on-line Dalitz plot with our wire chamber technique without magnetic field has been proven.

b) We conclude that the three-pion decay distribution in the A_2 region ($1.26 < M < 1.36$ GeV) is consistent with spin-parity 2^+ and does not fit 2^-. This result is in agreement with the analysis of the neutral A_2 in bubble chamber experiments. For the charged A_2, bubble

chamber experiments have given results of 2^+ at 3.2 GeV/c and 4.2 GeV/c, and at higher energies similar to ours both 2^+ and 2^-. Our experiment differs from these bubble chamber experiments in that we only have events for $|t|$ values between 0.16 and 0.28 $(GeV/c)^2$. We believe that there is a difference in the background due to the larger $|t|$ value; in particular, we expect the background from the A_1 resonance and Deck effect[72] to be smaller in our data.

* * *

Acknowledgements

I am extremely grateful to Prof. B. Maglić, who made it possible for me to join his group, and who always helped and supported my work, and also to Prof. G. E. Chikovani, the best teacher one could find. I am very indebted to Dr. W. Kienzle for his help during all stages.

I would like to thank Prof. J. Geiss, who allowed me to go to CERN and supported my efforts to start a collaboration between Bern and CERN. My warm thanks go to the members of the Missing Mass team, namely Mr. L. Dubal, Dr. M.N. Focacci, Mr. G. Laverrière, Mlle. C. Lechanoine, Dr. B. Levrat, Dr. M. Martin, Mr. Ch. Nef, and Dr. J. Seguinot; I am grateful to Mr. R. Klanner for his reading of the manuscript; and I would like to express my appreciation to Prof. H. Leutwyler who always helped me with theoretical discussions and practical advice, and also to Prof. Ch. Peyrou for his assistance and interest in my work.

I am grateful to Profs. G. Cocconi, W. Paul and P. Preiswerk for the hospitality extended to me by the Nuclear Physics Division at CERN.

I would also like to thank the Schweiz. Nationalfonds for their support.

REFERENCES

1) B. Maglić and G. Costa, Physics Letters 18, 185 (1965).

2) H.R. Blieden, D. Freytag, J. Geibel, A.R.F. Hassan, W. Kienzle, F. Lefébvres, B. Levrat, B.C. Maglić, J. Séguinot and A.J. Smith, Physics Letters 19, 444 (1965).

3) M.N. Focacci, W. Kienzle, B. Levrat, B.C. Maglić and M. Martin, Physics Letters 17, 890 (1966).

4) B. Levrat, C.A. Tolstrup, P. Schübelin, C. Nef, M. Martin, B.C. Maglić, W. Kienzle, M.N. Focacci, L. Dubal and G. Chikovani, Physics Letters 22, 714 (1966).

5) W. Kienzle, C. Lechanoine, B. Levrat, B.C. Maglić, M. Martin, P. Schübelin, L. Dubal, M. Fischer, P. Grieder, H.A. Neal and C. Nef, Physics Letters 25B, 44 (1967).

6) J.D. Jackson, Nuovo Cimento 34, 1644 (1964).

7) M.L. Goldberger and K.M. Watson, Phys.Rev. 136B, 1472 (1964).
J.S. Bell and C.J. Goebel, Phys.Rev. 138B, 1198 (1965).

8) M.L. Goldberger and K.M. Watson, Collision theory (J. Wiley, New York, 1964).

9) J. Séguinot, M. Martin, B.C. Maglić, B. Levrat, F. Lefèbvres, W. Kienzle, M.N. Focacci, L. Dubal, G. Chikovani, C. Bricman and P. Bareyre, Physics Letters 19, 712 (1966).

10) L. Dubal, M.N. Focacci, W. Kienzle, B.C. Maglić, M. Martin, P. Schübelin, G. Chikovani, M. Fischer, P. Grieder, H.A. Neal and C. Nef, Experimental confirmation of R-meson structure, submitted to Nuclear Phys. B.

11) J.A. Danysz, B.R. French, J.B. Kinson, V. Simak, J. Clayton, P. Masson, A. Muirhead and P. Renton, Physics Letters 24B, 309 (1967).

12) J.C. Crennel, P.V.C. Hough, G.R. Kalbfleisch, K.W. Lai, J.M. Scarr, T.G. Schumann, I.O. Skillicorn, R.C. Strand, M.S. Webster, P. Baumel, A.H. Bachman and R.L. Lea, Phys.Rev.Letters 18, 323 (1967).

13) A. Forino, G. Cessaroli, L. Lendinara, G. Quareni, A. Quareni-Vignudelli, A. Romano, J. Laberrigue-Frolow, J. Quinquart, M. Sené, W. Fickinger, O. Goussu and A. Rogozinski, Physics Letters 19, 65 (1965).

14) N. Armenise, B. Ghidini, V. Picciarelli, A. Romano, A. Forino, G. Cessaroli, L. Lendinara, G. Quareni, A. Quareni-Vignudelli, A. Cartucci, M.G. Dagliana, G. di Caporiaco, G. Parrini, M. Barrier, O. Goussu, J. Laberrigue-Frolow, D. Mettel, N.H. Khanh and J. Quinquart, "A_2^0 production in $\pi^+ d$ interaction" (to be published).

15) R.H. Dalitz, Proc. of XIII Int.Conf. on High-Energy Physics, Berkeley, 1966 (Univ. of Calif. Press, 1967), p.215.

16) G. Chikovani, L. Dubal, M.N. Focacci, W. Kienzle, B. Levrat, B.C. Maglić, M. Martin, C. Nef, P. Schübelin and J. Séguinot, Phys.Letters 22, 233 (1966).

17) R.J. Abrams, R.L. Cool, G. Giacomelli, T.F. Kycia, B.A. Leontic, K.K. Li and D.N. Michael, BNL 11356 (1967).

18) G. Goldhaber, UCRL-17696 (1967).

19) S.J. Lindenbaum, Physics Today 18, 4 (1965).

20) G.E. Chikovani, G.C. Laverrière and P. Schübelin, Nucl.Instr.and Methods 47, 273-276 (1967).

21) S. Fukui and S. Miyamoto, Nuovo Cimento 11, 113 (1959).

22) A.A. Borisov, B.A. Dogolshein, B.I. Luchkov, L.V. Reshetin and V.I. Ushakov, Pribory Tekh.Eksper. 1, 49 (1962).

23) G.E. Chikovani, V.N. Roinishvili and V.A. Mikhailov, Report given at the Nuclear Electronics Conference, Moscow (1961).

24) V.N. Bolotov, M.L. Dayon, M.I. Devishev, L.F. Klimanova, B.I. Luchkov and A.P. Shmeleva, Proc. 5th Int.Conf. on Cosmic Rays, India (1963), p.534.

25) A.I. Alikhanyan, T.L. Asatiani and E.M. Matevosian, JETP 17, 522 (1963).
A.I. Alikhanyan, T.L. Asatiani, E.M. Matevosian and R.O. Sharkhatunian, Physics Letters 4, 295 (1963).

26) V.A. Lyubimov and F.A. Pavlovsky, JETP 46, 1143 (1964).

27) J.P. Garron, D. Grossman and K. Strauch, Rev.Sci.Instr. 63, 264 (1965).

28) V.A. Mikhailov, V.N. Roinishvili and G.E. Chikovani, JETP 45, 10 (1963).
G.E. Chikovani, V.N. Roinishvili and V.A. Mikhailov, Physics Letters 6, 254 (1963).
G.E. Chikovani, V.N. Roinishvili and V.A. Mikhailov, Proc. 5th Int. Conf. on Cosmics Rays, India (1963), p.517.

29) G.E. Chikovani, V.A. Mikhailov and V.N. Roinishvili, JETP 46, 1228 (1964).
G.E. Chikovani, V.A. Mikhailov and V.N. Roinishvili, Nucl.Instr. and Methods 29, 261 (1964).

30) G.E. Chikovani, V.A. Mikhailov, V.N. Roinishvili and A.K. Djavrishvili, Nucl.Instr. and Methods 35, 193 (1965).

31) B.A. Dogolshein and B.I. Luchkov, JETP 46, 392 (1964).
B.A. Dogolshein and B.I. Luchkov, Proc. 5th Int.Conf. on Cosmic Rays, India (1963), p.530.

32) B.A. Dogolshein, B.I. Luchkov and B.U. Rodionov, JETP 46, 1953 (1964).

33) F. Bulos, A. Boyarski, R. Diebold, A. Odian, B. Richter and F. Villa, SLAC-PUB-140 (Sept. 1965).

34) E. Gygi and F. Schneider, Proc. Informal Meeting on Filmless Spark Chamber Techniques and Associated Computer Uses, CERN 64-30 (1964), p.351.

35) F. Krienen, Nucl.Instr. and Methods 16, 262 (1962).

36) B.C. Maglić and F.A. Kirsten, Nucl.Instr. and Methods 17, 49 (1962).

37) V. Perez-Mendez, IEEE Trans.Nucl.Sci. Vol. NS-12, No. 4 (August 1965).

38) W. Vernon, Proc. Informal Meeting on Filmless Spark Chamber Techniques and Associated Computer Uses, CERN 64-30 (1964), p.57.

39) V. Barbanenete, M. De Blasi, C. De Marzo, G. Giannelli, B. Marangelli and M. Ricco, IEEE Trans.Nucl.Sci. NS-12, Vol. No. 4 (August 1965).

40) G. Giannelli, Proc. Frascati Congress (1963), Report LNF 63/54 of Frascati National Laboratory.

G. Giannelli, Proc. Informal Meeting on Filmless Spark Chamber Techniques and Associated Computer Uses, CERN 64-30 (1964), p.325.

G. Giannelli, Nucl.Instr. and Methods 31, 29 (1964).

41) V. Perez-Mendez and J.M. Pfab, Nucl.Instr. and Methods 33, 141 (1965).

42) G. Charpak, L. Massonet and J. Favier, Nucl.Instr. and Methods 24, 501 (1963).

43) V. Perez-Mendez, Development in magnetostrictive read-outs for spark chambers (September 1966), University of California Lawrence Radiation Laboratory, Berkeley, Calif., AEC Contract No. W-7405-eng-48.

44) V. Perez-Mendez and J.M. Pfab, Nucl.Inst. and Methods 33, 141 (1965).

45) F. Kirsten, V. Perez-Mendez and J. Pfab, Lawrence Radiation Laboratory, Report UCID-2629 (August 1965).

46) Th.J. Devlin, Th.F. Droege, V. Perez-Mendez and J. Solomon, Princeton, Penn. Acc. Report PPAD-85-E (March 1966), Nucl.Instr. and Methods 46, 197 (1967).

47) F. Bradamante and F. Sauli, University of Trieste Report INFN/Ae-66/2 (1966).

48) F.A. Kirsten, K.L. Lee and J. Conragan, IEEE Trans.Nucl.Sci. Vol. NS-13, No. 3, 583 (June 1966).

49) A. Grove, V. Perez-Mendez and K.L. Lee, Lawrence Radiation Laboratory Report UCID-2839 (September 1966).

50) L. Kaufman, V. Perez-Mendez and J.M. Pfab, IEEE Trans.Nucl.Sci. Vol. NS-13, No. 3, 578 (June 1966).

51) L. Kaufman, V. Perez-Mendez and J.M. Pfab, Magnetostrictive and piezoelectric read-out of spark chambers in magnetic fields, Lawrence Radiation Laboratory, University of California, Berkeley, (private communication).

52) G. Brautti, Organization of spark chambers with magnetostrictive read-out, CERN 66-30 (1966).

53) J. Fischer, Digitized spark chambers at BNL, Internal Report BNL 10576.

54) J. Fischer, Digitized printed discharge planes and their operation at rapid rates, IEEE Trans.Nucl.Sci. Vol. NS-12, No. 4, 37 (1965). (Also BNL 9260.)

55) E. Bleser, G.B. Collins, J. Fischer, T. Fujii, S. Heller, W. Higinbotham, J. Menes, H. Pate, F. Turkot and N.C. Hien, Design and performance of an on-line wire spark chamber spectrometer for 5 to 30 BeV/c particles, Nucl.Instr. and Methods, to appear shortly. (Also BNL 9897.)

56) W.A. Higinbotham, J.F. Jacobs, H.R. Pate, IEEE Trans.Nucl.Sci. Vol. NS-12, No. 1, 386 (1965).

57) J. Fischer, Proc. 7th Conf. on Phenomena in Ionized Gases, Belgrade (1965), p.135. (Also BNL 9443.)

58) J.M. Meek and J.D. Craggs, Electrical breakdown of gases (Clarendon Press, Oxford, 1953).

59) J.S. Townsend, Electrons in gases (Hutchinson 1947).

60) J.S. Townsend, Electricity in gases, (Oxford, 1914).

61) L.B. Loeb, Fundamental processes of electrical discharges in gases, (J. Wiley, New York, 1939).

62) A.A. Kruithof and F.M. Penning, Physica 3, 515 (1936); 4, 430 (1937).

63) J.M. Meek, Phys.Rev. 57, 722 (1940).

64) H. Raether, Arch.Elektrotech. 34, 49 (1940).

65) M.I. Daion and G.A. Leksin, Soviet Phys. Uspekhi 6, 428 (1963).

66) G.E. Chikovani, M. Fischer, M.N. Focacci, W. Kienzle, G. Laverrière, C. Lechanoine, B. Levrat, M. Martin and P. Schüblin, CERN 67-13 (1967).

67) Zemach, Phys.Rev. 153, B1201 (1964).

68) G. Benson, L. Lovell, E. Marquit, B. Roe, D. Sinclair and J. Van der Velde, Phys.Rev.Letters 16, 1177 (1966).

H.O. Cohn, R.D. McCullock, W.M. Bugg, G.T. Condo, Nuclear Phys. B1, 57 (1967).

69) S.U. Chung, O.I. Dahl, L.M. Havely, R.J. Hess, J. Kirz and D.H. Miller, Phys.Rev.Letters 18, 100 (1967).

70) V.E. Barnes, W.B. Fowler, K.W. Lai, S. Orenstein, D. Radojicic, M.S. Webster, A.H. Backman, P. Blaumel and R.M. Lea, Phys.Rev.Letters 16, 41 (1966).

71) N.M. Cason, Phys.Rev. 148, 1282 (1966).

72) R.T. Deck, Phys.Rev.Letters 13, 169 (1964).

CURRICULUM VITAE

I was born on 21.5.1940 in Bern, the son of Walter Schübelin and his wife Marie. In Belp, I completed my primary school within four years, entered the secondary school in 1951, and then changed to the Progymnasium in Bern in 1953. In 1959 I passed my Matura, type B, at the Städt. Gymnasium in Bern. In the same town I studied physics under the late Prof. F. Houtermans and achieved my diploma in 1965. Immediately after, it became possible for me to join the Missing Mass Spectrometer experiment at CERN, starting a collaboration between the Physics Institute of Bern University and CERN. In the person of Prof. B. Maglić, leader of the MMS experimental group, I had a dynamic teacher who guided and supervised my work.

* * *

Fig. 1a : Kinematics for $\pi p \rightarrow pX$ at $p_1 = 5$ GeV/c and $M_X = 0.760$ GeV

The lab. angle θ_3 of the recoil proton is plotted versus the c.m. angle θ_3^*. θ_3 reaches a maximum where the Jacobian, i.e. $d(\cos \theta_3^*)/d(\cos \theta_3)$, becomes infinite.

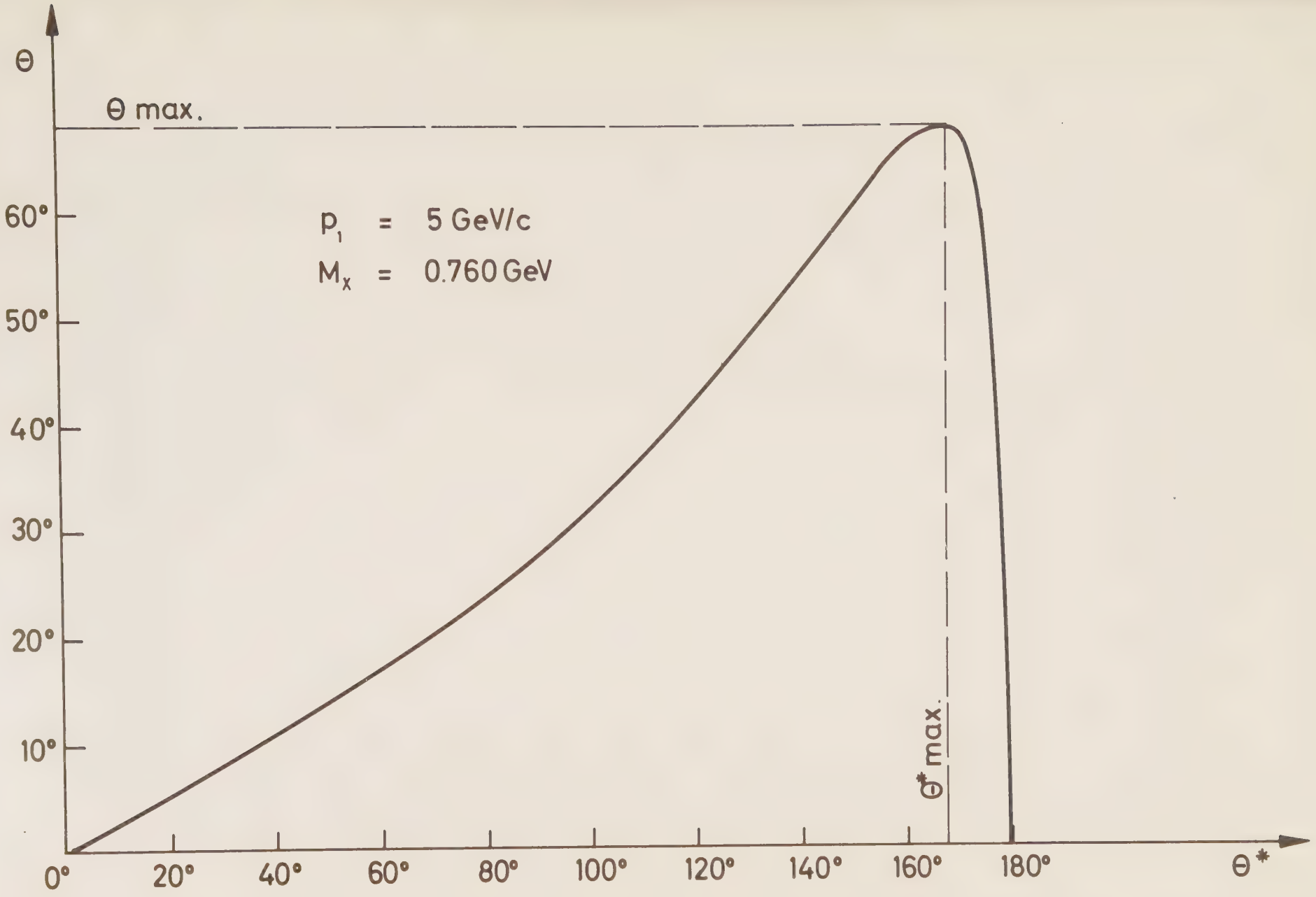
Θ
Θ max.
60°
50°
40°
30°
20°
10°
p_1 = 5 GeV/c
M_X = 0.760 GeV
Θ* max.
0°
20°
40°
60°
80°
100°
120°
140°
160°
180°
Θ*

FIG. 1a

Fig. 1b : Lab. angle Θ_3 versus momentum p_3 of the recoil proton at $p_1 = 5.0$ GeV/c and different masses M_X

With increasing M_X, the Jacobian peak (Θ_3^{max}) is shifting towards higher p_3 while Θ_3^{max} is decreasing.

FIG.1b

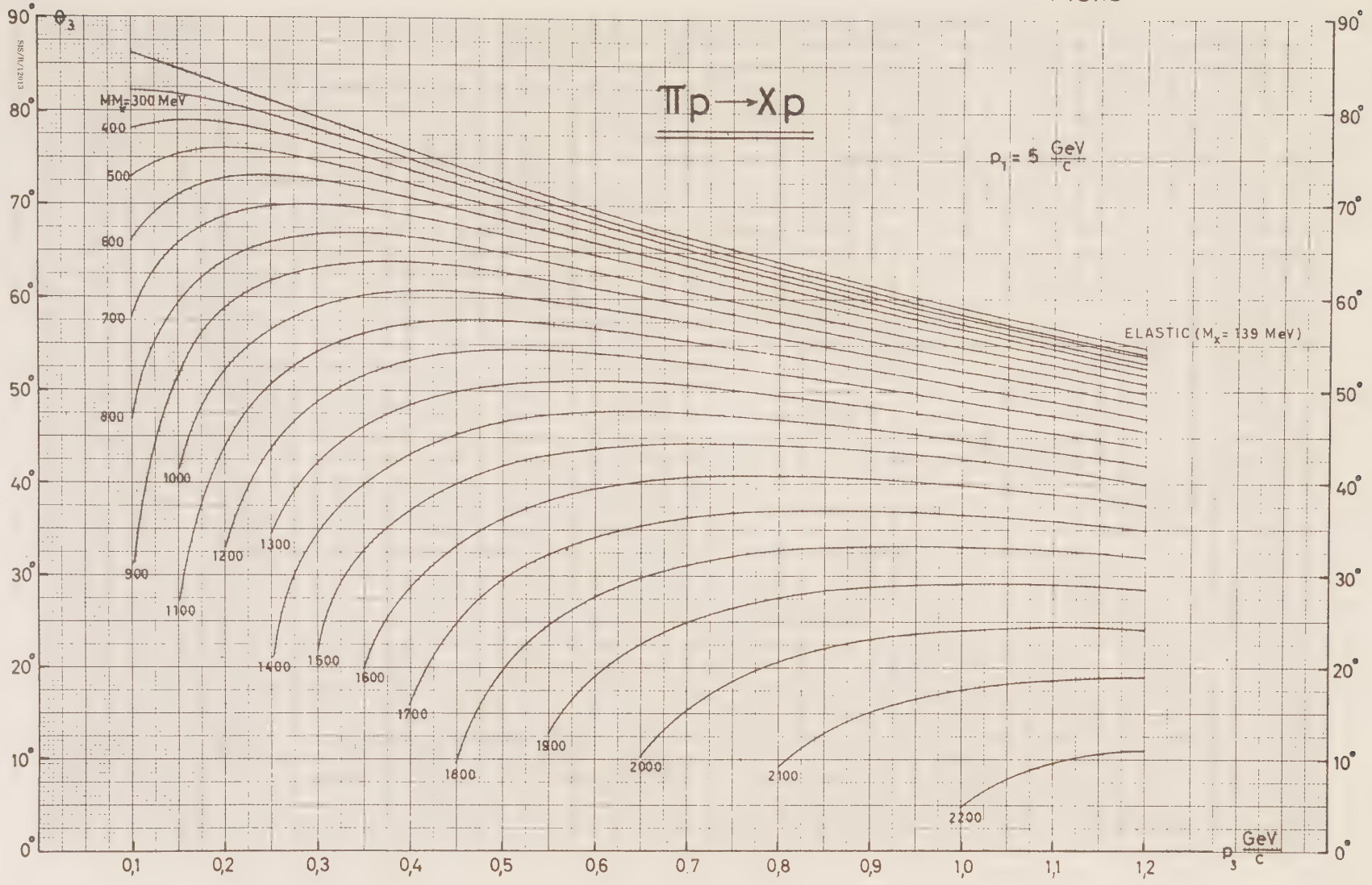
$\pi p \rightarrow X p$
$p_1 = 5\ \frac{GeV}{c}$
θ_3
MM_x=300 MeV
400
500
600
700
800
900
1000
1100
1200
1300
1400
1500
1600
1700
1800
1900
2000
2100
2200
ELASTIC (M_x= 139 MeV)
$p_3\ \frac{GeV}{c}$
0°
10°
20°
30°
40°
50°
60°
70°
80°
90°
0,1
0,2
0,3
0,4
0,5
0,6
0,7
0,8
0,9
1,0
1,1
1,2

Fig. 2 : Lab. angle distribution $d\sigma/d\Theta$ of the recoil protons for isotropic and anisotropic c.m. distribution

The dashed curve shows the enhancement at Θ_3^{max} coming from pure kinematics, i.e. the proton is emitted isotropically in the c.m. (this corresponds to a pure solid-angle transformation). The full curve shows the enhancement due to kinematics plus dynamics, i.e. the proton is emitted strongly backward in the c.m. due to peripheral collision.

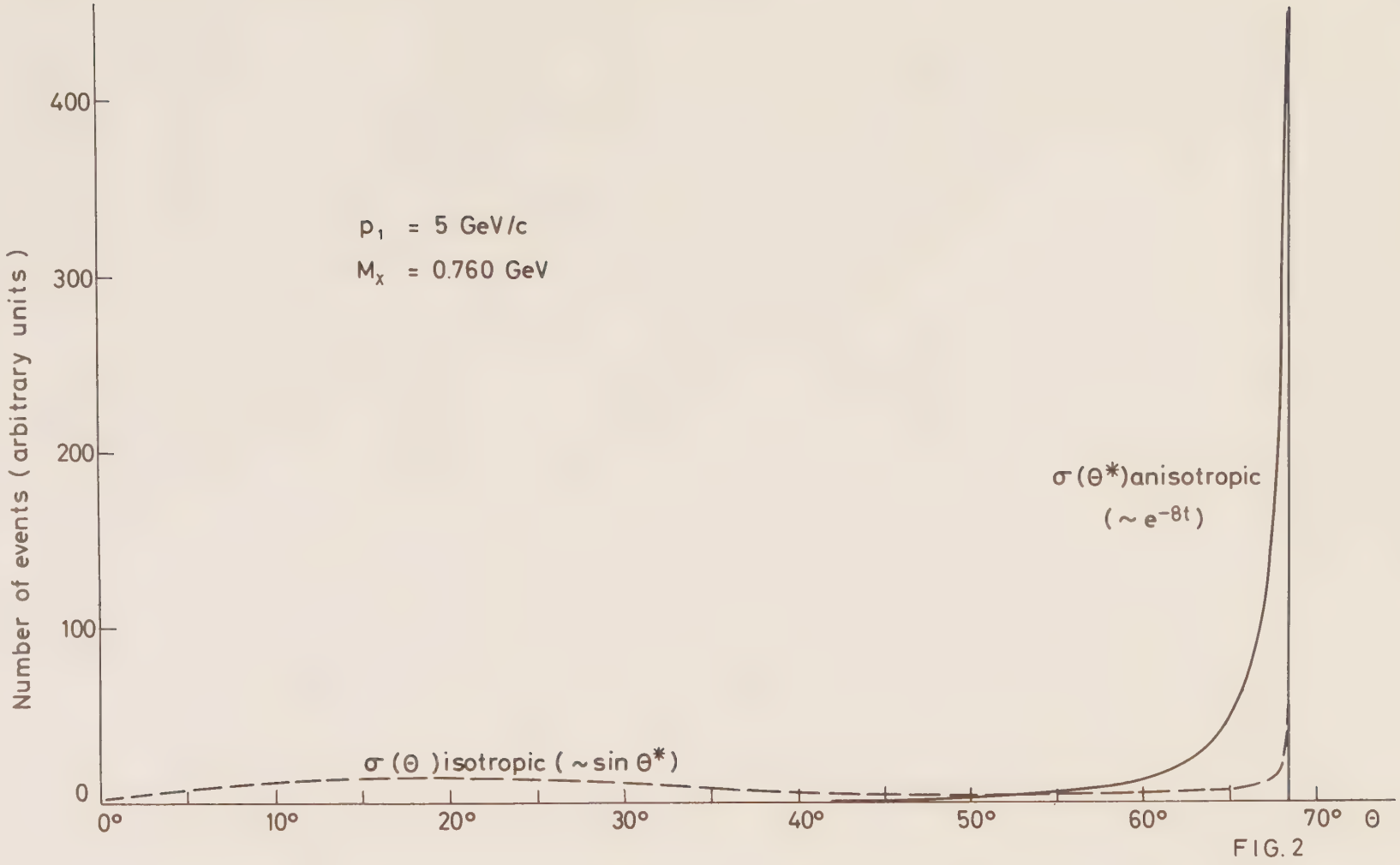
400
300
200
100
0
Number of events (arbitrary units)
p_1 = 5 GeV/c
M_X = 0.760 GeV
$\sigma(\Theta^*)$anisotropic
$(\sim e^{-8t})$
$\sigma(\Theta)$isotropic $(\sim \sin\Theta^*)$
0°
10°
20°
30°
40°
50°
60°
70°
Θ

FIG. 2

Fig. 3 : Set-up of CERN MMS (as of November 1966)

H1, H2,	Incident beam hodoscopes
SCI - SC IV	Sonic spark chambers for recoil proton location
R's and P's	Scintillation counters for the trigger and the recoil proton range determination
VM	72-element scintillation counter matrix
V's, $\bar{B}$	Scintillation counters for additional vertex requirements
T	Time zero counter for time-of-flight

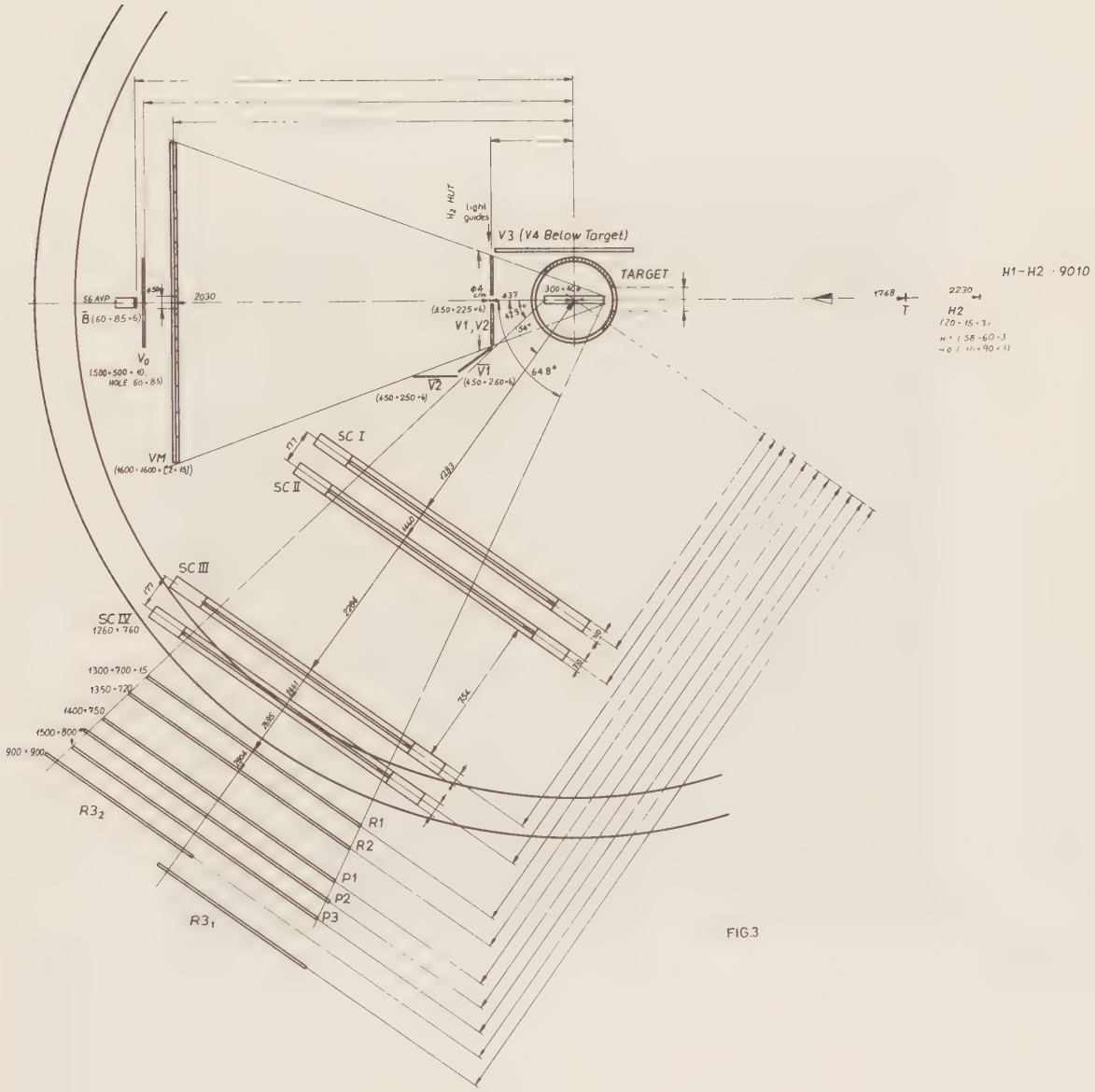
H1-H2 · 9010
H2 HUT
light guides
V3 (V4 Below Target)
TARGET
SC AVP
B (60 · 85 · 6)
V0
(500 · 500 · 10, HOLE 60 · 85)
VM
V1, V2
V1
V2
(450 · 250 · 4)
SC I
SC II
SC III
SC IV
1260 · 760
1300 · 700 · 15
1350 · 720
1400 · 750
1500 · 800
900 · 900
R3₂
R3₁
R1
R2
P1
P2
P3
T
H2
120 · 15 · 3
H + (58 · 60 · 3
H0 (1/1 · 90 · 3)

FIG.3

Fig. 4 : Visual output from CDC 6600 on-line on TV screen in the experimental area. After 90 minutes of data sampling, a clear A_2 peak and part of the R peak are seen.

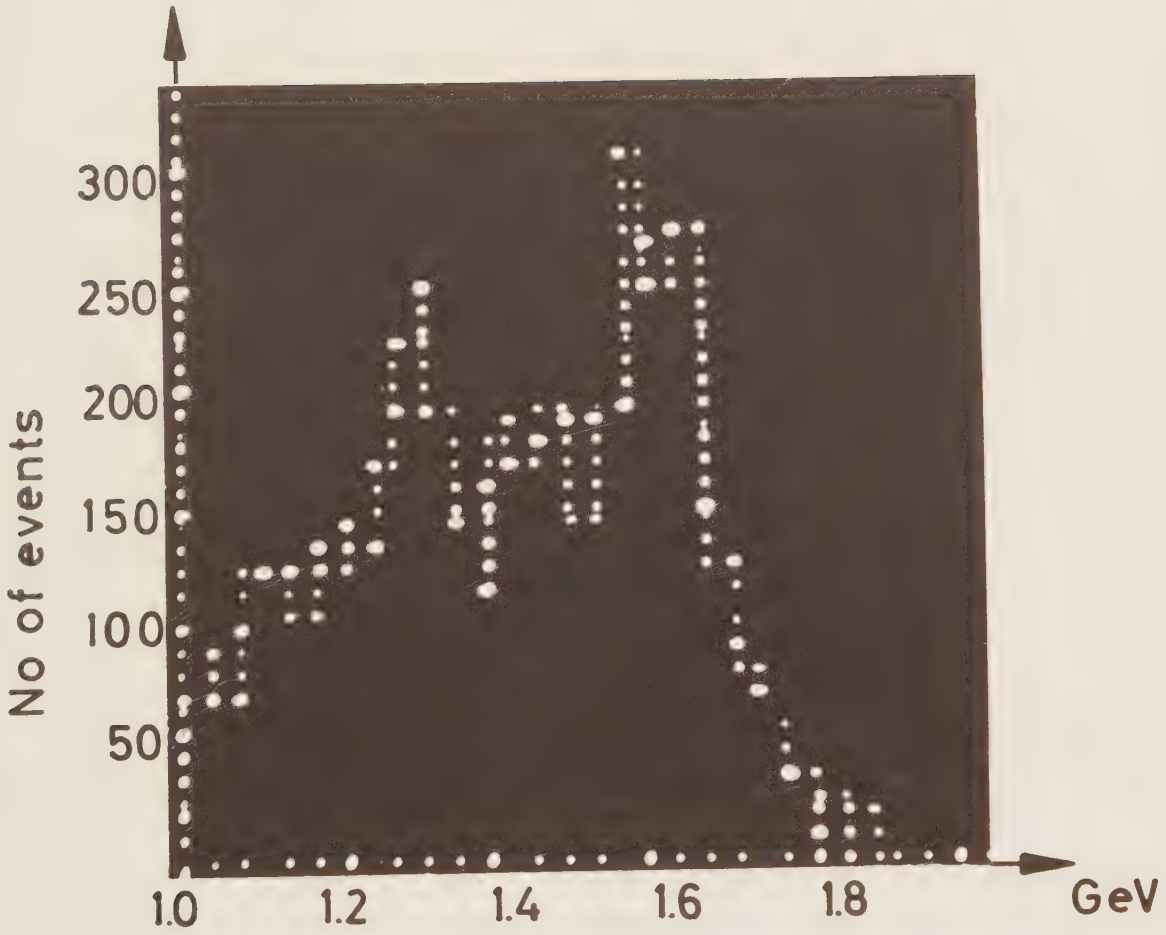

FIG. 4

Fig. 5 : Compiled spectrum of bosons X^- of isotopic spin I = 1 or 2, produced in the reaction $\pi^- p \rightarrow pX^-$, observed by the CERN missing-mass spectrometer. The incident pion momentum p_π is indicated below each peak. The area under each peak corresponds to its differential cross-section $d\sigma/dt$, normalized to $\bar{t} = 0.2$ $(GeV/c)^2$ using the observed $d\sigma/dt$ versus $|t|$ dependence. For convenience of presentation, the spectrum has been scaled up by a factor of 2 in the region of the δ meson (900-1000 MeV) and the R meson (1530-1810 MeV) and scaled down in the region of the A_2 meson (1150-1530 MeV) by a factor of 2. The dashed lines at the bottom indicate two mass bands (1000-1150 and 1450-1570 MeV) which have not been covered by the full efficiency of the spectrometer in any run. The errors are statistical.

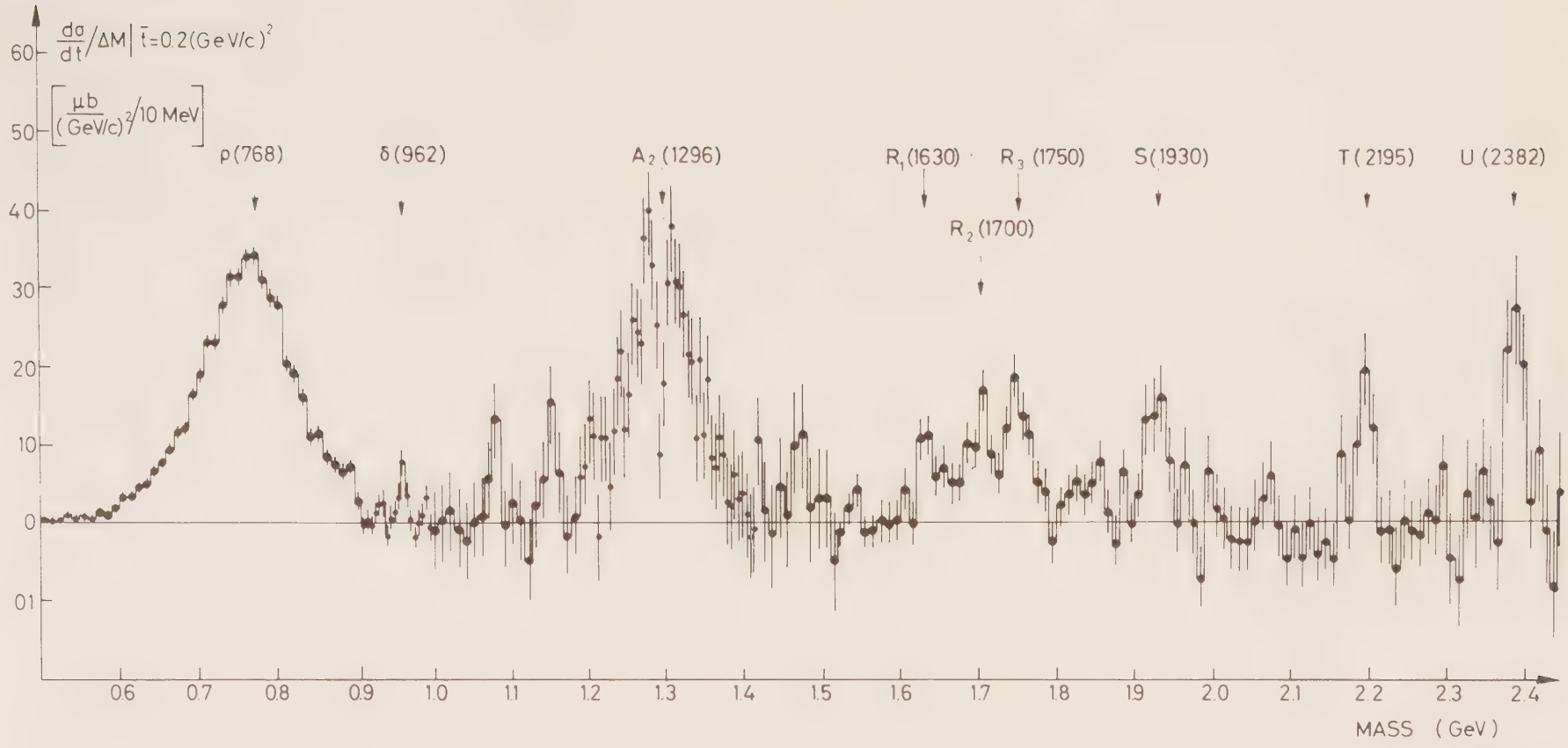
$\frac{d\sigma}{dt}/\Delta M \Big|_{\bar{t}=0.2(GeV/c)^2}$
$\left[\frac{\mu b}{(GeV/c)^2/10\,MeV}\right]$
60
50
40
30
20
10
0
01
ρ(768)
δ(962)
A_2(1296)
R_1(1630)
R_3(1750)
R_2(1700)
S(1930)
T(2195)
U(2382)
0.6
0.7
0.8
0.9
1.0
1.1
1.2
1.3
1.4
1.5
1.6
1.7
1.8
1.9
2.0
2.1
2.2
2.3
2.4
MASS (GeV)

FIG.5

Fig. 6 : Total A_2 data from January 1967 run. p_1 = 7.0 GeV/c and $0.18 < t < 0.32$ $(GeV/c)^2$. 4000 events are above background in the A_2 peak. Bin size = 15 MeV.

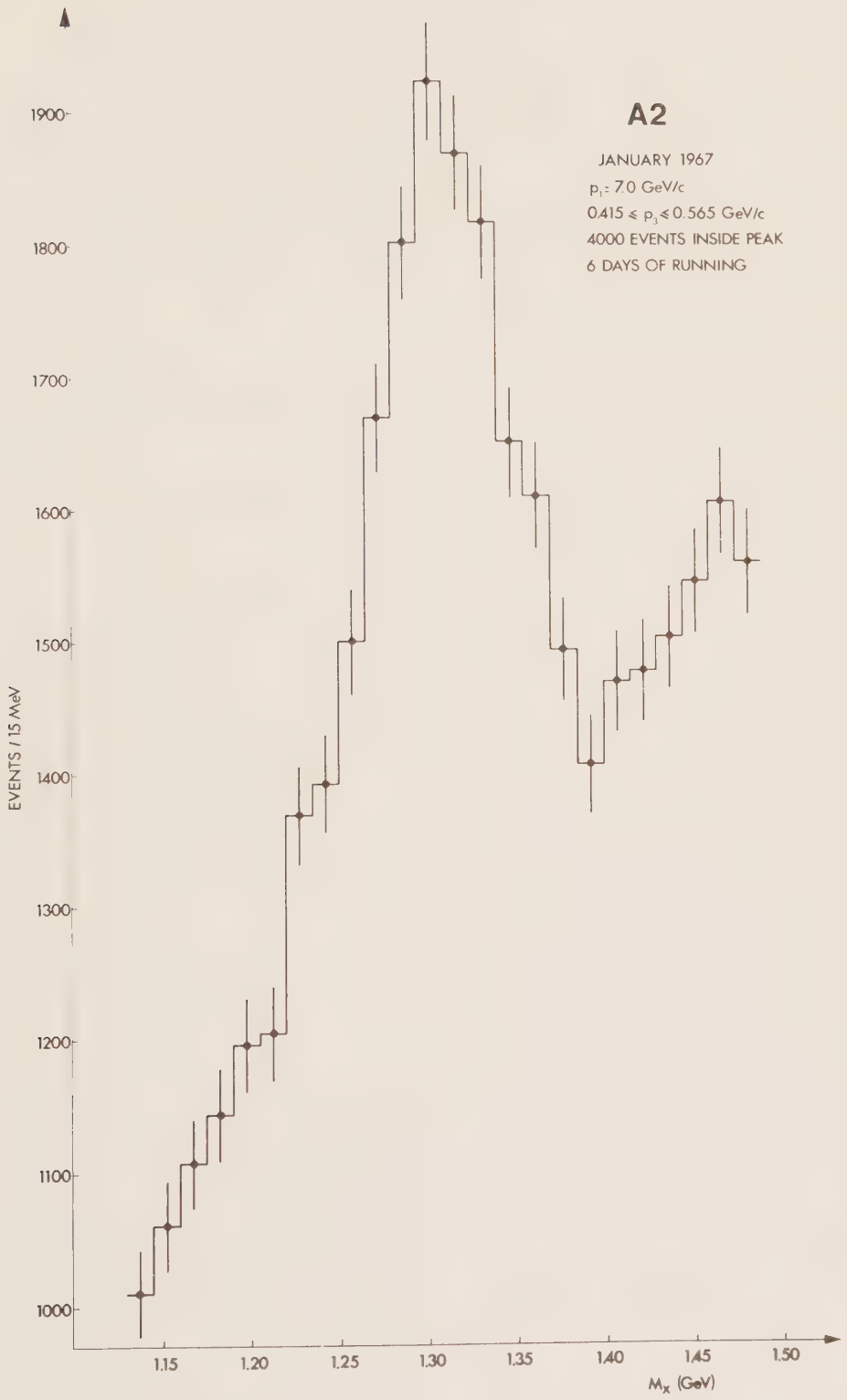
A2
JANUARY 1967
p_1 = 7.0 GeV/c
0.415 ≤ p_3 ≤ 0.565 GeV/c
4000 EVENTS INSIDE PEAK
6 DAYS OF RUNNING
EVENTS / 15 MeV
1900
1800
1700
1600
1500
1400
1300
1200
1100
1000
1.15
1.20
1.25
1.30
1.35
1.40
1.45
1.50
M_X (GeV)

FIG.6

Fig. 7a : Kinematics for $\pi^- p \rightarrow pX^-$ (i.e. lab. angle θ versus momentum p_3 of the recoil proton) at $p_1 = 7.0$ GeV/c and different masses M_X. The centre of the proton telescope was set to $\theta = 56°$, the total angular acceptance going from 44.5° to 66.8°. The proton momentum p_3 was measured by range in five equal intervals (vertical lines, interval numbers 1 to 5), each of 30 MeV/c width.

Fig. 7b : Experimental mass resolution Γ_{exp} (full width) in MeV for the five range intervals and at $M_X = 1.30$ GeV. The resolution Γ_{exp} is best in interval numbers 3 and 4, since they are nearest to the "Jacobian peak" of the 1.30 GeV mass lines.

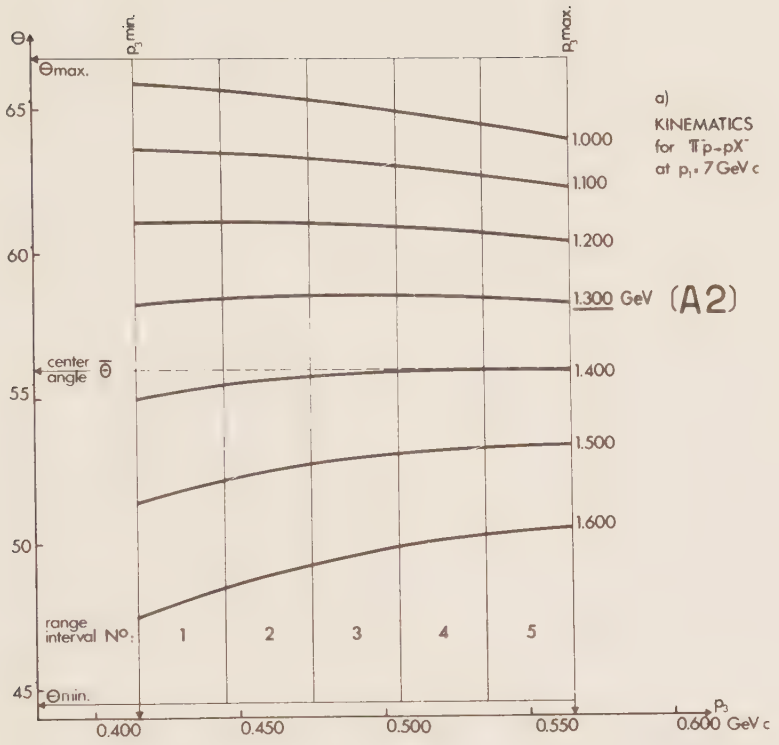
Θ
Θmax.
p3 min.
p3 max.
65
60
55
50
45
center angle Θ̄
Θmin.
1.000
1.100
1.200
1.300 GeV
1.400
1.500
1.600
range interval No:
1
2
3
4
5
0.400
0.450
0.500
0.550
0.600 GeV c
p3
a)
KINEMATICS
for π⁻p→pX⁻
at p1 = 7 GeV c
(A2)

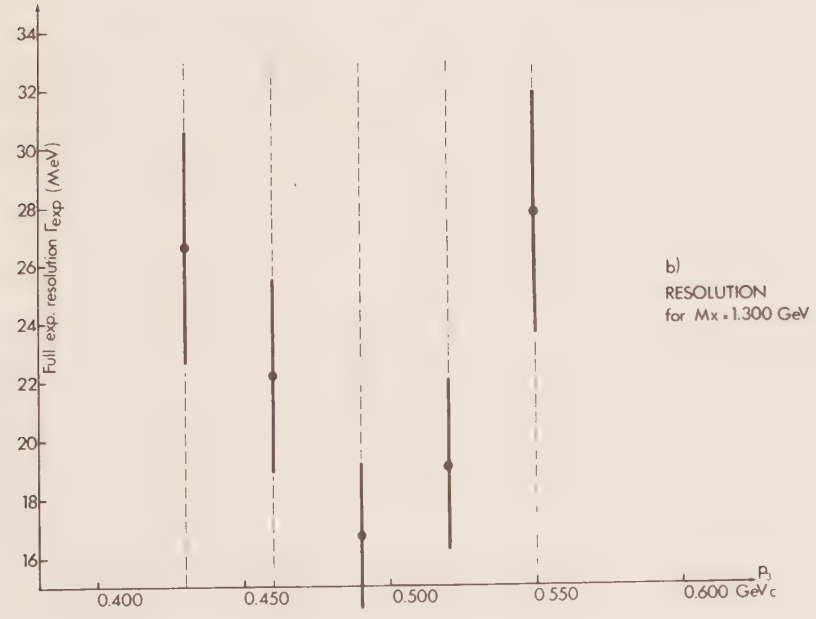
Full exp. resolution Γexp (MeV)
34
32
30
28
26
24
22
20
18
16
0.400
0.450
0.500
0 550
0.600 GeV c
p3
b)
RESOLUTION
for Mx = 1.300 GeV

FIG. 7

Fig. 8 : A_2 region for the five different range intervals, i.e. for five different experimental resolutions Γ_{exp}. In the samples 3 and 4, where the resolution is best, dips are seen in the centre of the A_2 peak. One bin $\Theta = 0.2°$ corresponds to $M_X = 8.0$ MeV in mass.

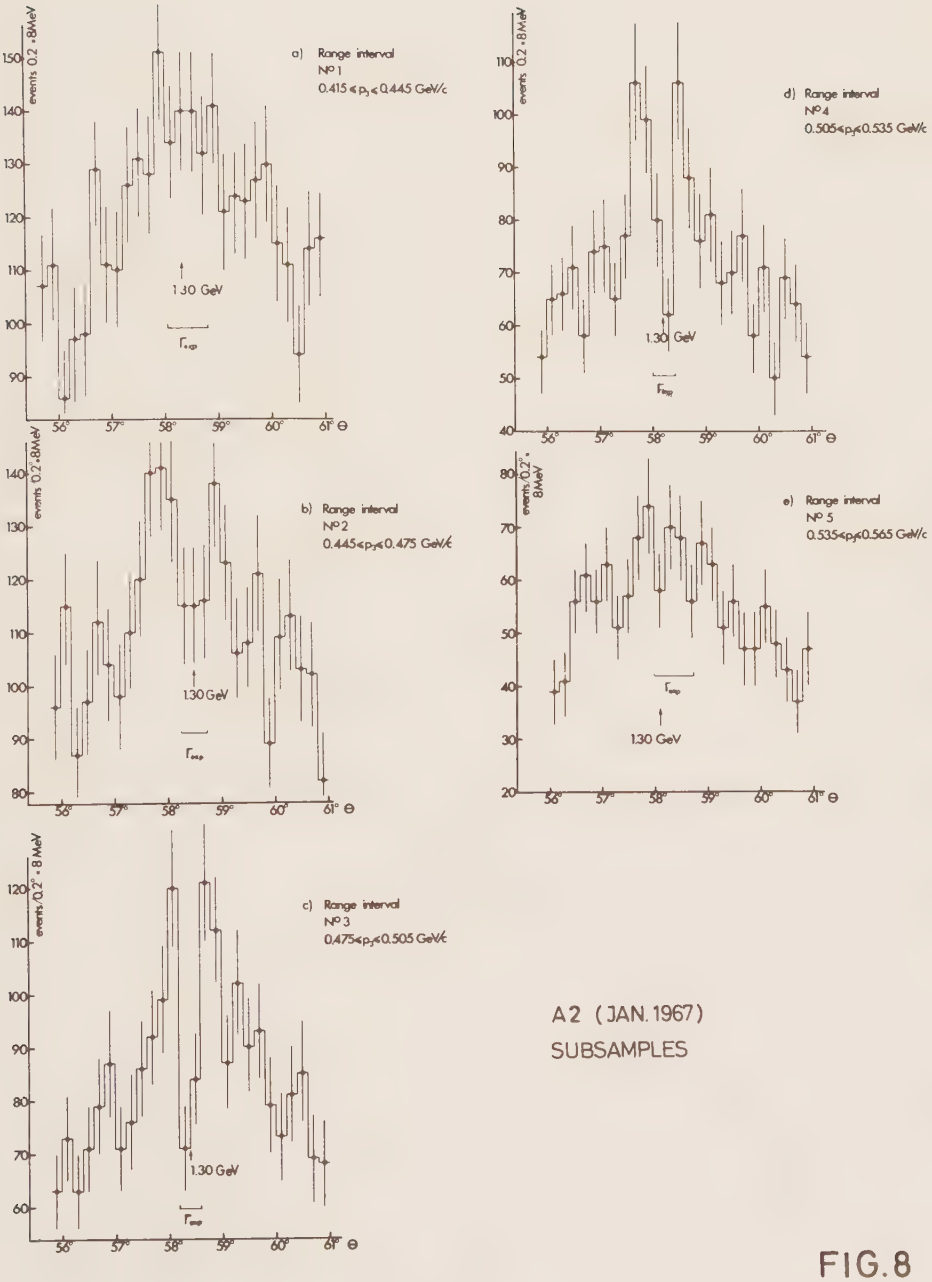

A2 (JAN. 1967)
SUBSAMPLES

FIG.8

Fig. 9 : A_2 best resolution sample. The two best resolution sub-samples of Fig. 8 (range intervals 4 and 3) have been added and plotted in bins of 0.1° = 4.0 MeV.

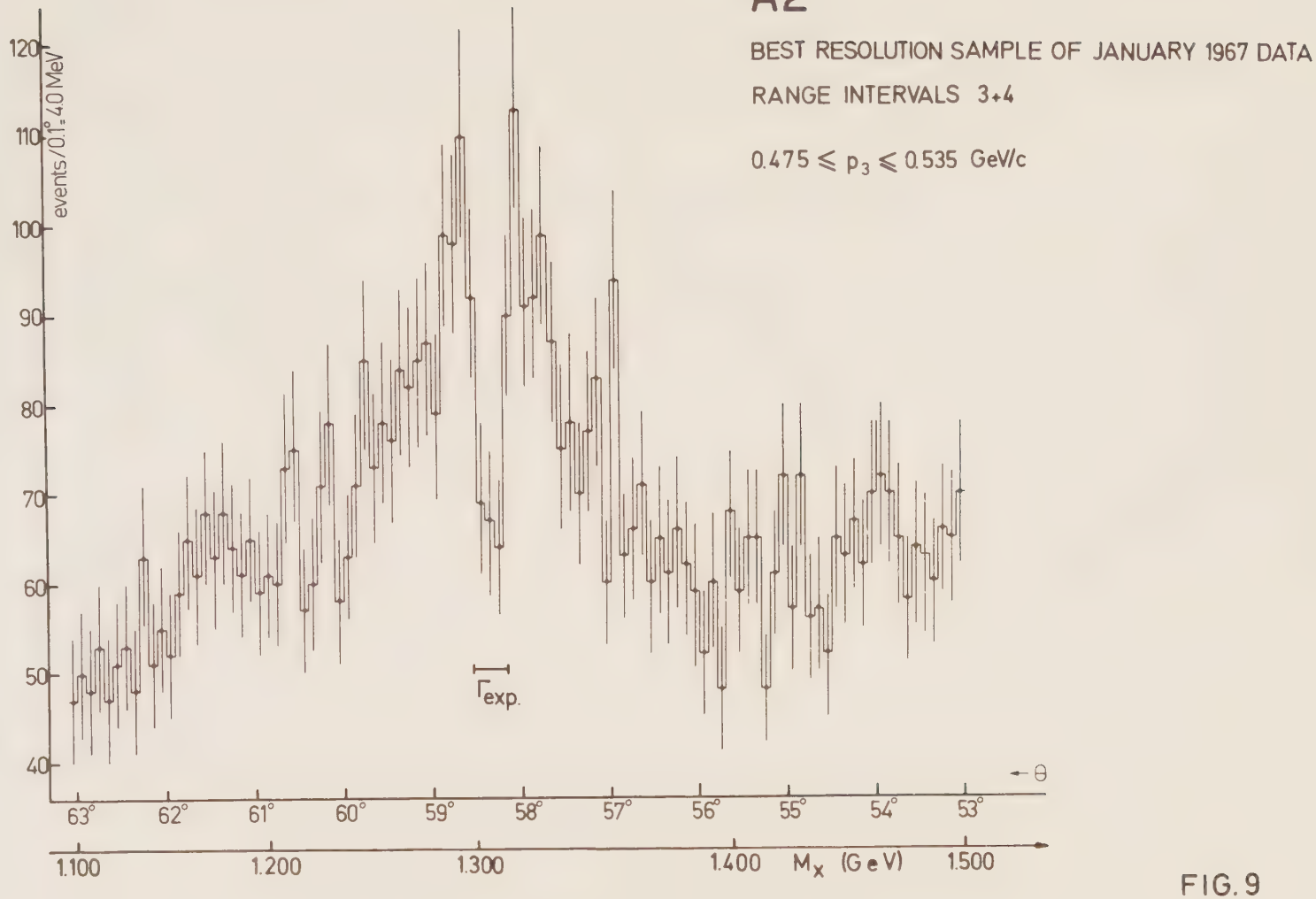
A2
BEST RESOLUTION SAMPLE OF JANUARY 1967 DATA
RANGE INTERVALS 3÷4
0.475 ⩽ p3 ⩽ 0.535 GeV/c
events/0.1°±40 MeV
120
110
100
90
80
70
60
50
40
Γexp.
←θ
63°
62°
61°
60°
59°
58°
57°
56°
55°
54°
53°
1.100
1.200
1.300
1.400
Mx (GeV)
1.500

FIG. 9

Fig. 10 : Earlier data on the A_2 mass spectrum:

a) A_2 at p_1 = 6.0 GeV/c (May 1965), with the spectrometer operating with "tapered absorbers". Centre angle of proton telescope $\Theta = 55°$. $0.485 < p_3 < 0.660$ GeV/c measured by time-of-flight.

b) A_2 at p_1 = 7.0 GeV/c (October 1965), spectrometer in "flat absorber" mode of operation, and using a completely redesigned proton telescope, centre angle $\Theta = 52°$. $0.480 < p_3 < 0.550$ GeV/c, lower limit measured by range, upper limit by time-of-flight.

c) Sum of (a) and (b), shows appearance of A_2 in the total earlier data. These data have been published in larger bins.

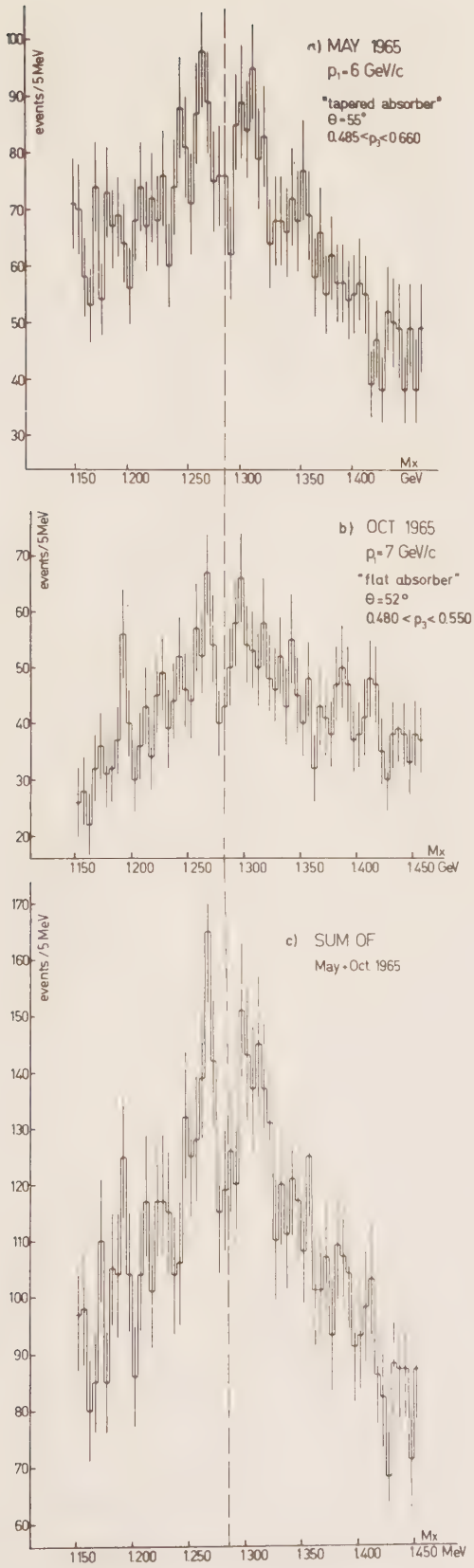
a) MAY 1965
p_1 = 6 GeV/c
"tapered absorber"
Θ = 55°
0.485 < p_3 < 0.660
events / 5 MeV
Mx
GeV
b) OCT 1965
p_1 = 7 GeV/c
"flat absorber"
Θ = 52°
0.480 < p_3 < 0.550
events / 5 MeV
Mx
GeV
c) SUM OF
May + Oct 1965
events / 5 MeV
Mx
MeV

FIG. 10

Fig. 11 : Total A_2 (May 1965 + October 1965 + January 1967). The following fits were obtained:

i) a single Breit-Wigner curve (dash-point line);

ii) two incoherent Breit-Wigner curves (dashed line);

iii) a "dipole" (full line).

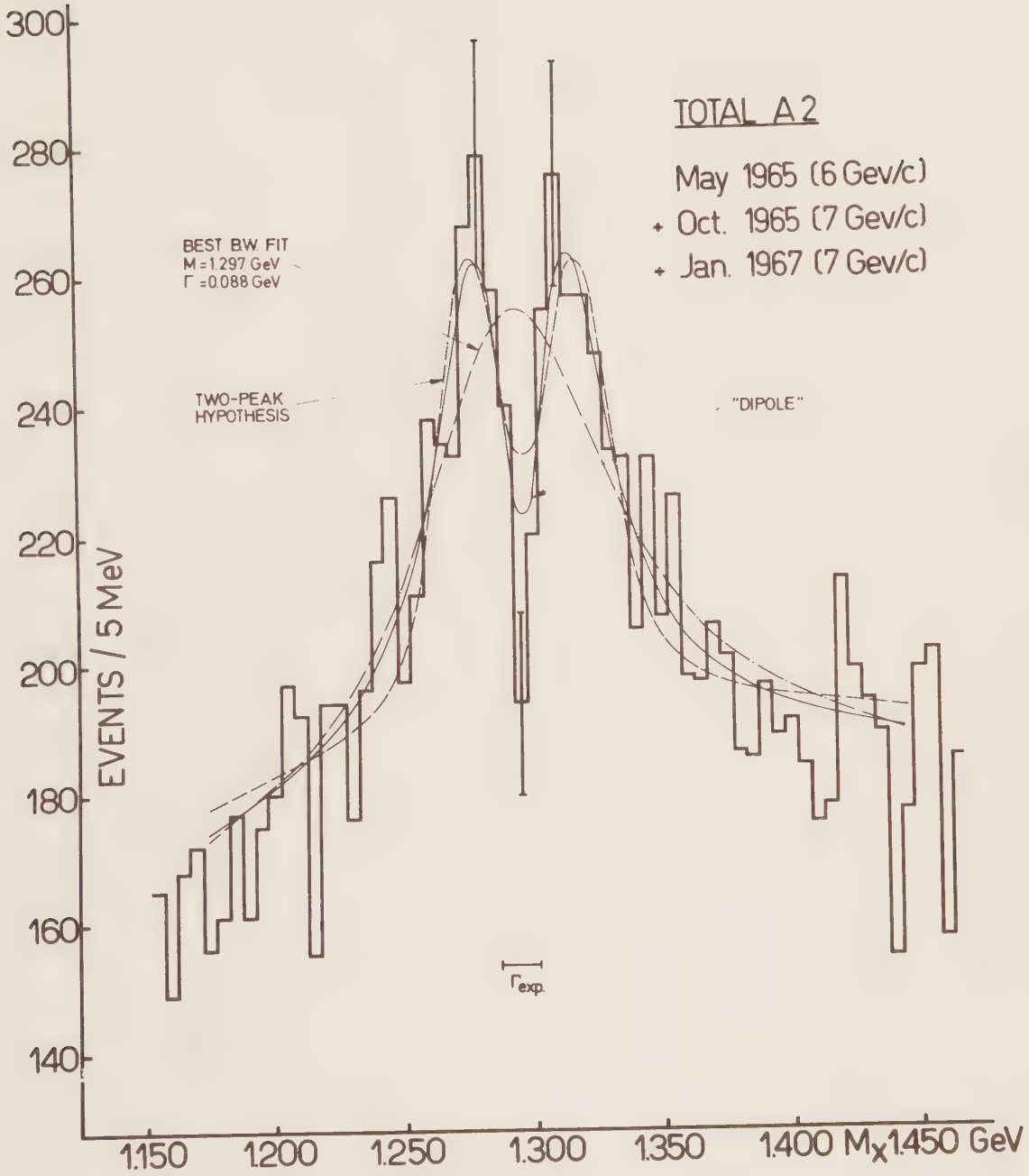
TOTAL A2
May 1965 (6 Gev/c)
+ Oct. 1965 (7 Gev/c)
+ Jan. 1967 (7 Gev/c)
BEST B.W. FIT
M = 1.297 GeV
Γ = 0.088 GeV
TWO-PEAK HYPOTHESIS
"DIPOLE"
EVENTS / 5 MeV
300
280
260
240
220
200
180
160
140
1.150
1.200
1.250
1.300
1.350
1.400
M_X 1.450 GeV
Γ_exp.

FIG. 11

Fig. 12 : Total data in the R region. As the end of full geometrical efficiency for the 7 GeV/c data is at 1860 MeV, we plot the spectrum only up to this mass. Bin size = 10 MeV.

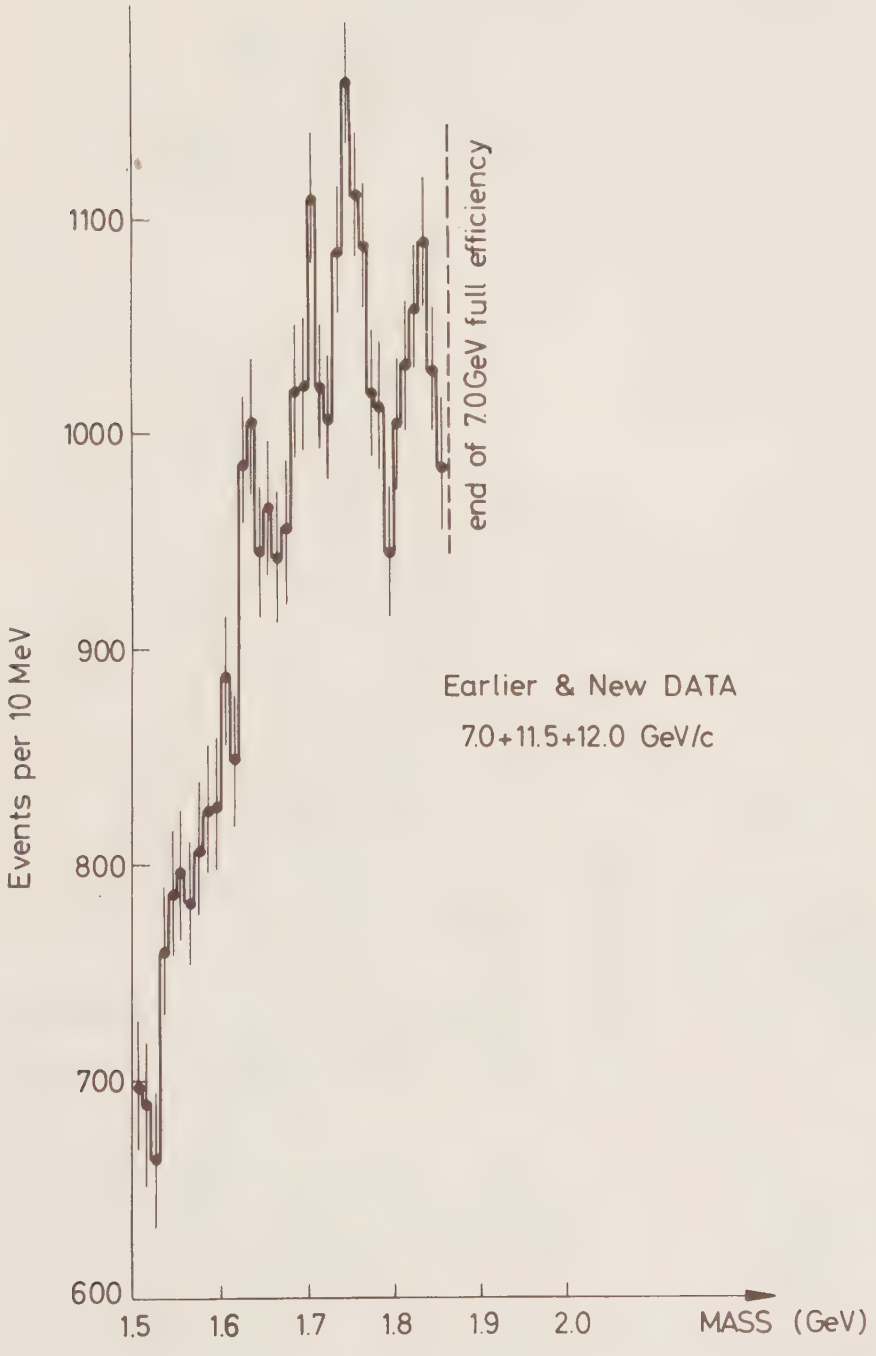
Events per 10 MeV
1100
1000
900
800
700
600
1.5
1.6
1.7
1.8
1.9
2.0
MASS (GeV)
end of 7.0GeV full efficiency
Earlier & New DATA
7.0+11.5+12.0 GeV/c

FIG.12

Fig. 13 : (A) and (B). Earlier data at 7 and 12 GeV/c with no charge selection for the decay products. The momentum transfer bite is $0.20 < t < 0.27$ $(GeV/c)^2$. Although this t-range is outside the Jacobian peak for the S(1930) meson, the enhancement at nearly the correct mass of the S can be seen.

(C). New data produced with 11.5 GeV/c incident π^- with a momentum transfer bite $0.18 < t < 0.29$ $(GeV/c)^2$. The charge selection is 1 + 3

Fig. 13 : (cont'd.) charged particles in the vertex matrix. R_1, R_2, R_3, and S are clearly seen. For the S meson, as in the 12 GeV/c data, the t-range is partially outside the Jacobian peak.

(D). New data at 11.5 GeV/c with the selection 1 charged particle in the vertex matrix. Contrary to the absence of R_3 in this decay selection, in our earlier data the $R_3(1750)$ is clearly seen, probably because of introduction of a new vertex matrix with better resolution.

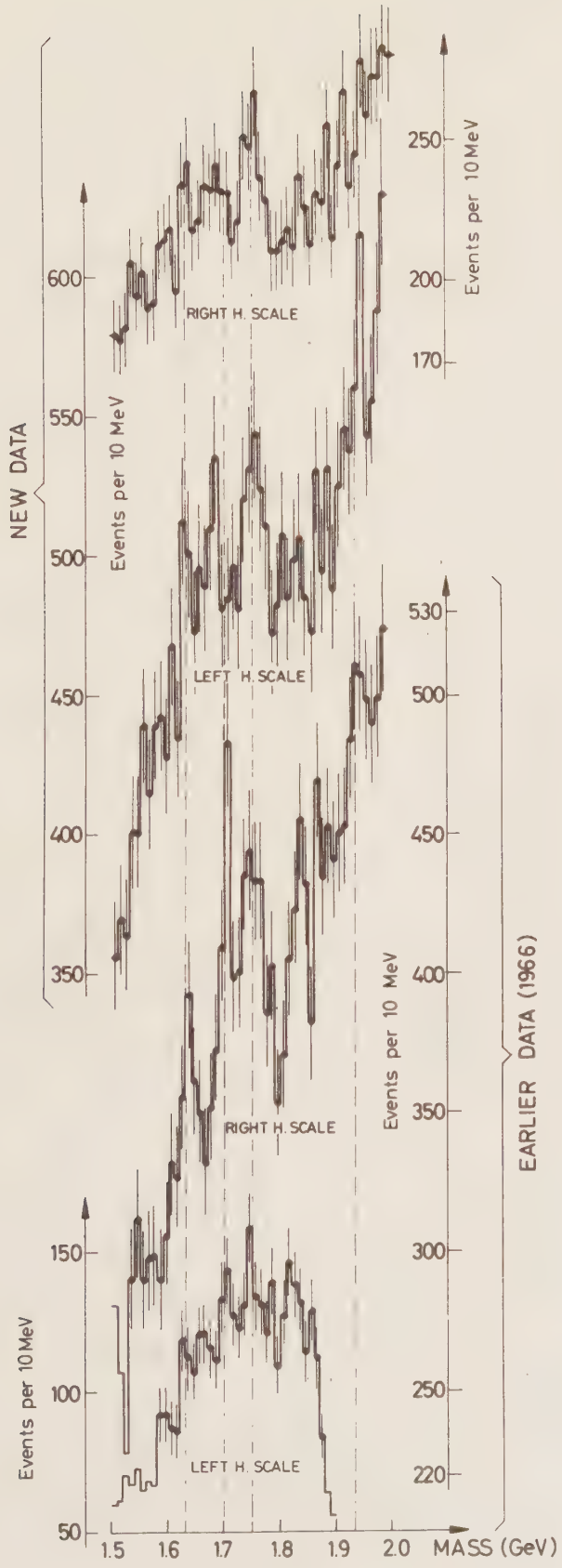

D

11.5 GeV/c

$0.18 < t < 0.29$ $(GeV/c)^2$

1 charged

C

11.5 GeV/c

$0.18 < t < 0.29$ $(GeV/c)^2$

(1+3) charged

B

12.0 GeV/c

$0.20 < t < 0.27$ $(GeV/c)^2$

all Decay Modes

A

7.0 GeV/c

$0.20 < t < 0.27$ $(GeV/c)^2$

all Decay Modes

FIG.13

Fig. 14 : Combined data 7, 11.5, and 12 GeV/c, with background subtracted. Upper part of the figure shows the expected spin-orbit splitting for the D-wave of a quark-antiquark pair taking the R_1 and R_3 masses as the reference values. G-parities inferred from bubble chamber experiments suggest G = +1 for R_1, R_2, and R_4; this is strongly supported, particularly for R_1, at which mass a charged dipion peak in effective mass distribution has been reported. The R_2 and R_4 could be identical with the $\pi\pi$ peaks observed at the same masses; nevertheless, these $\pi\pi$ enhancements have only been observed in a neutral system and no definite statement on isospin can be made. No positive G-parity objects have been found at the R_3 mass, but there was a broad bump found in the 3π neutral system; assuming it is an I = 1 object, G = -1. The background level was determined by the shoulders below and above the broad R peak, when it was plotted in 40 MeV bins.

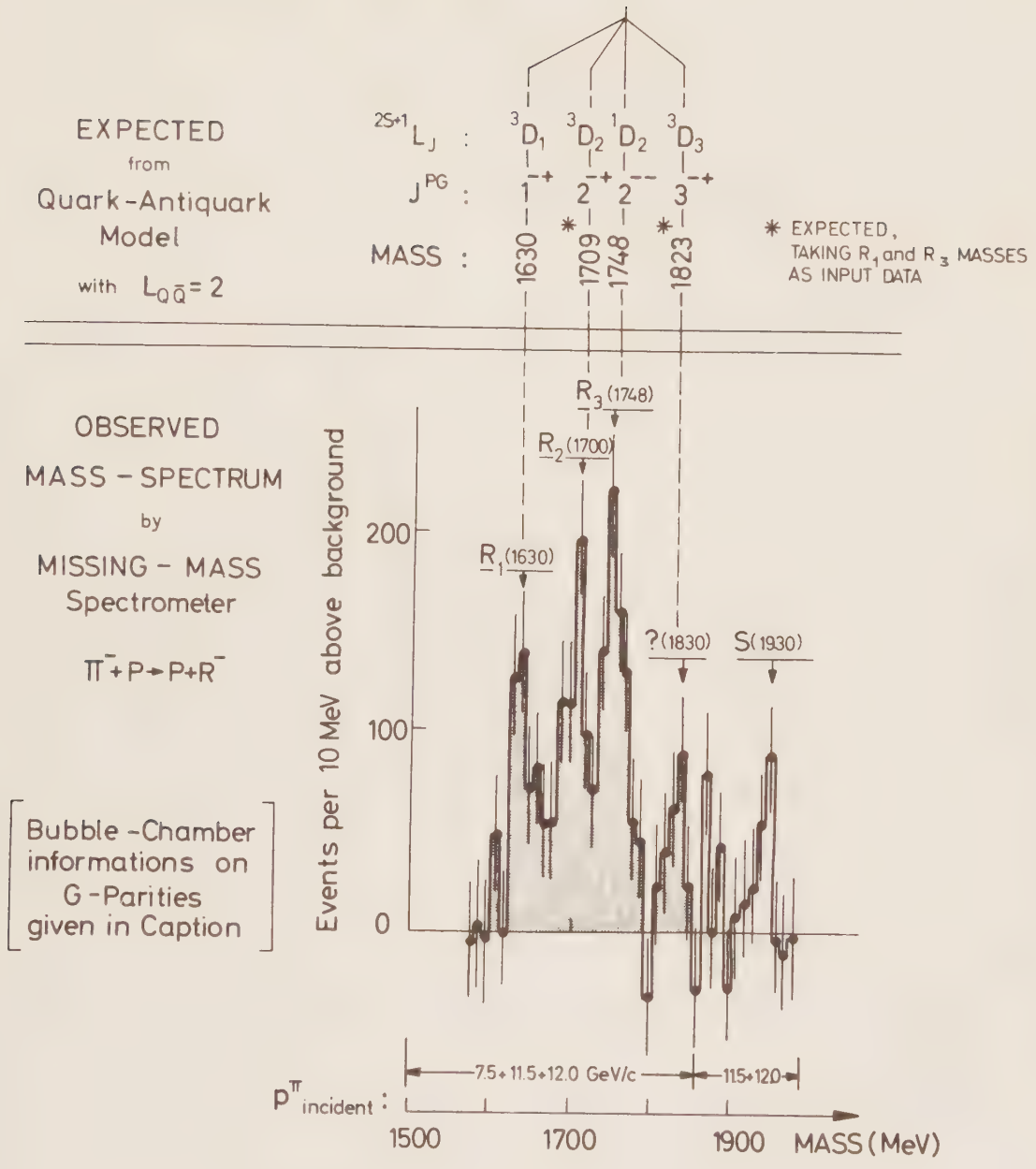
EXPECTED
from
Quark-Antiquark
Model
with $L_{Q\bar{Q}} = 2$
$^{2S+1}L_J$: $^3D_1$ $^3D_2$ $^1D_2$ $^3D_3$
J^{PG} : 1^{-+} 2^{-+} 2^{--} 3^{-+}
MASS : 1630 1709 1748 1823
* EXPECTED, TAKING R_1 and R_3 MASSES AS INPUT DATA
OBSERVED
MASS - SPECTRUM
by
MISSING - MASS
Spectrometer
$\pi^- + P \to P + R^-$
Bubble-Chamber informations on G-Parities given in Caption
R_3(1748)
R_2(1700)
R_1(1630)
?(1830)
S(1930)
Events per 10 MeV above background
200
100
0
7.5+11.5+12.0 GeV/c
11.5+12.0
$p^{\pi}_{incident}$:
1500
1700
1900
MASS (MeV)

FIG.14

Fig. 15a: Evidence for the S boson in the missing-mass spectrum from 1750 to 2150 MeV. Angular distribution of the recoil proton in a narrow band of $0.50 < p_3 < 0.63$ is shown directly. The decay selection 3 charged plus possible neutrals is shown. The same data in triple bins are shown at the side of the distribution.

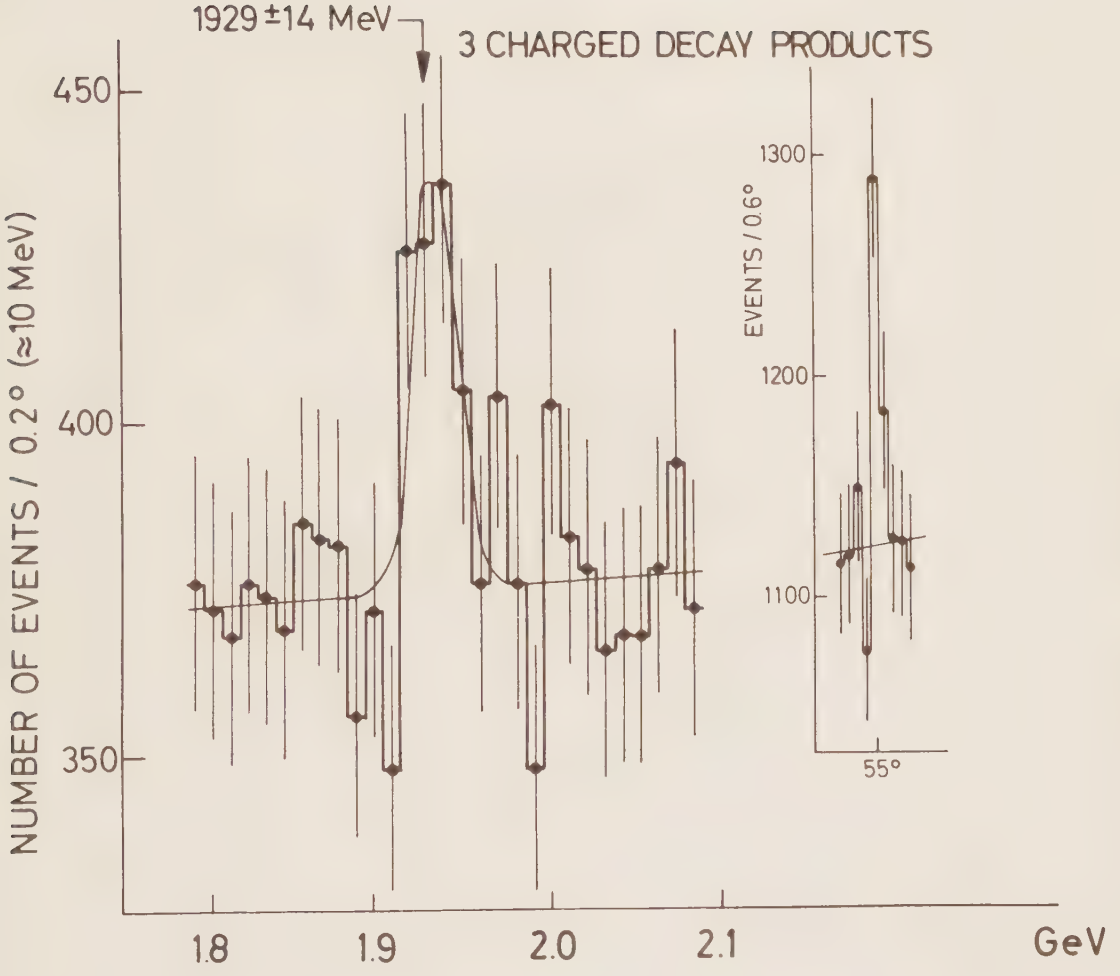
1929 ±14 MeV
3 CHARGED DECAY PRODUCTS
450
400
350
NUMBER OF EVENTS / 0.2° (≈10 MeV)
1300
1200
1100
EVENTS / 0.6°
55°
1.8
1.9
2.0
2.1
GeV

FIG.15a

Fig. 15b: Evidence for the T boson in missing-mass spectrum from 2050 to 2350 MeV. The missing-mass distribution is shown in bins of 10 MeV.

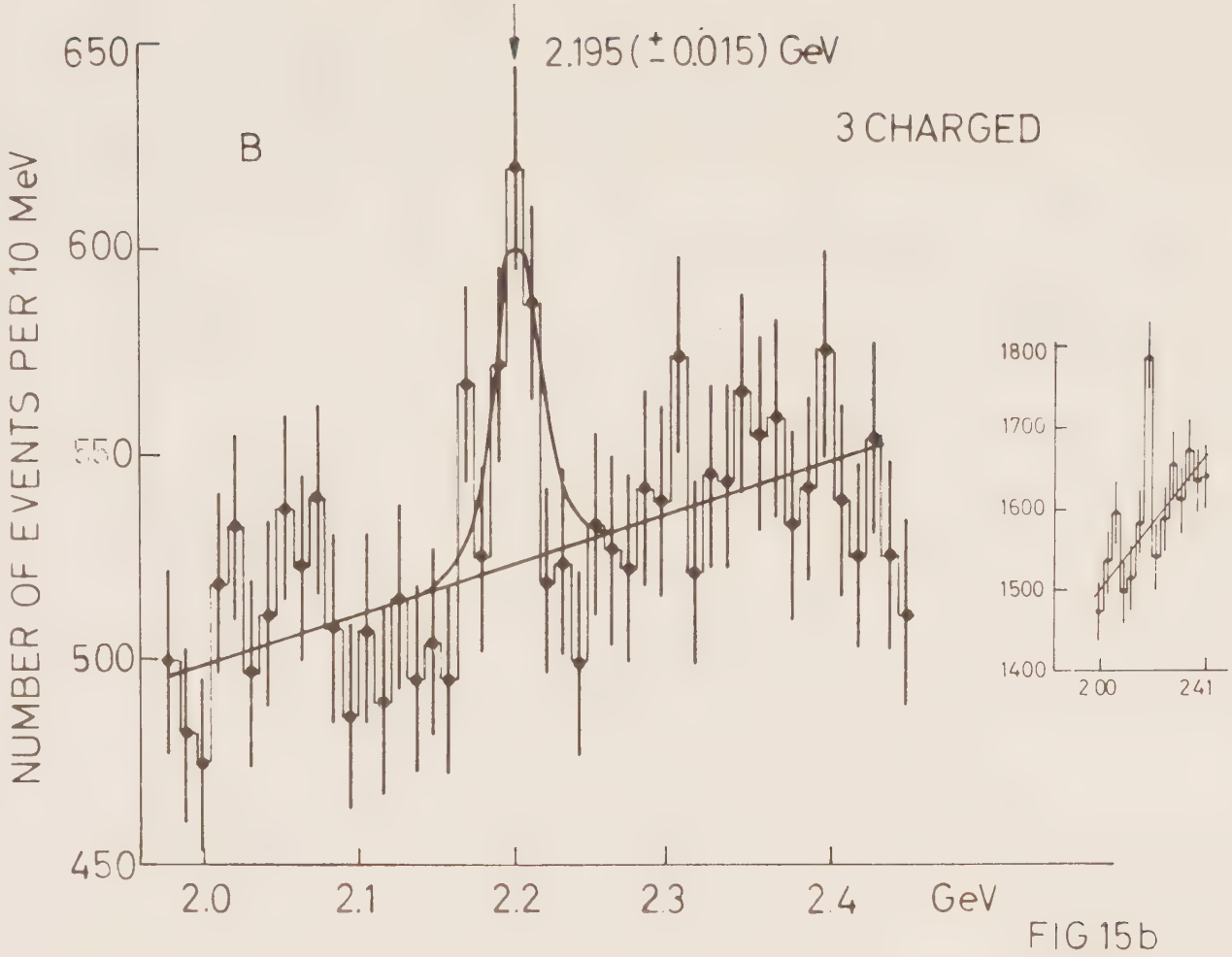
2.195 (± 0.015) GeV
B
3 CHARGED
NUMBER OF EVENTS PER 10 MeV
650
600
550
500
450
2.0
2.1
2.2
2.3
2.4
GeV
1800
1700
1600
1500
1400
2 00
241

FIG 15b

Fig. 16 : Evidence for the U boson in the missing-mass spectrum from 2000 to 2450 MeV, which is the maximum mass observable in our last run. All decay modes were put together

a) first evidence in angular distribution, obtained in November;

b) combined sample from all runs in missing mass (30 MeV bins).

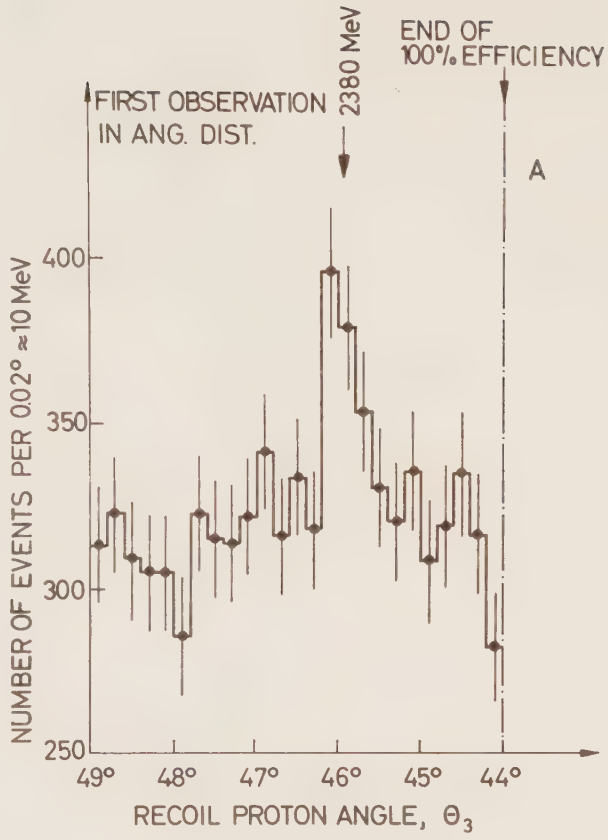
FIRST OBSERVATION
IN ANG. DIST.
2380 MeV
END OF
100% EFFICIENCY
A
NUMBER OF EVENTS PER 0.02° ≈10 MeV
400
350
300
250
49°
48°
47°
46°
45°
44°
RECOIL PROTON ANGLE, Θ_3

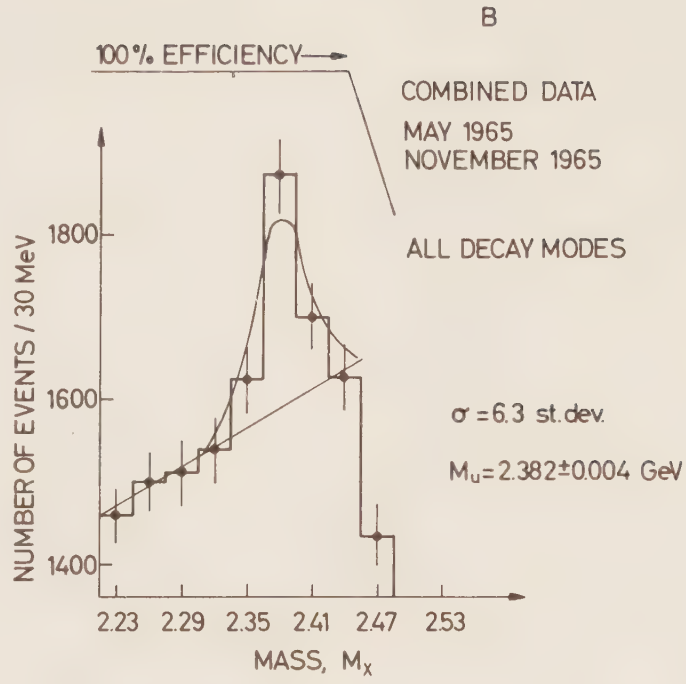
B
100% EFFICIENCY
COMBINED DATA
MAY 1965
NOVEMBER 1965
ALL DECAY MODES
σ = 6.3 st.dev.
M_u = 2.382±0.004 GeV
NUMBER OF EVENTS / 30 MeV
1800
1600
1400
2.23
2.29
2.35
2.41
2.47
2.53
MASS, M_X

FIG.16

Fig. 17 : Example of cumulative evidence is given for the case of the T boson, which is seen in three runs made under different experimental conditions and at different times.

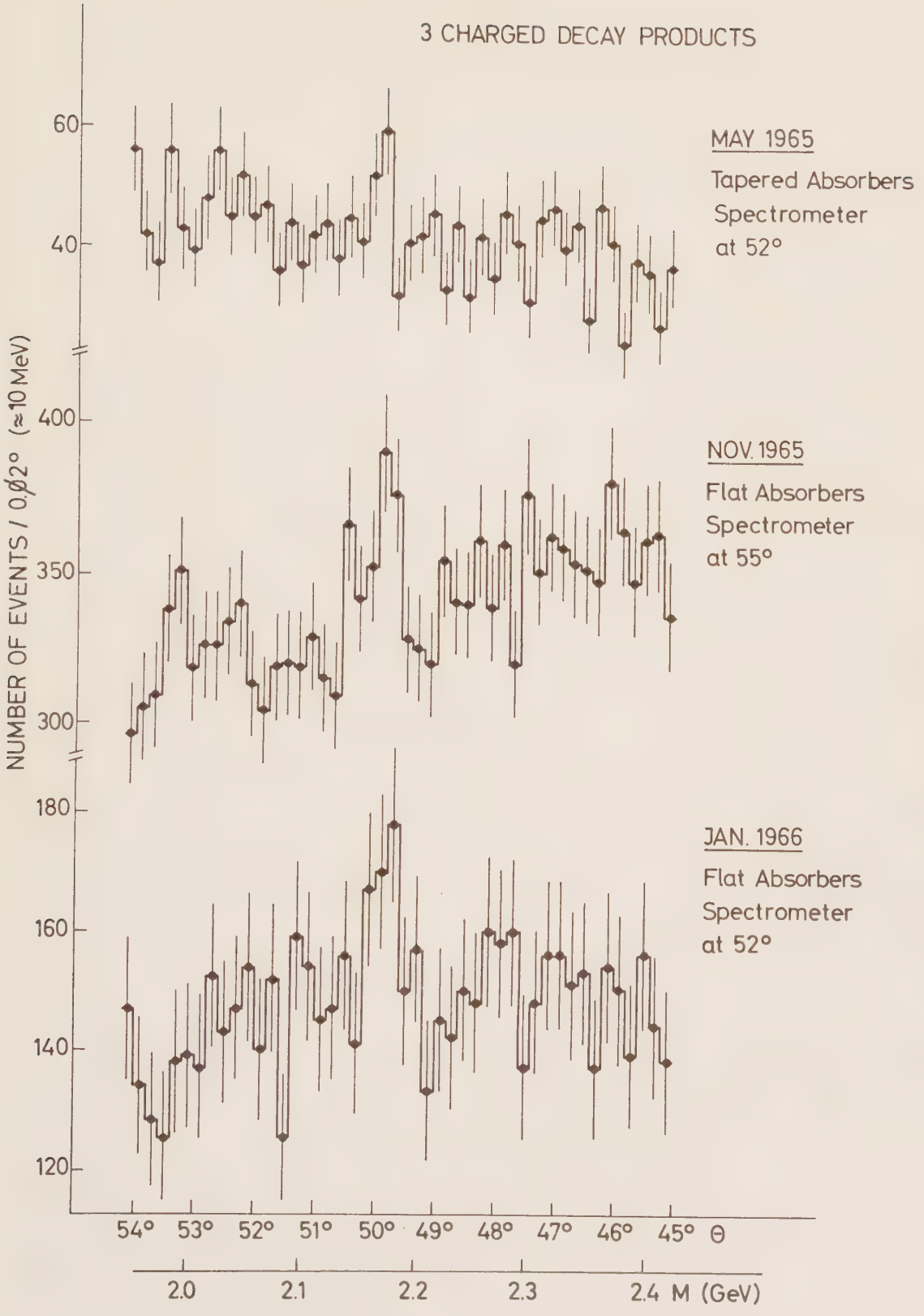
3 CHARGED DECAY PRODUCTS
MAY 1965
Tapered Absorbers
Spectrometer
at 52°
NOV. 1965
Flat Absorbers
Spectrometer
at 55°
JAN. 1966
Flat Absorbers
Spectrometer
at 52°
NUMBER OF EVENTS / 0.02° (≈10 MeV)
60
40
400
350
300
180
160
140
120
54° 53° 52° 51° 50° 49° 48° 47° 46° 45° Θ
2.0 2.1 2.2 2.3 2.4 M (GeV)

FIG.17

Fig. 18 : Current-voltage diagram between parallel plane electrodes in a gas. With increasing voltage, the current at first increases to a nearly constant value which corresponds to the photocurrent produced at the cathode (region a). At higher voltage, the current increases rapidly (region b-c). This amplification was ascribed by Townsend to ionization by electron collision. Photoelectrons leaving the cathode gain sufficient energy in the applied field to cause ionization when colliding with gas molecules.

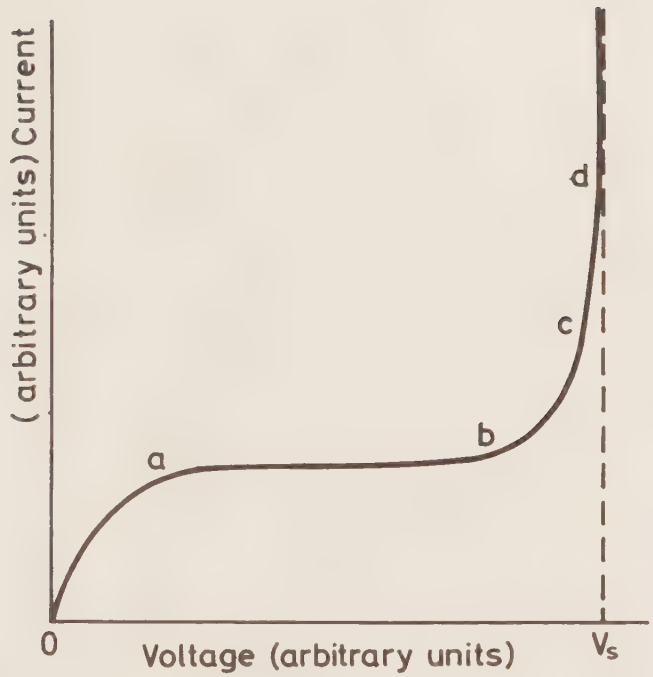

FIG.18

Fig. 19 : Ionization density for different gas mixtures. The curves obtained by Kruithof and Penning for neon and neon-argon mixtures show the variation of the first Townsend coefficient α with increasing electric field E. p_o is the gas pressure in mm Hg corrected to 0° C.

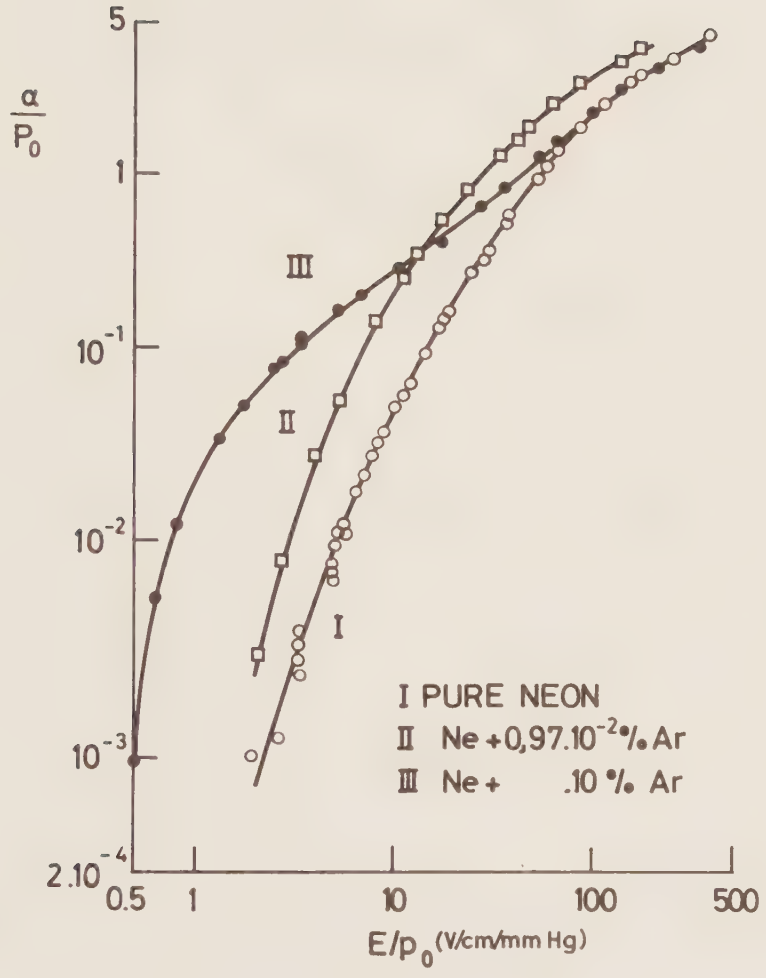
5
1
10^{-1}
10^{-2}
10^{-3}
2.10^{-4}
$\frac{\alpha}{P_0}$
III
II
I
I PURE NEON
II Ne +0,97.10^{-2}% Ar
III Ne + .10 % Ar
0.5
1
10
100
500
E/p_0 (V/cm/mm Hg)

FIG.19

Fig. 20 : The mechanism for avalanche development (a, b, c) and the subsequent growth into a streamer (d) and a spark (e).

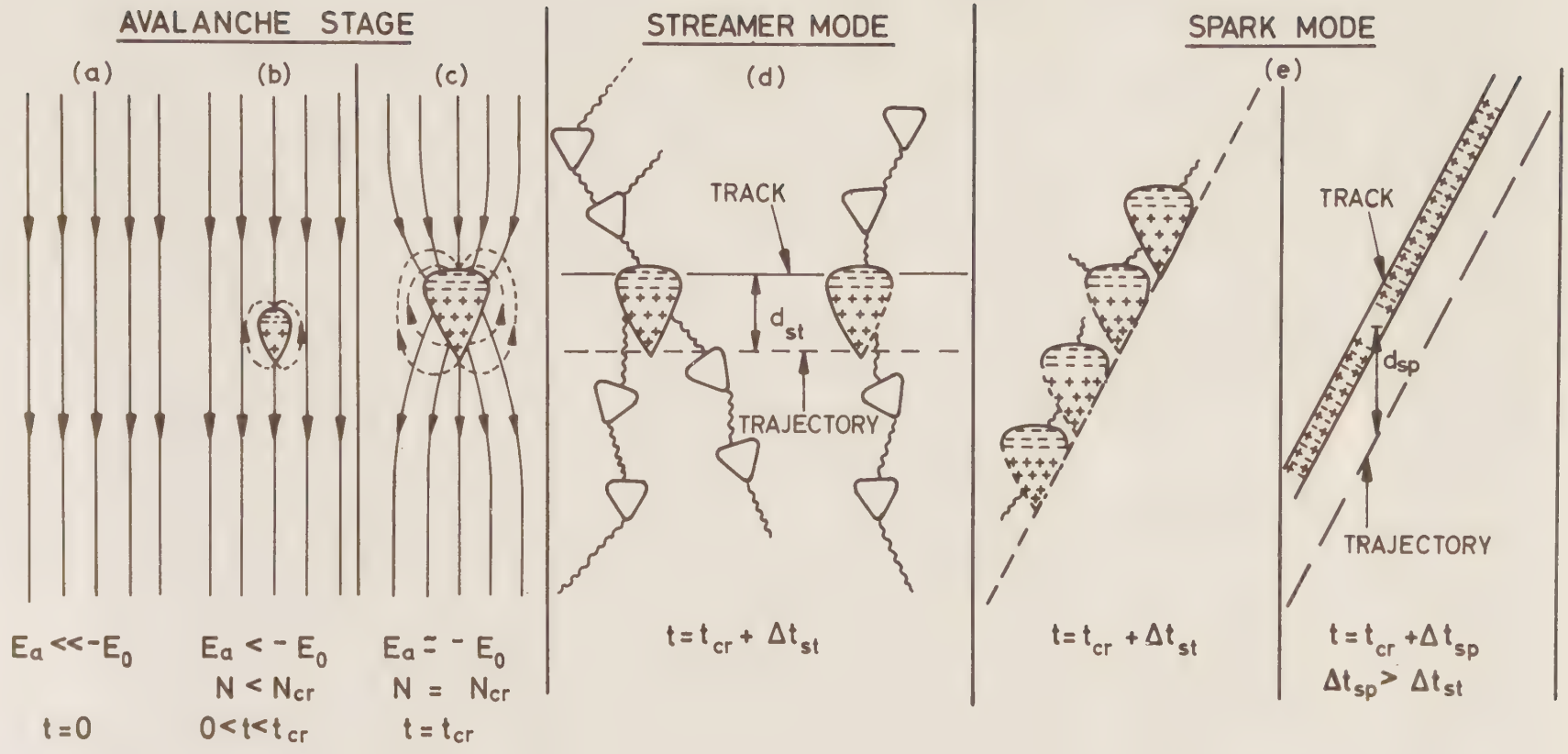
AVALANCHE STAGE
(a)
(b)
(c)
$E_a << -E_0$
$t = 0$
$E_a < -E_0$
$N < N_{cr}$
$0 < t < t_{cr}$
$E_a \simeq -E_0$
$N = N_{cr}$
$t = t_{cr}$
STREAMER MODE
(d)
TRACK
d_{st}
TRAJECTORY
$t = t_{cr} + \Delta t_{st}$
SPARK MODE
(e)
$t = t_{cr} + \Delta t_{st}$
TRACK
d_{sp}
TRAJECTORY
$t = t_{cr} + \Delta t_{sp}$
$\Delta t_{sp} > \Delta t_{st}$

FIG. 20

Fig. 21 : Different stages of a streamer.

The particle trajectory (verticle) is perpendicular to the applied electric field (horizontal). Four different stages of streamer formation corresponding to HV pulses of different length are seen. The picture on the left shows the useful mode of operation: the track consists of a string of luminous dots. The second picture from the left shows positive and negative streamers already clearly separated. A still longer HV pulse was applied, giving pictures three and four; discharge through many channels. The pictures were taken by G.E. Chikovani.

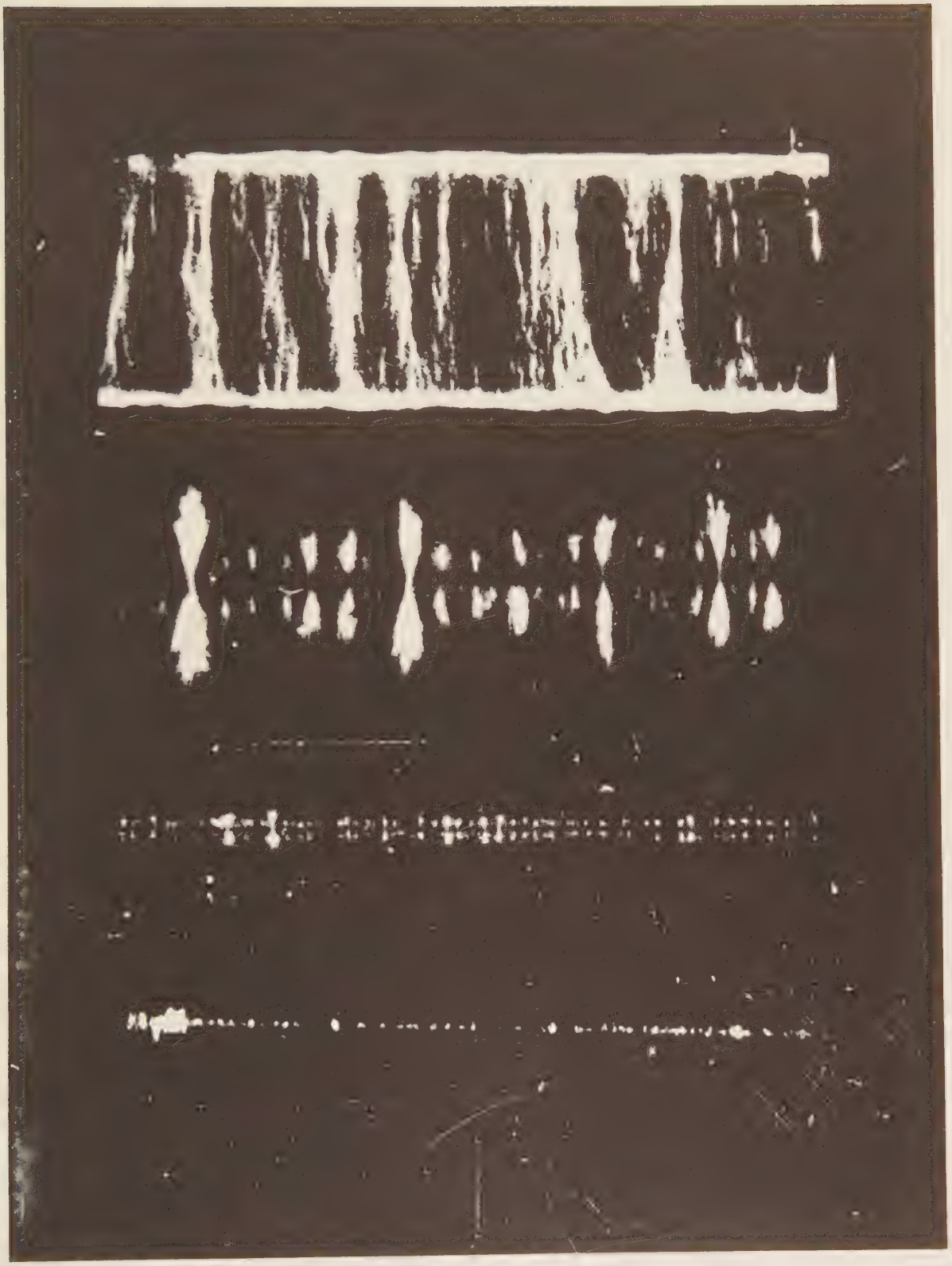

FIG. 21

Fig. 22 : Streamer chamber picture with the chamber inside a magnetic field. The picture was taken by G.E. Chikovani.

FIG. 22

Fig. 23 : Particle tracks in our prototype chamber operating in the spark-following mode (polaroid film, 3000 ASA, stop number = 1 : 10).

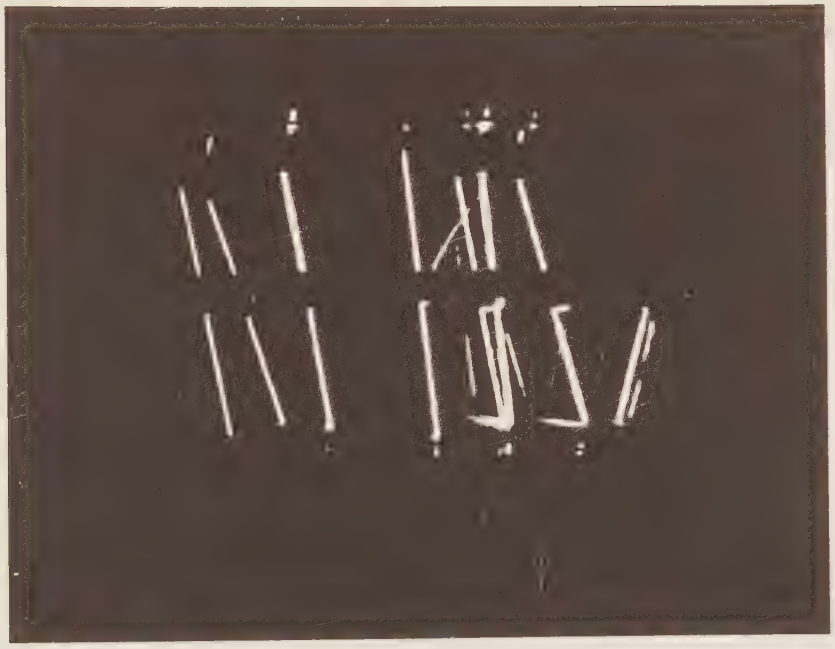

FIG. 23

Fig. 24 : Prototype chamber. Breakdown occurred along the plexiglas screws in the four corners.

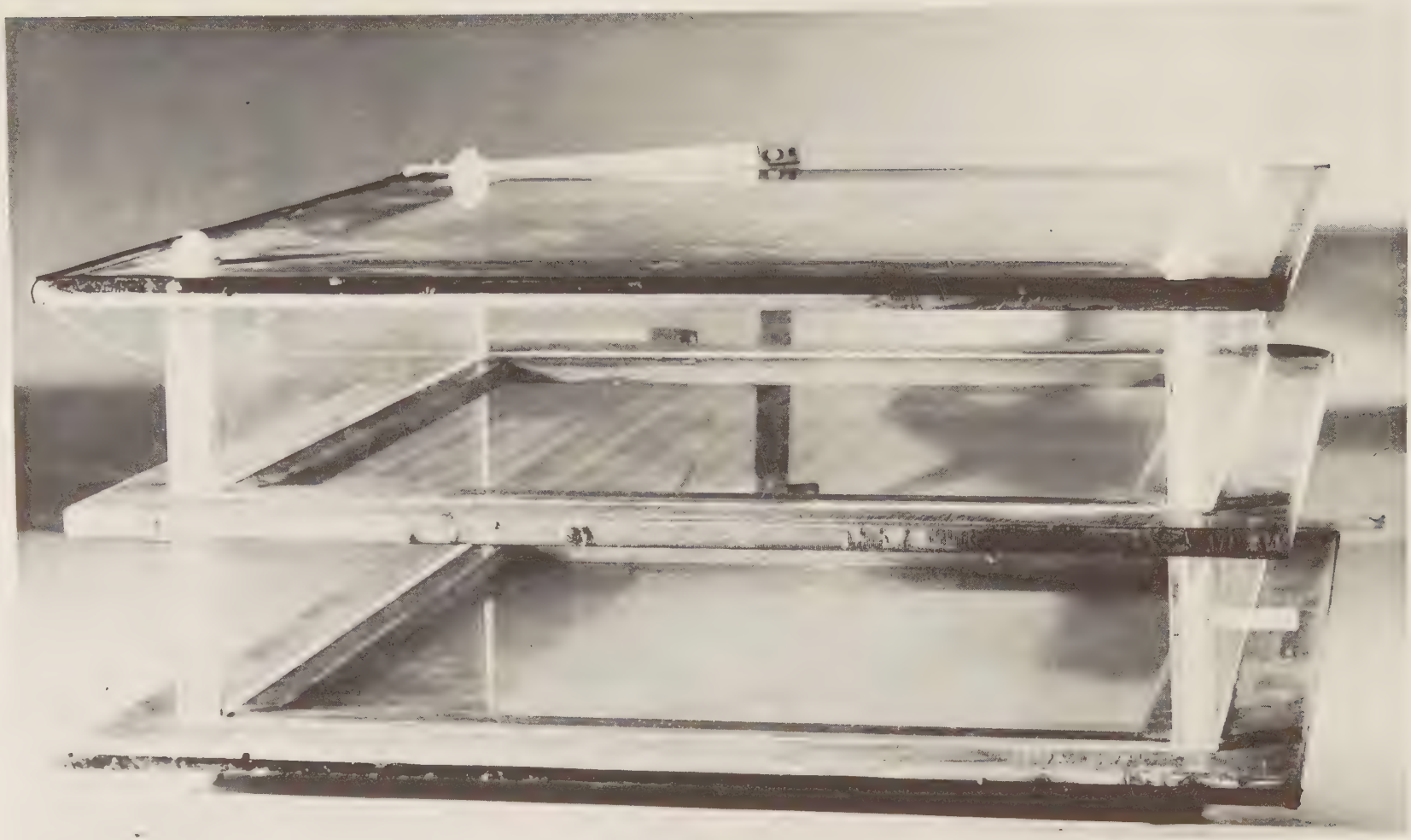

FIG. 24

Fig. 25 : View from the top into our Marx generator. Input at the left-hand side. The charging resistors are put into teflon tubes to avoid breakdown.

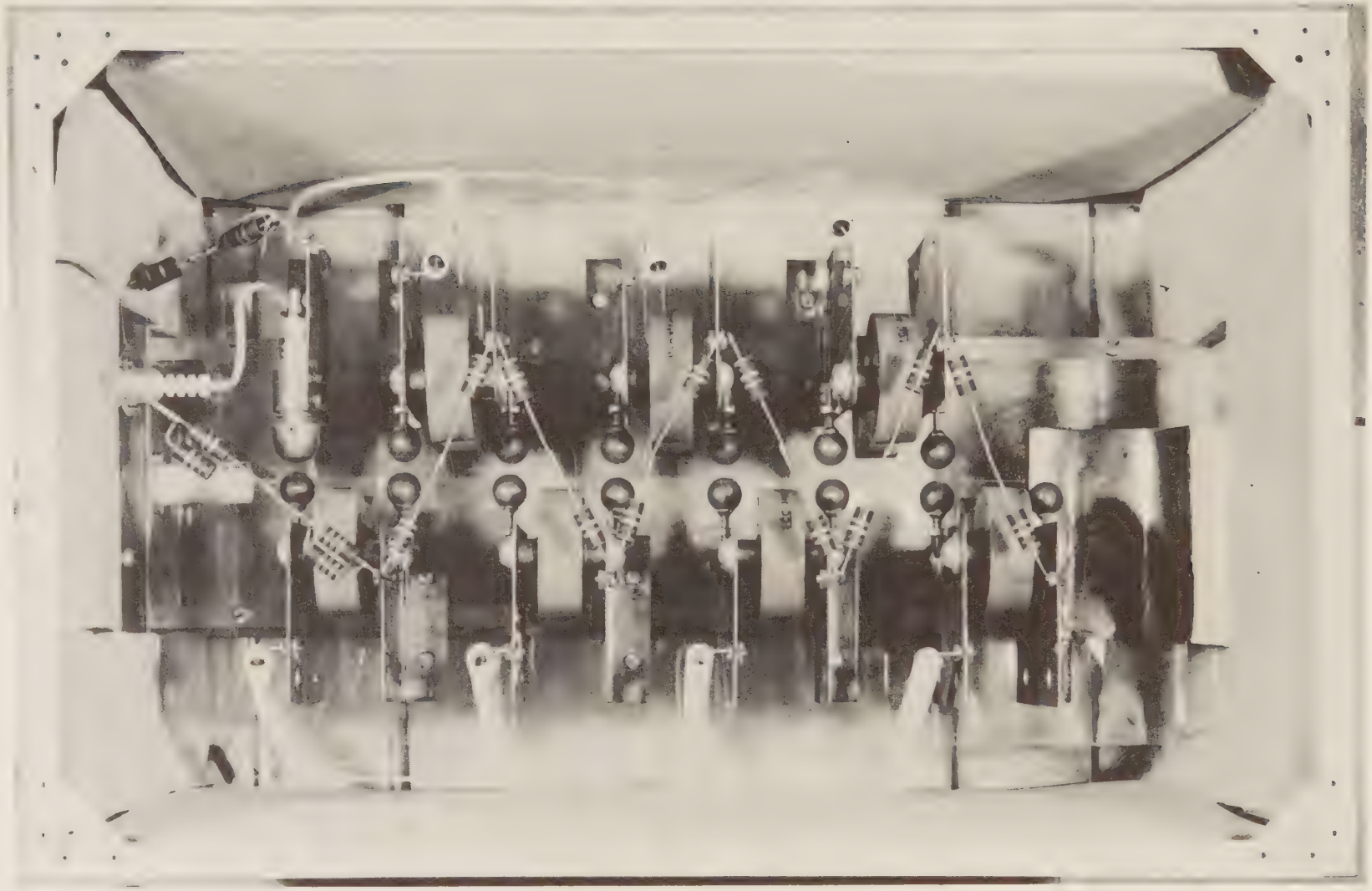

FIG. 25

Fig. 26 : Marx generator scheme.

The high voltage pulse is generated by a seven-stage Marx generator. Each stage consists of two parallel capacitors of 3×10^3 pF at 20 kV. To decrease the charging time, all stages are charged in parallel. The generator is operated in an air atmosphere. The spark-gap electrodes are steel balls, and the distance between them is adjustable. The gaps "see" each other in such a way that UV light emitted from the first gap ionizes the following ones.

The generator is triggered by a three-electrode spark gap, which itself is triggered by a 10 kV negative pulse from a conventional presparker. To decrease the jitter of the trigger gap, the ground electrode is at earth, via a resistor of 20 Ω. For recharging the generator in a short time (~ 10 msec) with a conventional power supply, a buffer capacitor of 14 μF is used.

The output pulse has a rise-time of ~ 25 nsec at a load of 860 pF (chamber load). The pulse length (normally 50-100 nsec) is adjusted by connecting resistors in parallel with the chamber. The characteristics of the generator remained unchanged after 10^6 triggers.

7-STAGE MARX-GENERATOR

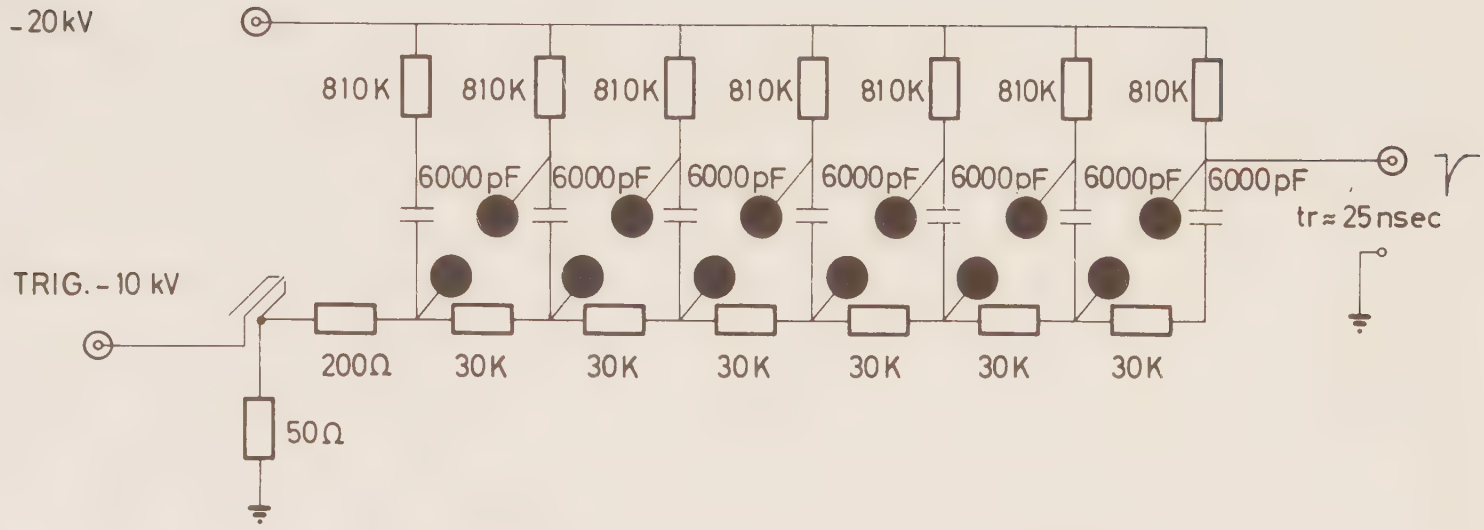

FIG.26

Fig. 27 : Efficiency versus time delay for different quencher concentrations.
Henogal : 100 (cm^3/min);
Argon : 6 (cm^3/min);
Freon : o: 0.0080, •: 0.0064, ∇: 0.0032, Δ: 0.0016 (cm^3/min).

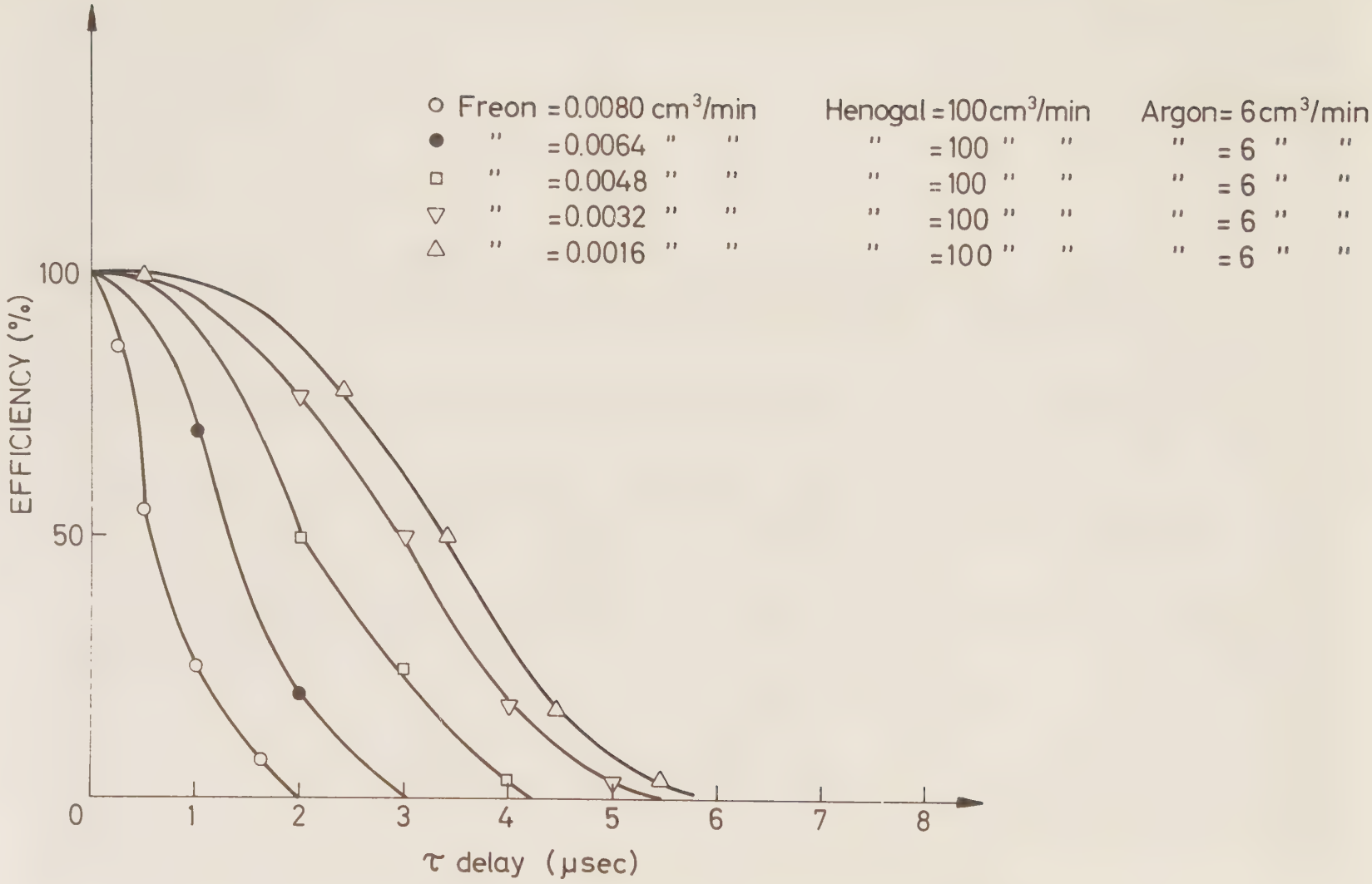
○ Freon = 0.0080 cm³/min
● " = 0.0064 " "
□ " = 0.0048 " "
▽ " = 0.0032 " "
△ " = 0.0016 " "
Henogal = 100 cm³/min
" = 100 " "
" = 100 " "
" = 100 " "
" = 100 " "
Argon = 6 cm³/min
" = 6 " "
" = 6 " "
" = 6 " "
" = 6 " "
EFFICIENCY (%)
100
50
0
1
2
3
4
5
6
7
8
τ delay (μsec)

FIG. 27

Fig. 28 : Schematic scheme of the large chamber.

FIG.28

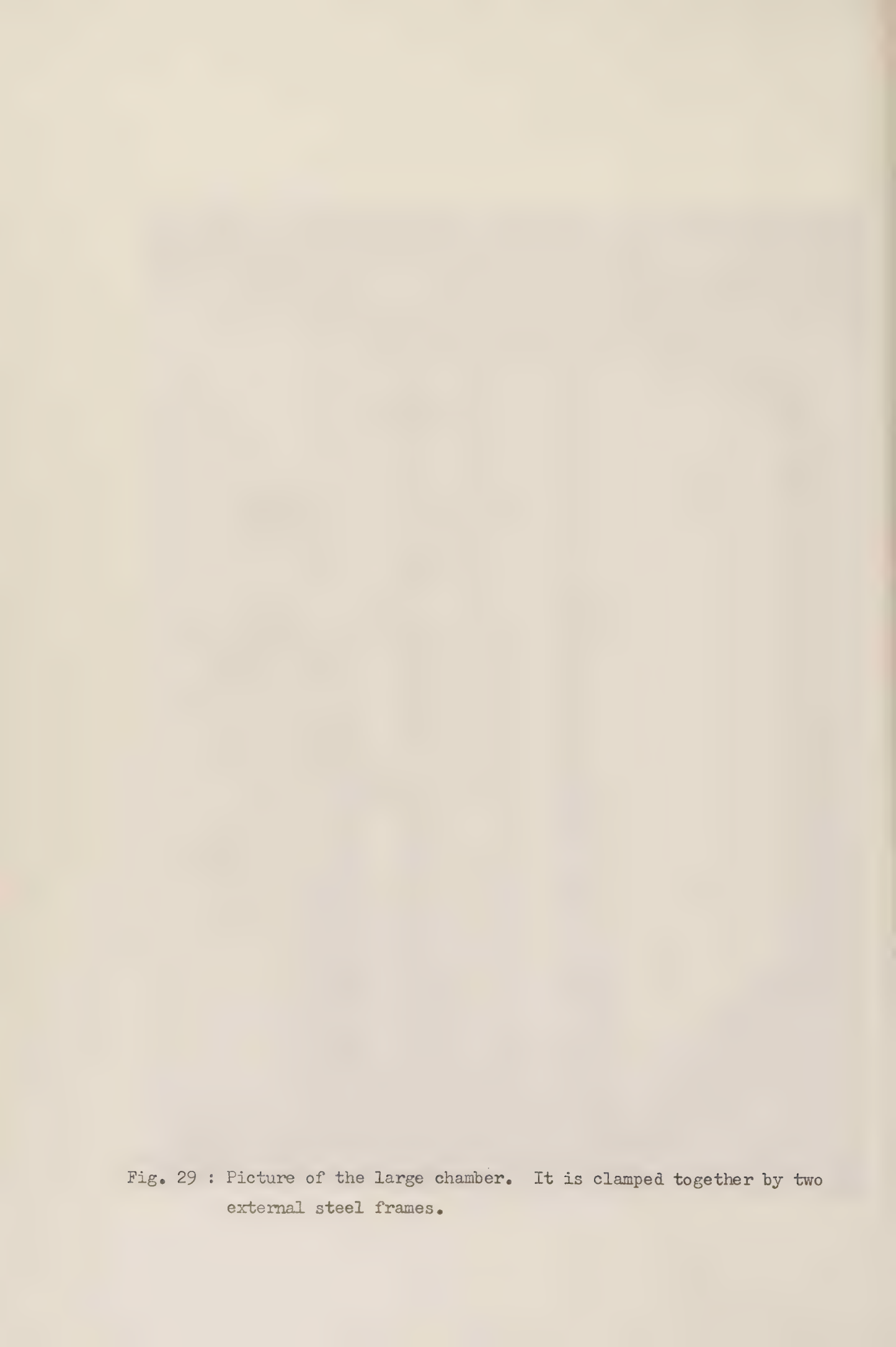

Fig. 29 : Picture of the large chamber. It is clamped together by two external steel frames.

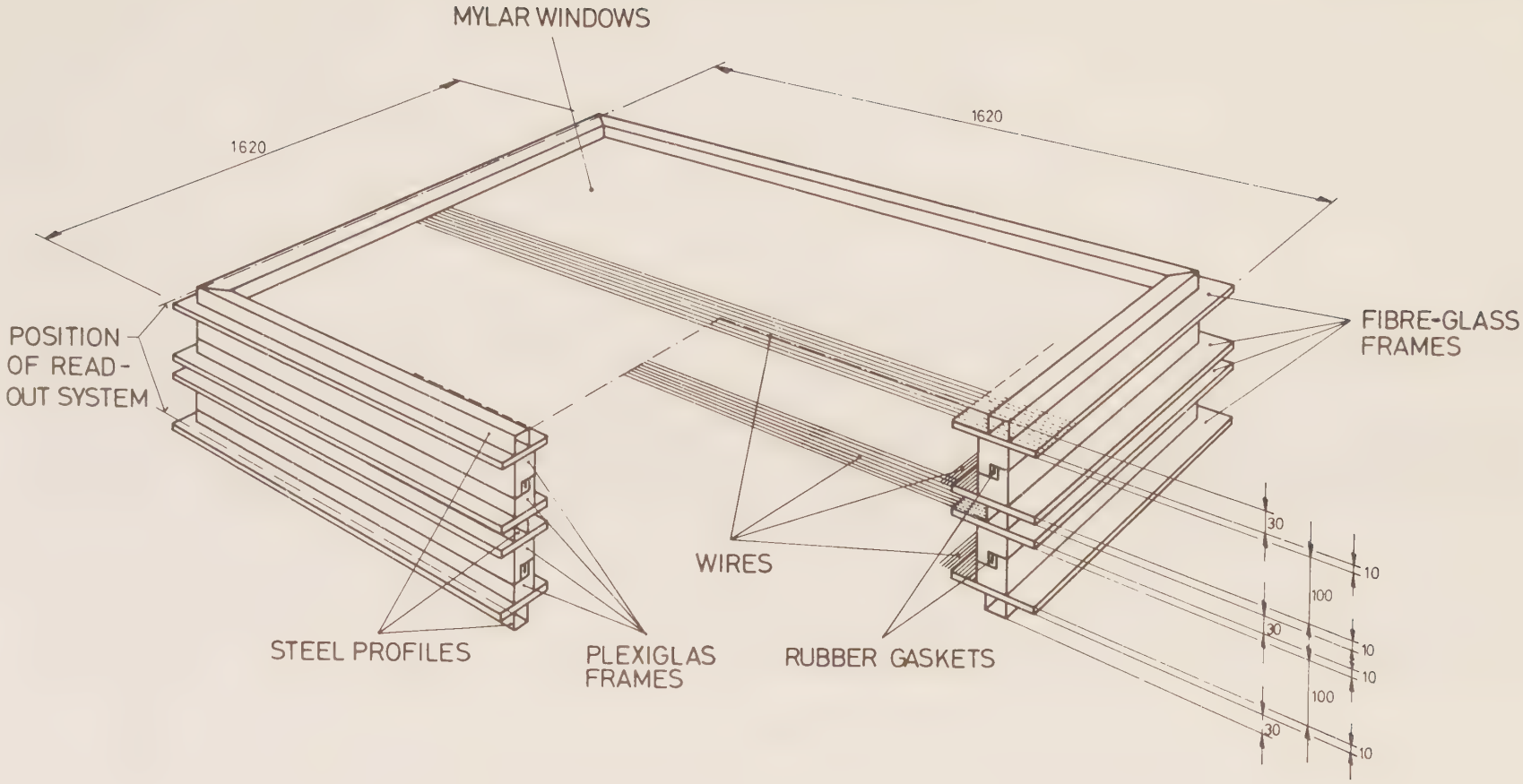
MYLAR WINDOWS
1620
1620
POSITION OF READ-OUT SYSTEM
FIBRE-GLASS FRAMES
WIRES
STEEL PROFILES
PLEXIGLAS FRAMES
RUBBER GASKETS
30
10
100
30
10
10
100
30
10

FIG. 29

Fig. 30 : Detailed view of the read-out wire and support. A 10 cm long polyethylene tube filled with silastic is damping the signals at the end of the wire to avoid reflections. The tension of the wire can be adjusted with the screw seen on the right-hand side.

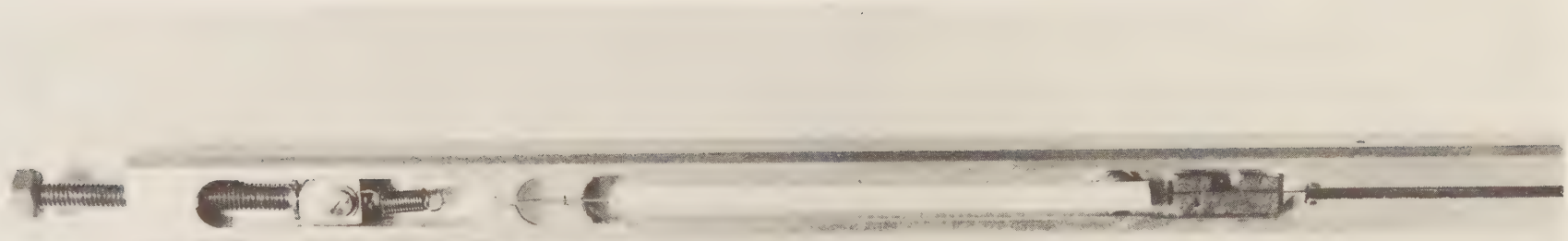

FIG. 30

Fig. 31 : Block scheme of read-out electronics from pick-up coil to computer.

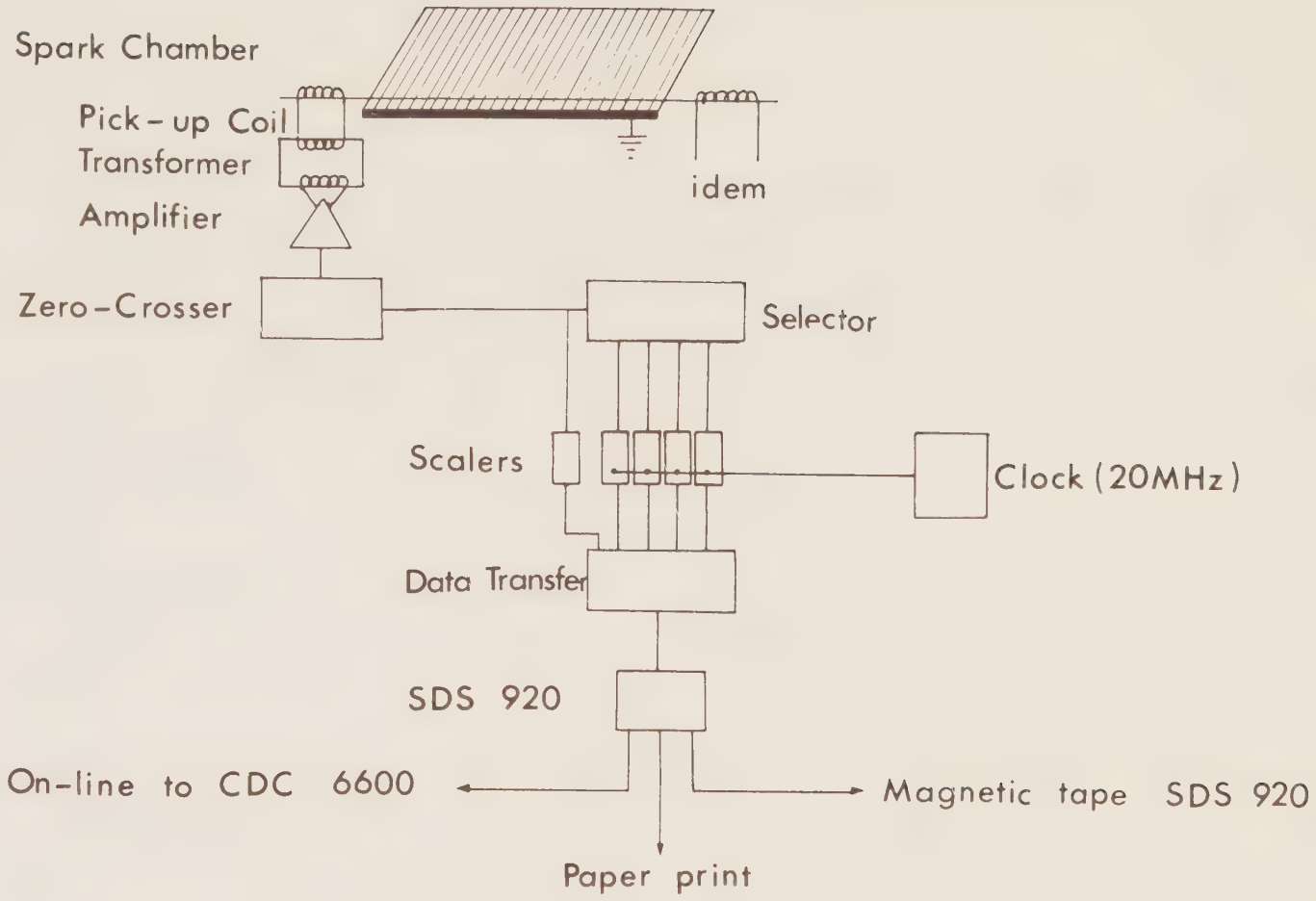
Spark Chamber
Pick-up Coil
Transformer
Amplifier
idem
Zero-Crosser
Selector
Scalers
Clock (20MHz)
Data Transfer
SDS 920
On-line to CDC 6600
Magnetic tape SDS 920
Paper print

FIG. 31

Fig. 32 : The Commander is a logic circuit with the following duties:

- to accept one trigger from fast electronics;
- to give a trigger signal to the spark chambers;
- to give "start" and "stop" signals with certain delays to the scaler (via selector);
- to give a "start record" signal to the data transfer system for transferring the scaler content into the computer memory;
- to block the fast logics until the data transfer is finished and the whole system ready for the next event.

COMMANDER FOR MAGNETOSTRICTION CHAMBER

FIG. 32

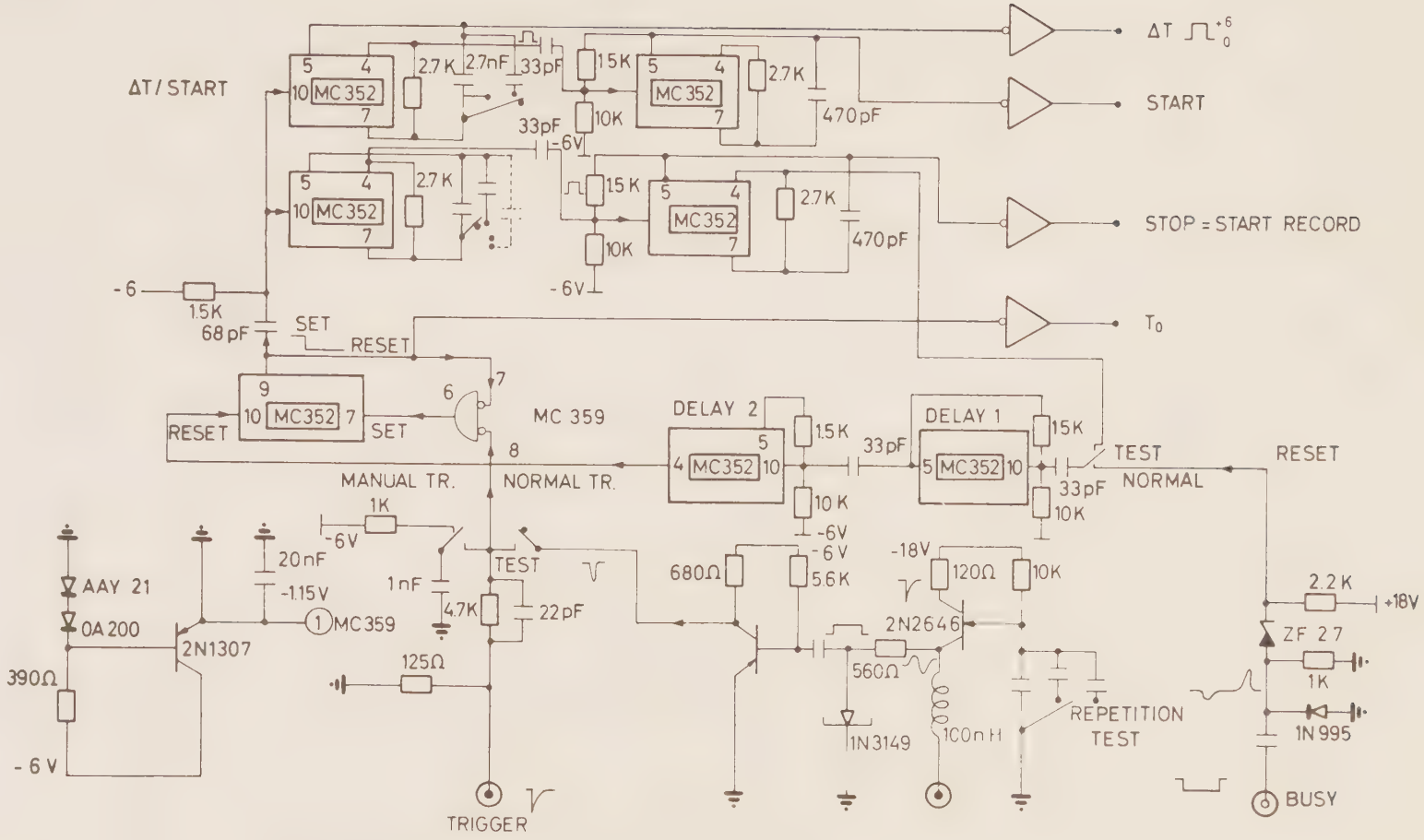

Fig. 33 : Transformer.

Since the pick-up coil has a low output impedance compared to a typical transistor input impedance, the output impedance of the read-out coil is adapted to the amplifier input impedance by a Foucault-current transformer. This transformer was designed for shielding against electromagnetic noise and to avoid losses. The transformation ratio is 1 to 8.

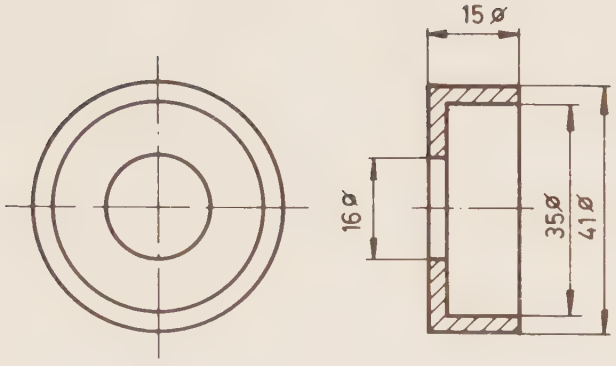

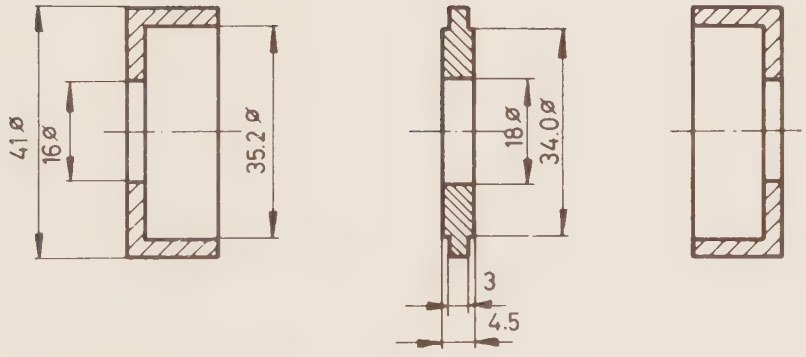

FERRITE K 300 502

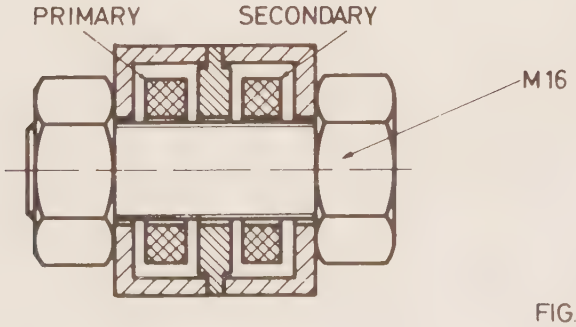

FIG. 33

Fig. 34 : Amplifier.

The amplifier following the input transformer has a gain of 450, and a threshold of 200 μV. The output is a positive signal of 9 V on 50 Ω at 20 mV input and has a non-linearity of $\pm$ 3%. The input of the amplifier is protected against overload by two high current diodes in opposite sense. To reduce integration effects due to overload from pick-up, the third stage contains a polarity-dependent feedback from collector to base via a diode. The magnetostrictive signal has such a polarity that it is not affected by this feedback.

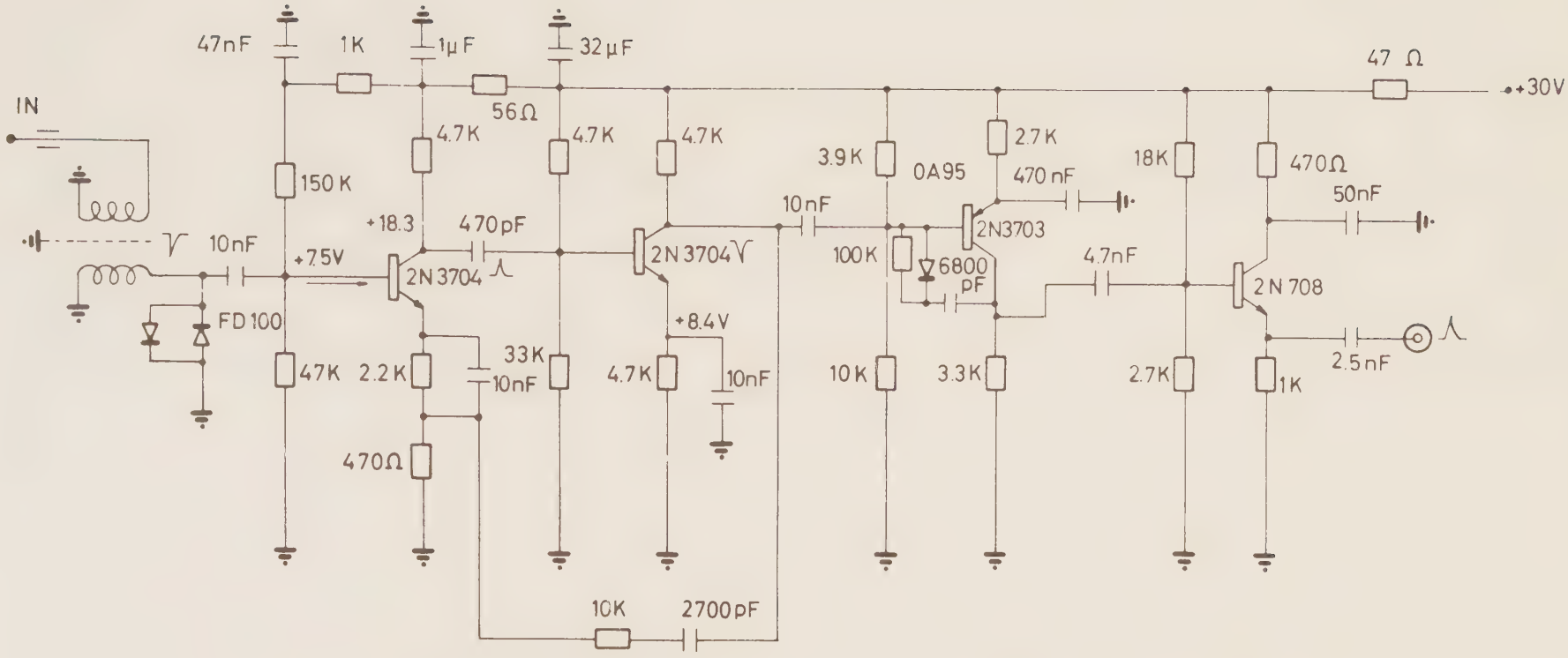

AMPLIFIER FOR MAGNETOSTRICTION

FIG. 34

Fig. 35 : Zero-Crosser.

A zero-crosser is used to obtain a precise centre value of the magnetostrictive signal, i.e. an amplitude-independent spark location. The input stage consists of a differential amplifier which gives a temperature stability needed to keep the tunnel diode polarization constant. The tunnel diode is normally in its lower state, it is triggered to the higher state by the positive part of the differentiated magnetostrictive signal. It is returned to its lower state at the negative part of the same signal. Variation of the input amplitude from 0.2 V to 2 V gives a time shift of 60 to 80 nsec (corresponding to 0.2 - 0.3 mm in spark location).

The signal from the tunnel diode is amplified and differentiated, and the negative part of the resulting signal is removed by a diode. The output signal is 6 V, width 30 nsec, rise-time $\simeq$ 10 nsec, at a load of 50 Ω.

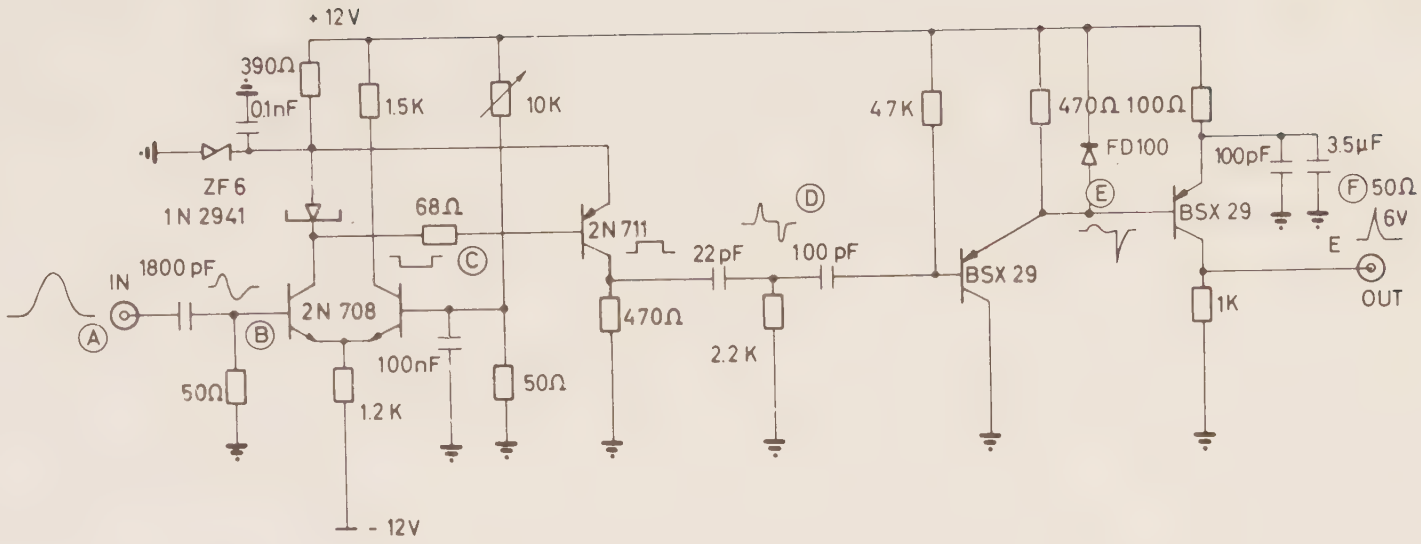

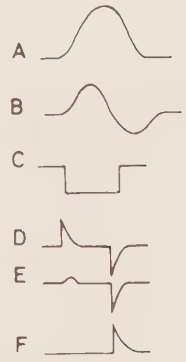

ZERO - CROSSER

FIG. 35

Fig. 36 : Selector.

The selector has the task of switching each magnetostrictive signal to an individual scaler. The selector system allows simultaneous selection of four sparks per coil. Two selector system cards can be connected in series, which then allows the selection of eight sparks per coil.

After ΔT (time between trigger and start) all scalers start counting with 20 MHz. Each magnetostrictive signal stops the clock counting in the corresponding scaler, so that the scaler content is a measure for the geometrical origin of the magnetostrictive signal, e.g. the spark position.

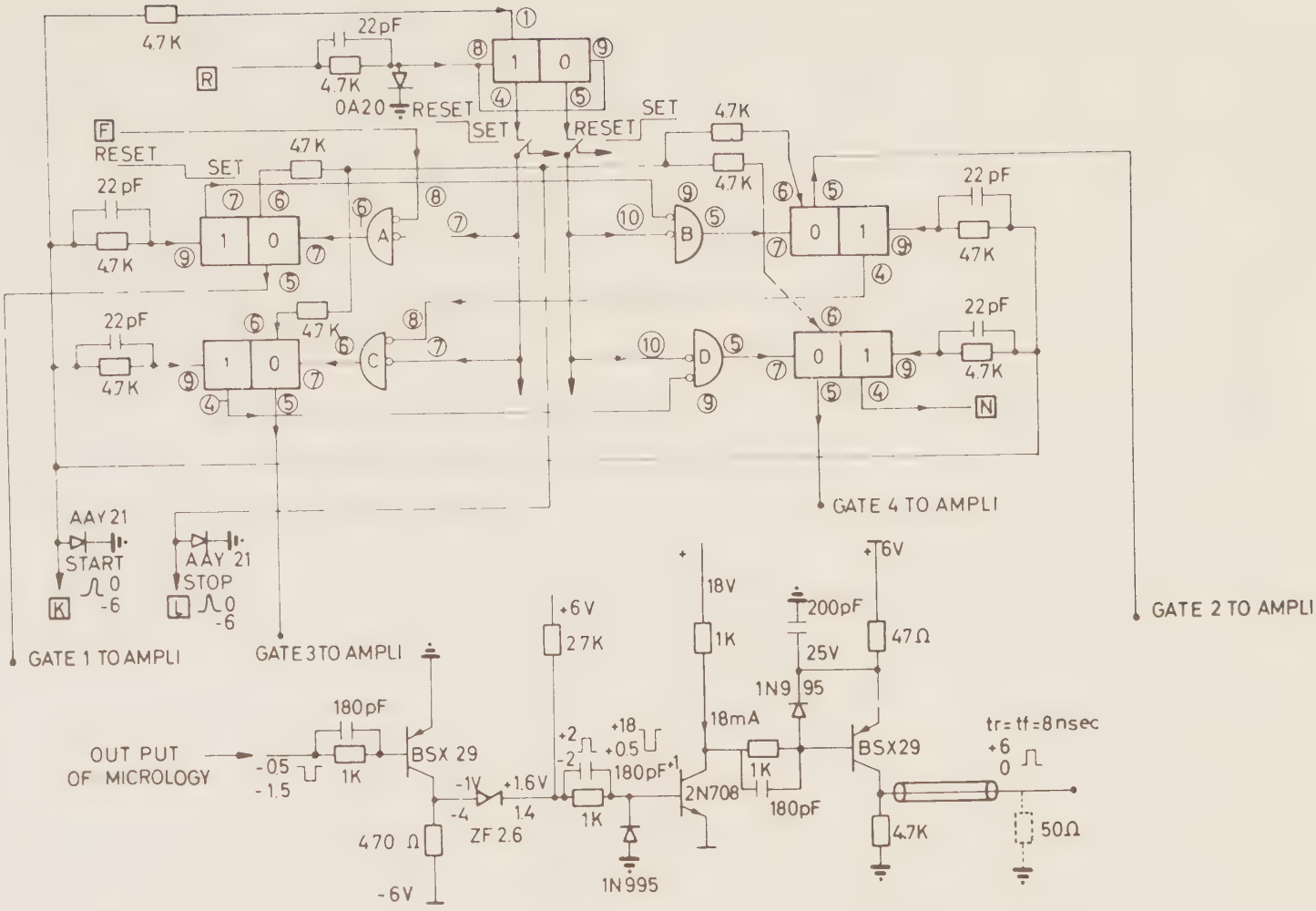

SELECTOR AND OUTPUT UNIT

FIG. 36

Fig. 37 : Time schedule of read-out electronics.

TIME DIAGRAM

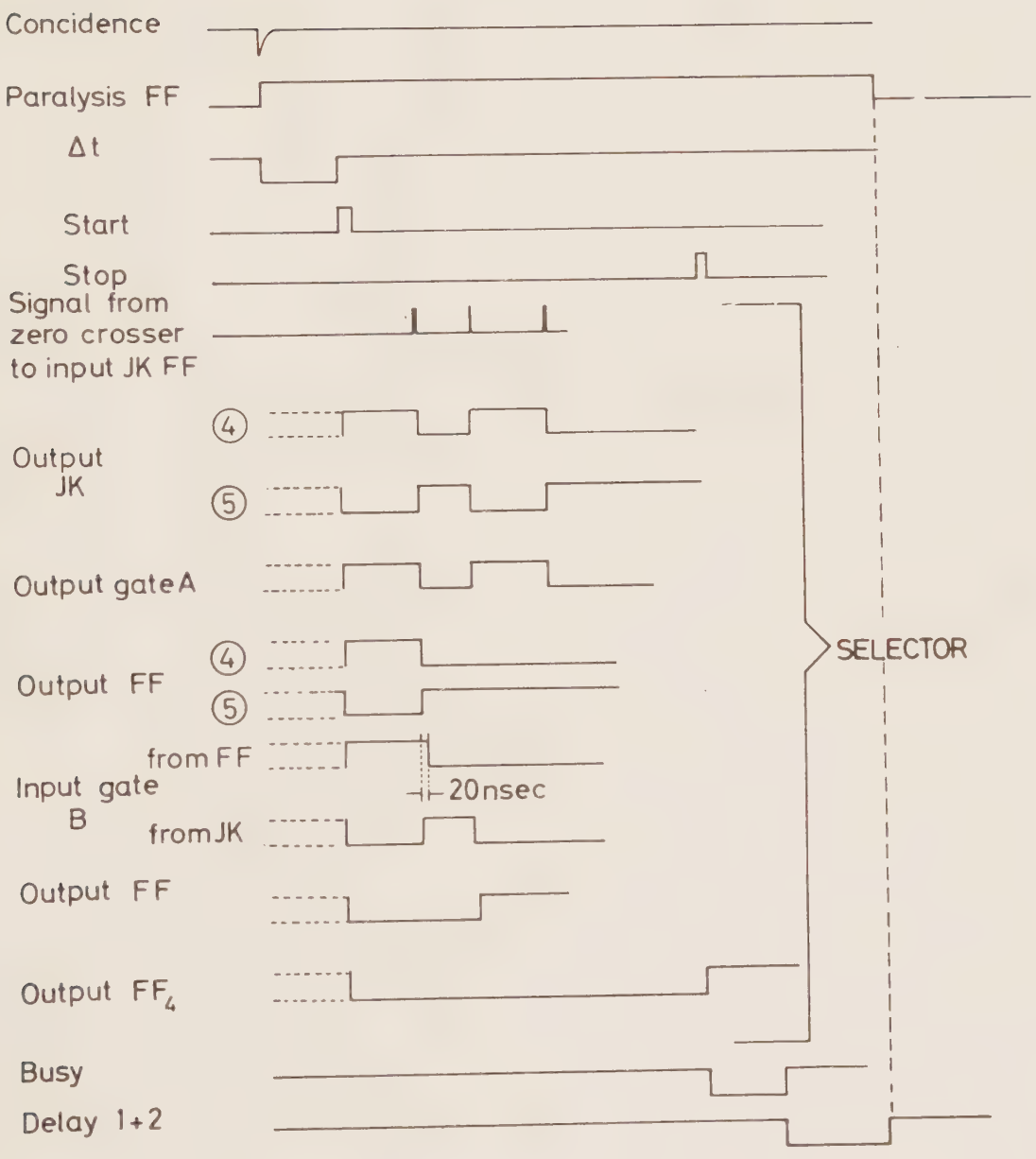

FIG. 37

Fig. 38 : Coordinate system for track reconstruction with the information of two chambers and the vertex. y is coordinate in the beam direction, x and z the two perpendicular ones. Index 0 stands for vertex, indices 1 to 4 for the corresponding four wire planes.

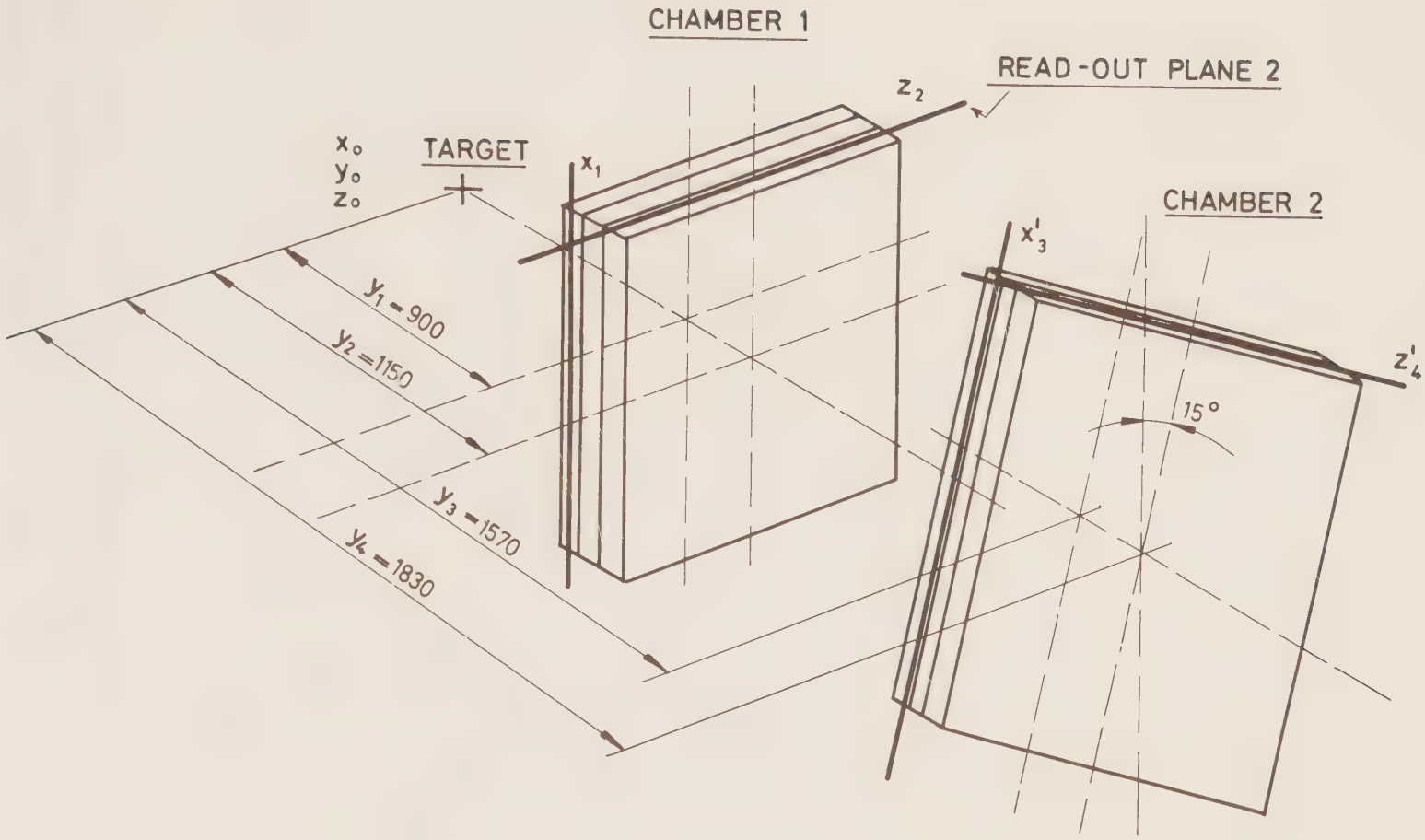
CHAMBER 1
READ-OUT PLANE 2
z_2
x_0
y_0
z_0
TARGET
x_1
CHAMBER 2
x'_3
z'_4
15°
$y_1 = 900$
$y_2 = 1150$
$y_3 = 1570$
$y_4 = 1830$

FIG.38

Fig. 39 : Set-up of CERN boson spectrometer in January 1967 run. In forward direction behind the target, the two wide-gap wire chambers are seen. The first chamber is not centred because of geometrical restrictions.

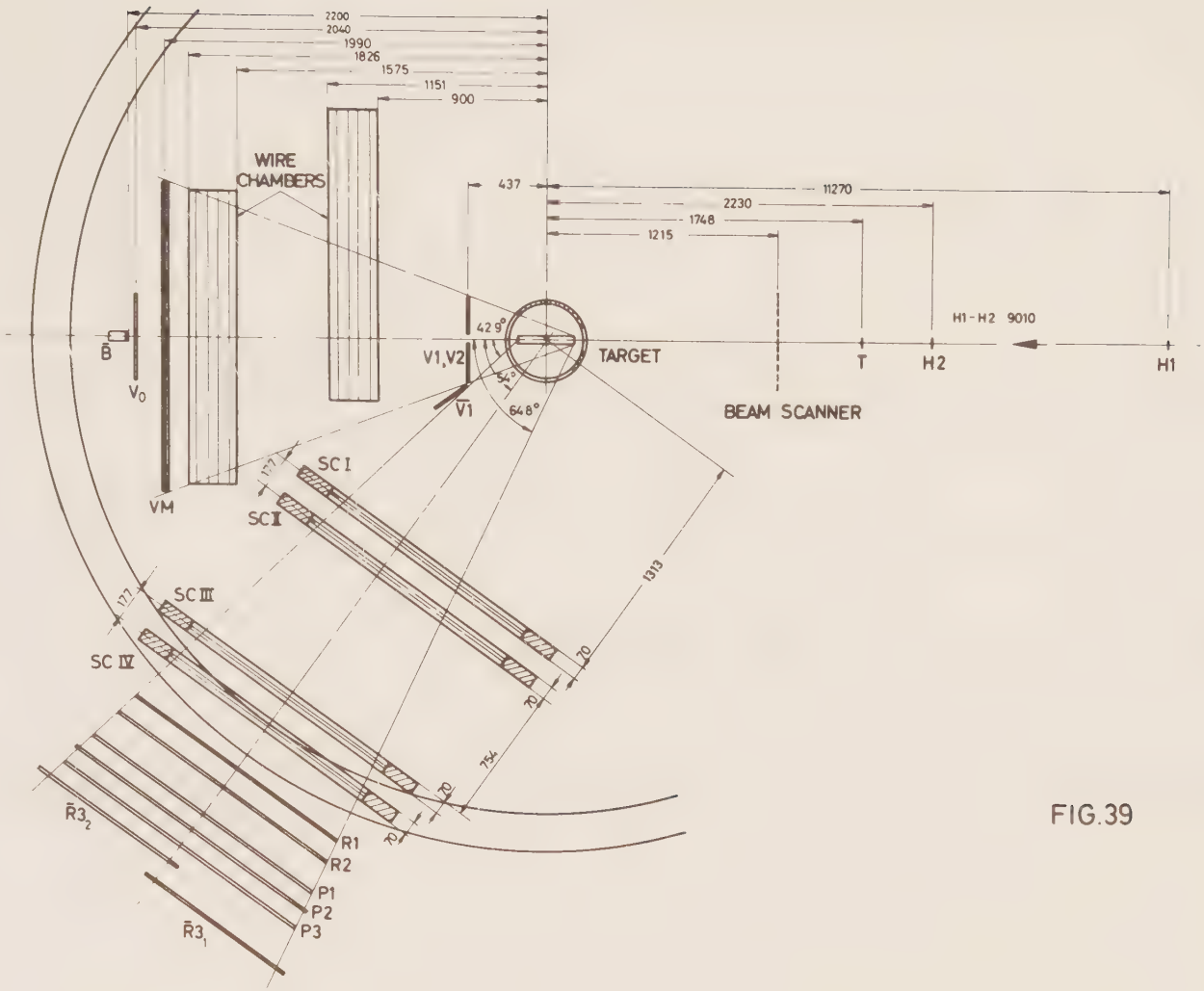
2200
2040
1990
1826
1575
1151
900
WIRE CHAMBERS
437
11270
2230
1748
1215
H1 - H2 9010
42.9°
B
V1,V2
TARGET
T
H2
H1
V0
V1
6.48°
BEAM SCANNER
SC I
VM
SC I
SC III
SC IV
1313
70
754
R̃3₂
R1
R2
P1
P2
P3
R̃3₁

FIG.39

Fig. 40 : On-line print-out for three events. The first eight lines concern the sonic system. The next two lines give the signal coordinates from the two coils in plane one (the second coil has missed one signal). The repeated value 5264 or 5265 is the stop signal. The next two lines give the multiplicity per coil (from coils one to eight). The first figure in the last line of event one is the ΔT value. The rest are computer check-numbers.

FIG. 40

754	2756	1743	1975
3Ø94	3648	541	2Ø75
2Ø99	2ØØ3	1Ø13	3Ø39
2363	1396	13Ø5	37Ø1
3ØØØ3Ø	5ØØ6	4613Ø	4ØØØ4Ø
911Ø3Ø	4ØØØØØ	1Ø2ØØ	111Ø8
12Ø	1Ø4	1ØØØØ	439
121Ø2	11ØØ	1	Ø
4Ø85	417Ø	5264	5264
1363	5264	5265	5264
3376	5265	5264	5264
2118	5264	5264	5265
2847	5265	5264	5266
2698	5264	5264	5264
2246	3133	5264	5264
2277	3164	5264	5264
2	1	1	1
2	1	2	2
725	Ø	2668	4Ø65828

1743	414Ø	2453	9Ø2
1812	4296	2588	787
1621	4314	2823	954
1718	448Ø	2967	88Ø
1Ø4ØØ	Ø	2ØØØ14	Ø
911Ø3Ø	6ØØØØØ	16ØØØ	18155
97	118	1ØØØØ	44Ø
121Ø2	1113	1	Ø
25ØØ	3757	4722	5263
8Ø8	1769	5264	5263
1618	4Ø95	4436	5264
1Ø77	1419	3884	5264
838	4586	5264	5266
962	471Ø	5264	5264
412	37Ø1	5264	5264
171Ø	4997	5264	5264
3	2	3	3
2	2	2	2
725	Ø	2668	4Ø65828

16979	16979	16979	16979
16979	16979	16979	16979
28Ø6	4322	1652	915
2771	414Ø	1439	1138
4ØØØØ2	46ØØ5	Ø	4ØØ4
911Ø6Ø	Ø	1Ø2ØØ	6541
144	122	11ØØØ	44Ø
121Ø2	1124	1	Ø
3889	4Ø17	5265	5264
1515	1632	5264	5264
3289	3412	3751	5265
1763	21Ø2	2226	5264
2Ø7Ø	2642	5264	5267
29Ø4	3477	5265	5264
21Ø5	2347	2553	5265
2853	3Ø61	3299	5265
2	2	3	3
3	2	3	3
725	Ø	2668	4Ø65828

Fig. 41 : The chambers were triggered on beam particles, defined by widely spaced hodoscopes (H1 and H2, Fig. 39). The difference between the positions in the two x-planes is shown. It has a width of ± 1.25 mm.

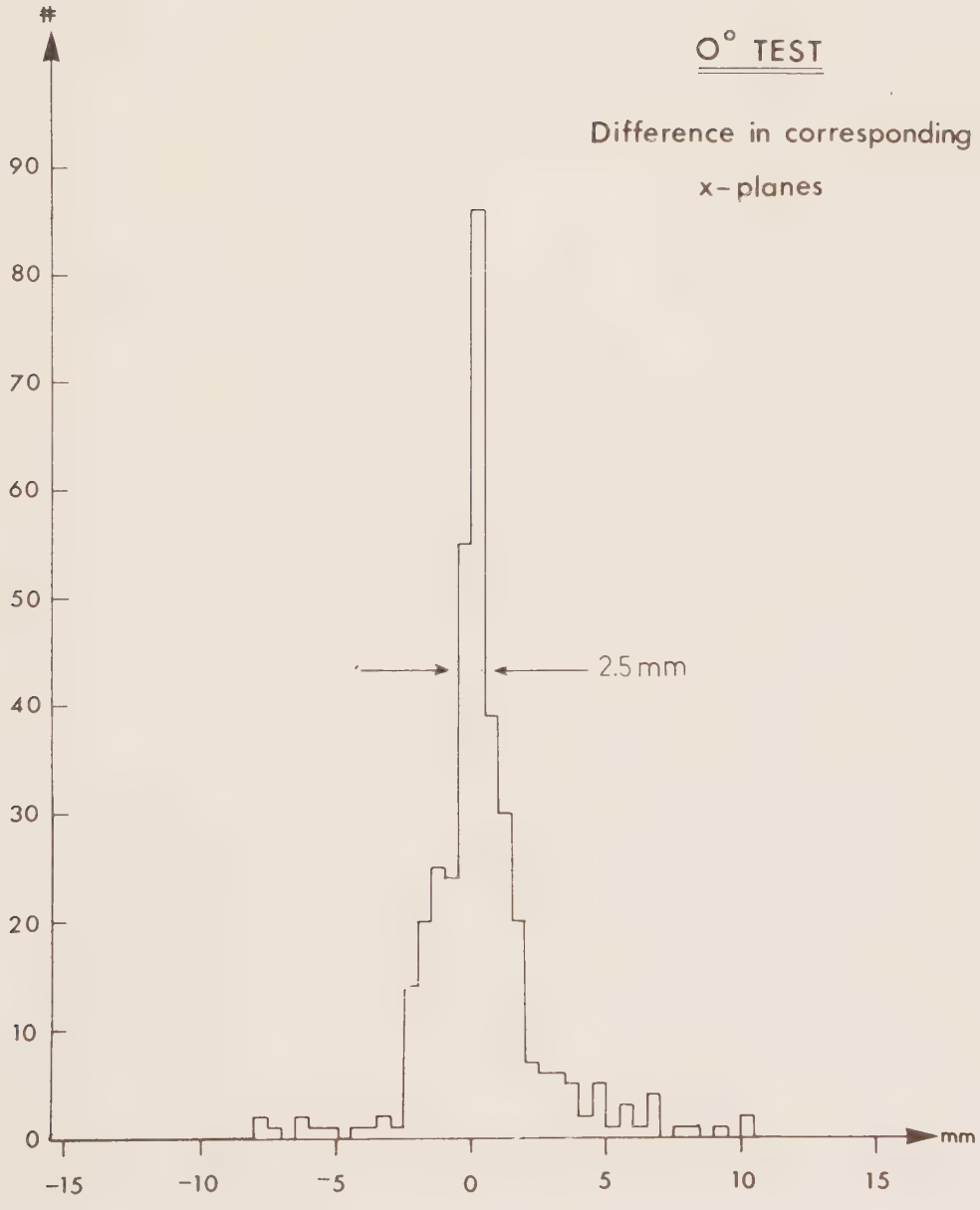
#
0° TEST
Difference in corresponding
x-planes
90
80
70
60
50
40
30
20
10
0
2.5 mm
mm
-15
-10
-5
0
5
10
15

FIG 41

Fig. 42 : The difference between the positions in the two z-planes is shown.
Width = ± 1.25 mm.

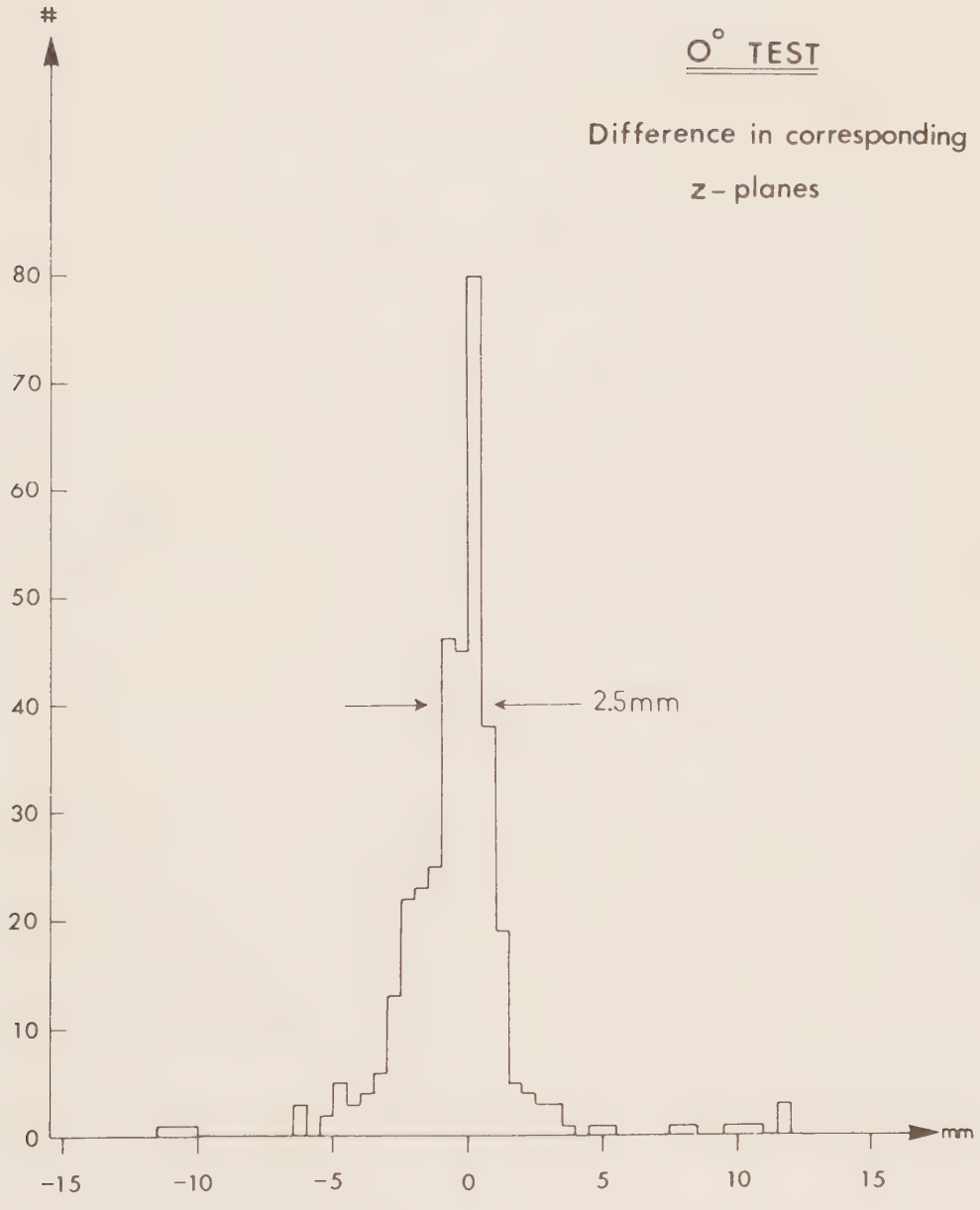
#
0° TEST
Difference in corresponding
z – planes
80
70
60
50
40
30
20
10
0
2.5mm
mm
−15
−10
−5
0
5
10
15

FIG. 42

Fig. 43 : The spectrometer has been triggered on protons in the "elastic angle". The distribution in the first wire chamber of forward-going particles associated with the proton is shown. One can see that most of them are elastically scattered pions.

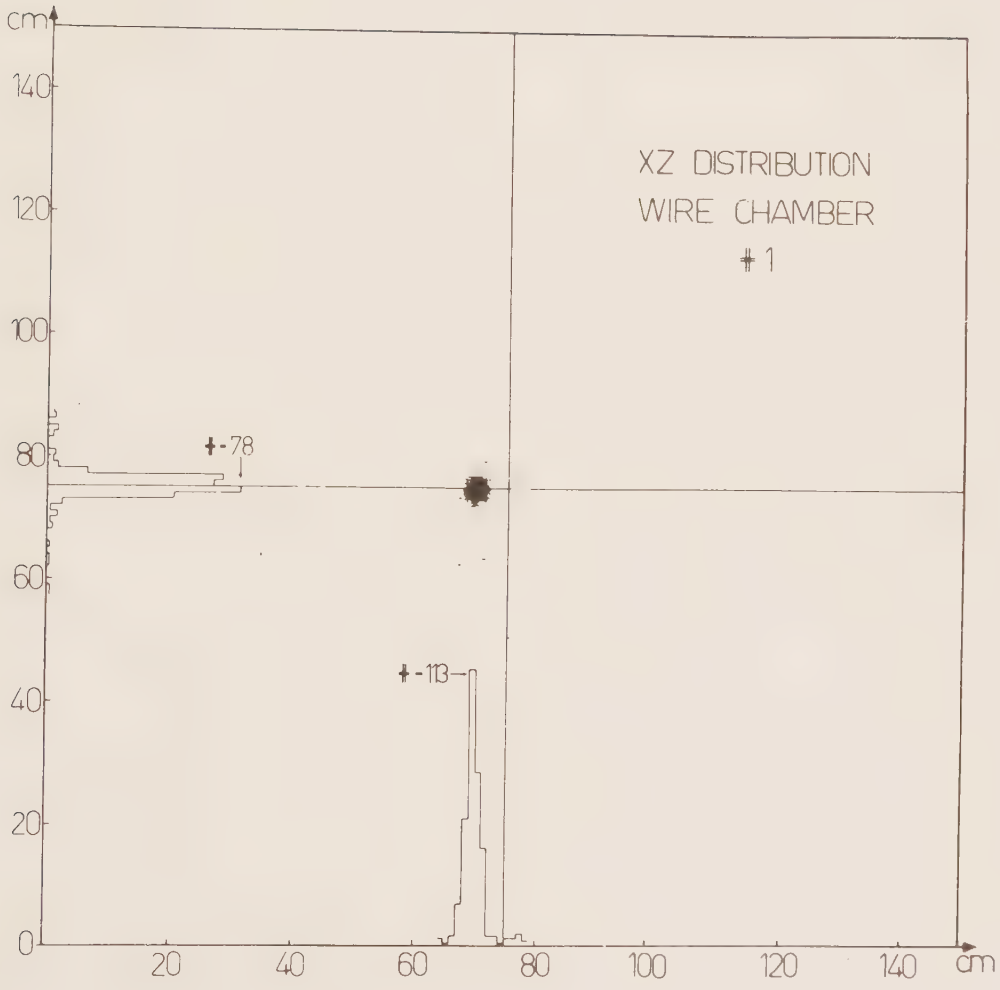
cm
140
120
100
80
60
40
20
0
XZ DISTRIBUTION
WIRE CHAMBER
1
#-78
#-113
20
40
60
80
100
120
140
cm

FIG.43

Fig. 44 : The chambers were triggered on elastic events. The difference between measured and fitted coordinates in the first plane is shown.

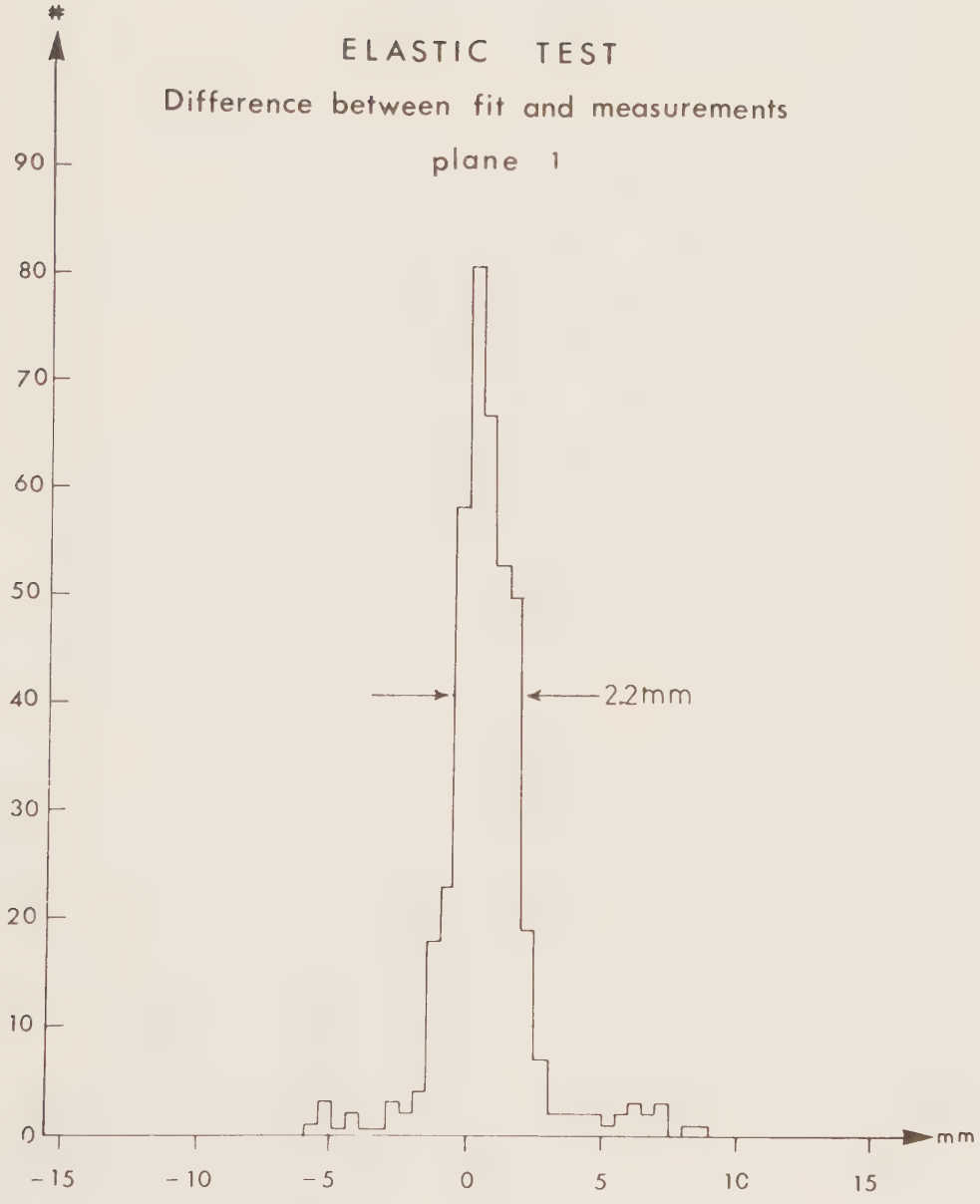
#
ELASTIC TEST
Difference between fit and measurements
plane 1
90
80
70
60
50
40
30
20
10
0
2.2mm
mm
-15
-10
-5
0
5
10
15

FIG. 44

Fig. 45 : Second plane.

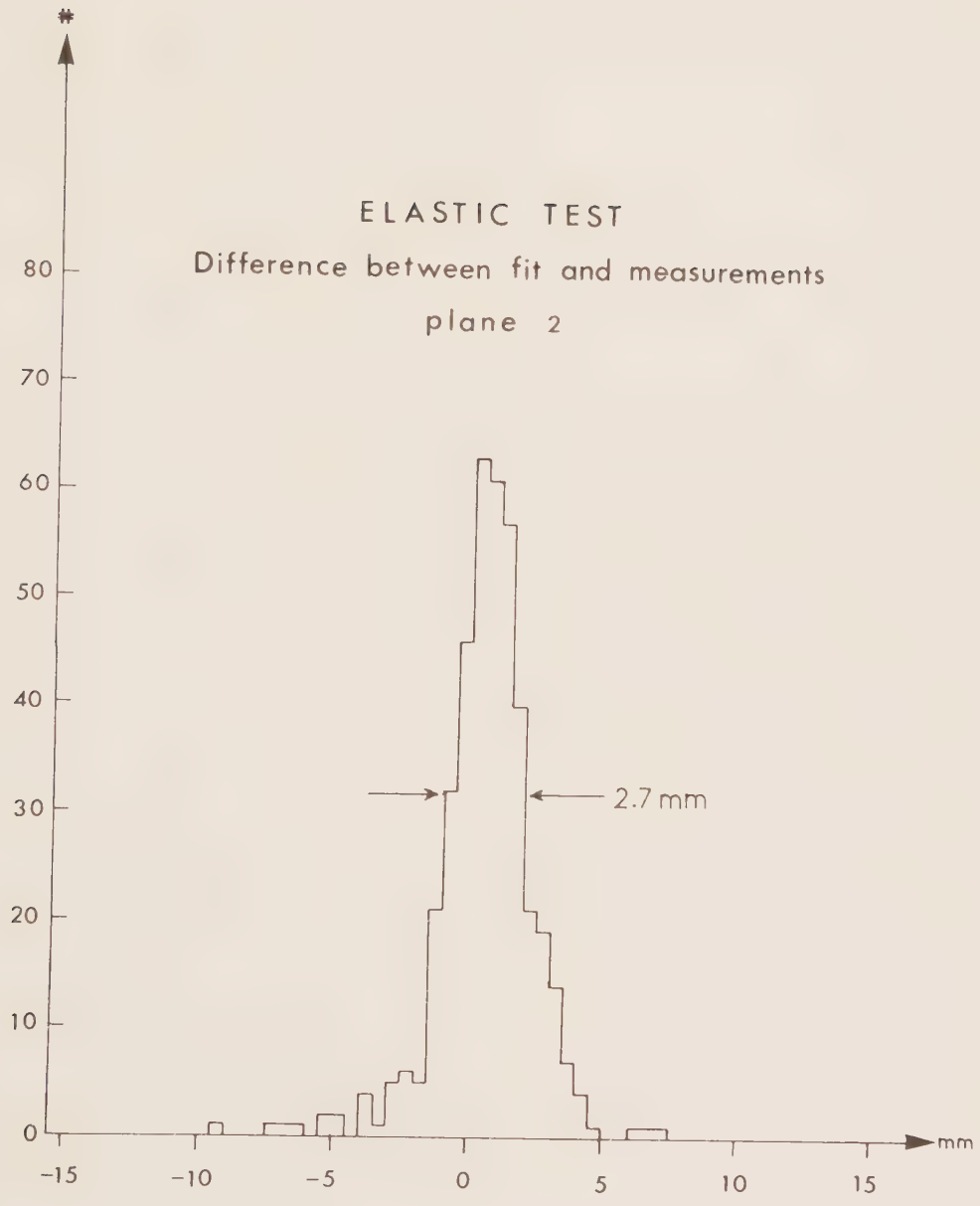
ELASTIC TEST
Difference between fit and measurements
plane 2
*
80
70
60
50
40
30
20
10
0
2.7 mm
−15
−10
−5
0
5
10
15
mm

FIG. 45

Fig. 46 : Third plane.

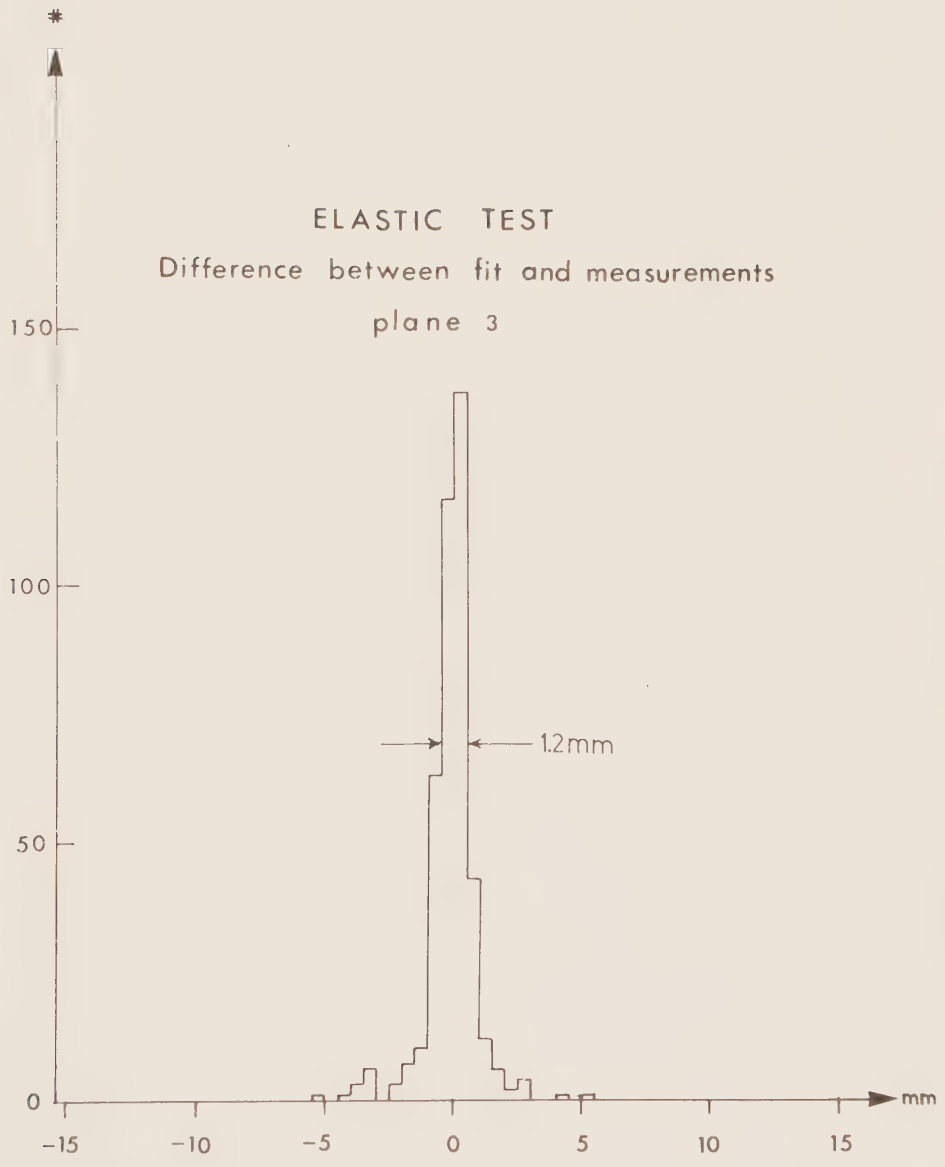
*
ELASTIC TEST
Difference between fit and measurements
plane 3
150
100
50
0
1.2mm
mm
-15
-10
-5
0
5
10
15

FIG. 46

Fig. 47 : Fourth plane.

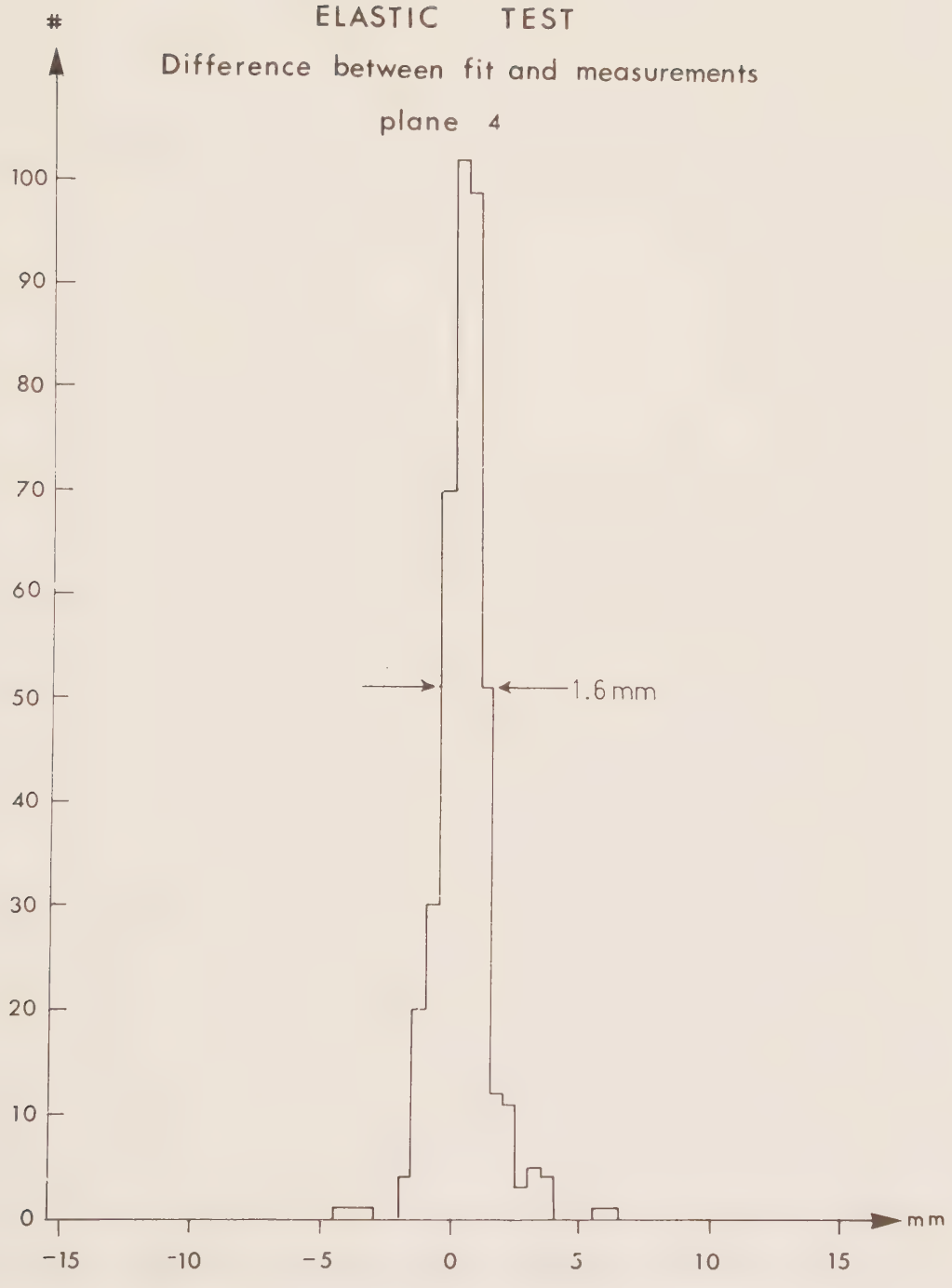
ELASTIC TEST
Difference between fit and measurements
plane 4
#
100
90
80
70
60
50
40
30
20
10
0
1.6 mm
−15
−10
−5
0
5
10
15
mm

FIG. 47

Fig. 48 : The position of the elastic pion in the wire chambers can be calculated from the proton-side information with an error (coming from $\Delta p_1/p_1 = \pm 1\%$ for the incident pion momentum and $\Delta p_3 = \pm 15$ MeV/c for the recoil proton momentum) of ± 2.3 mrad. The difference between calculated and fitted angle is shown, its width is ± 2.0 mrad.

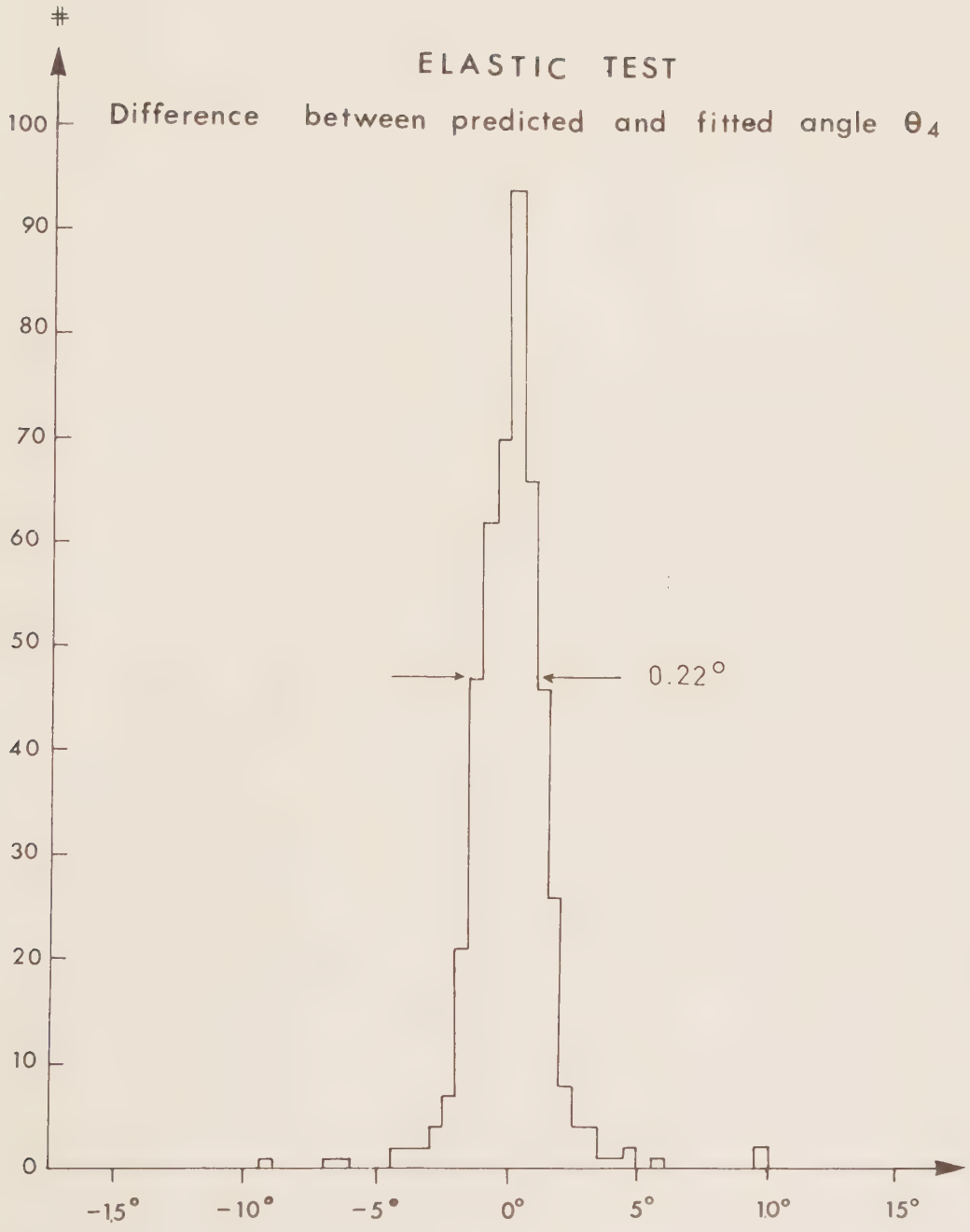
#
ELASTIC TEST
Difference between predicted and fitted angle θ_4
100
90
80
70
60
50
40
30
20
10
0
0.22°
-15°
-10°
-5°
0°
5°
10°
15°

FIG. 48

Fig. 49 : The spark distribution in wire chamber 1 is shown. The cross in the middle indicates the beam centre, the surface inside the circle corresponds to the beam-killer area.

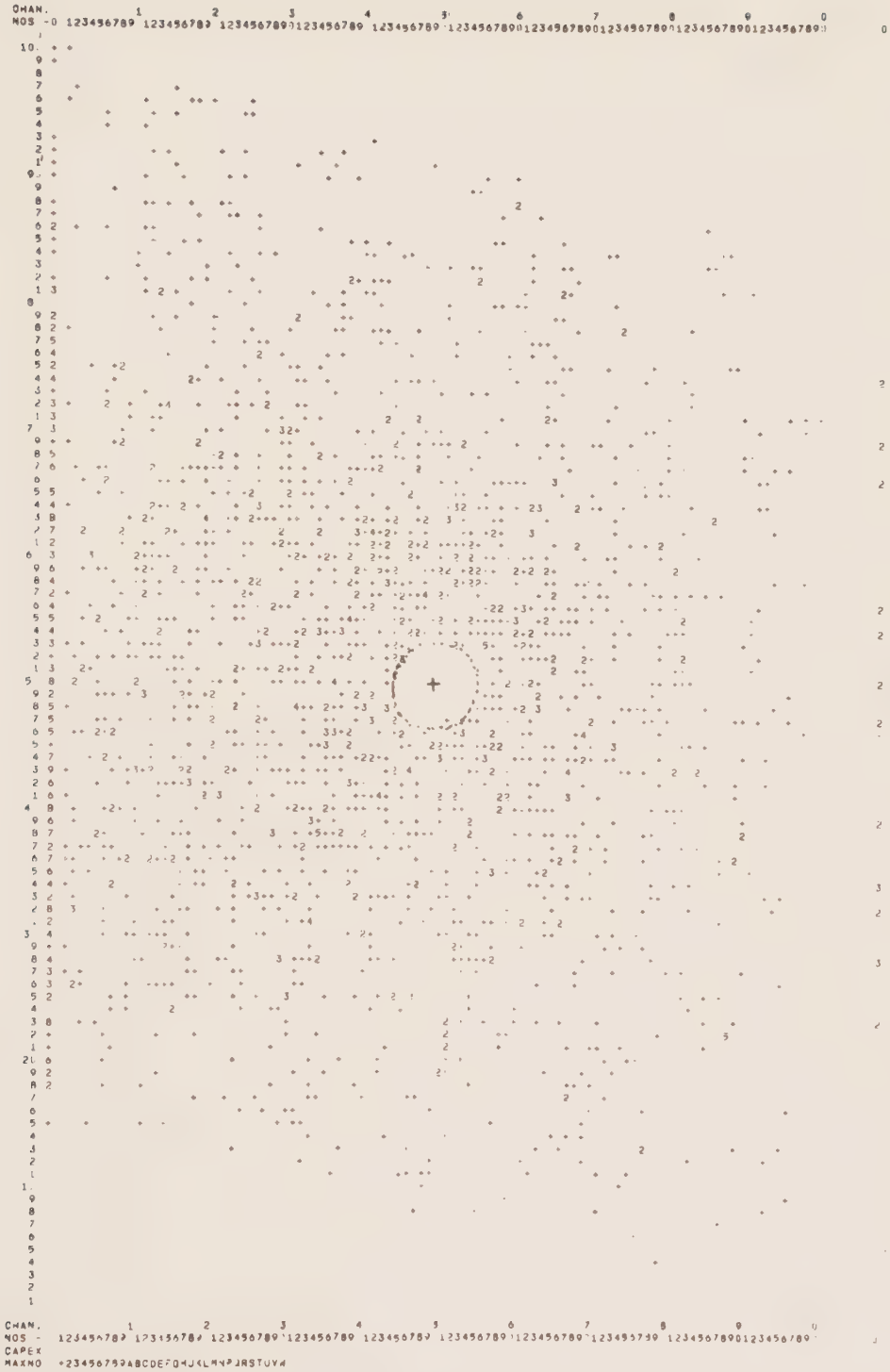

FIG. 49

Fig. 50 : The total energy of the $\pi^- p$ system minus the total energy of the pX^- system — called ΔE — is shown. The events coming from the decay $X^- \rightarrow \pi^+ \pi^- \pi^-$ are found in the peak around $\Delta E = 0$, whereas the other decay modes are in the tails.

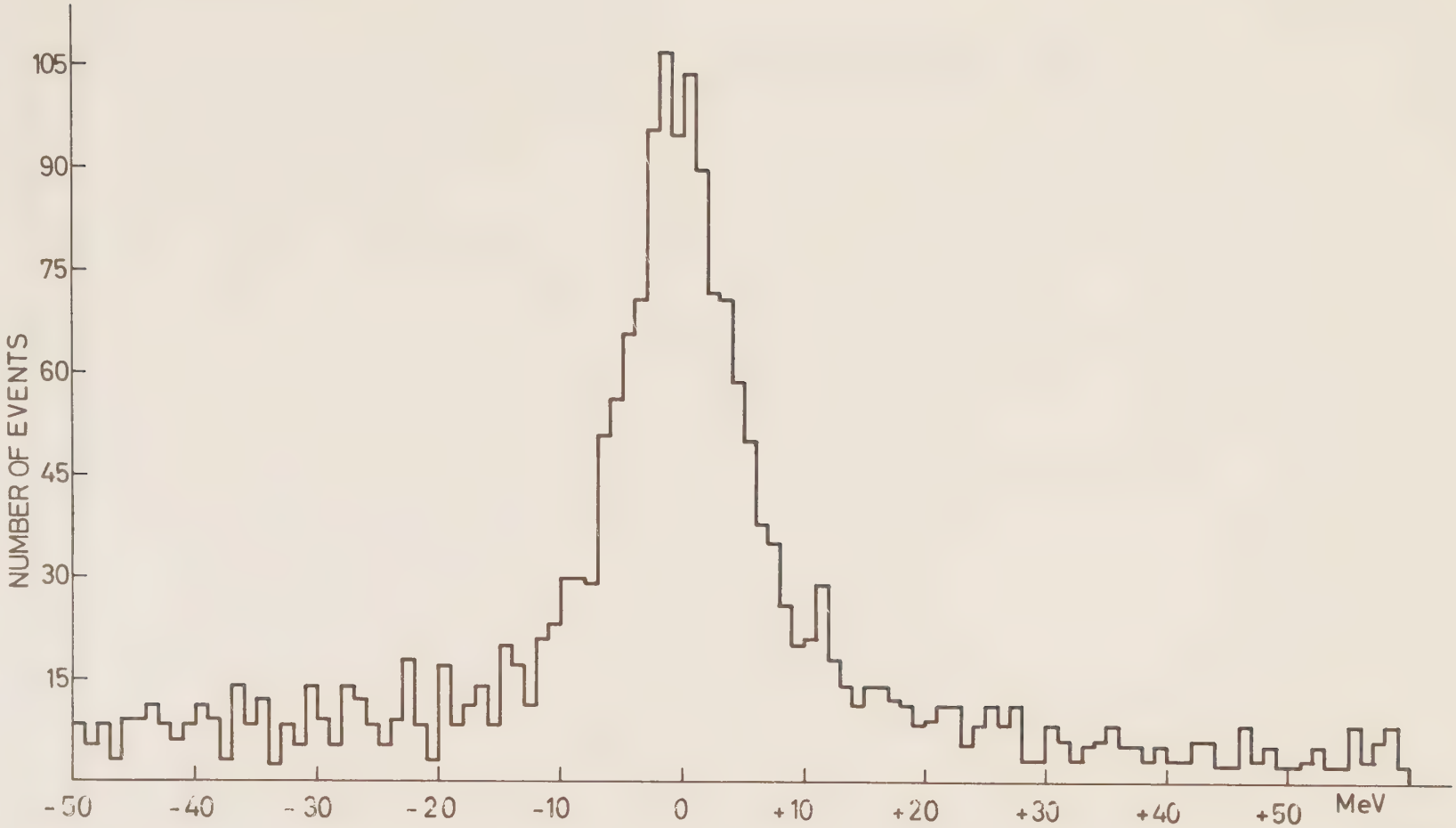
NUMBER OF EVENTS
105
90
75
60
45
30
15
-50
-40
-30
-20
-10
0
+10
+20
+30
+40
+50
MeV

FIG. 50

Fig. 51 : The total sample of registered events shows the A_2 meson on a steeply rising background, interpreted as more than three-pion phase-space.

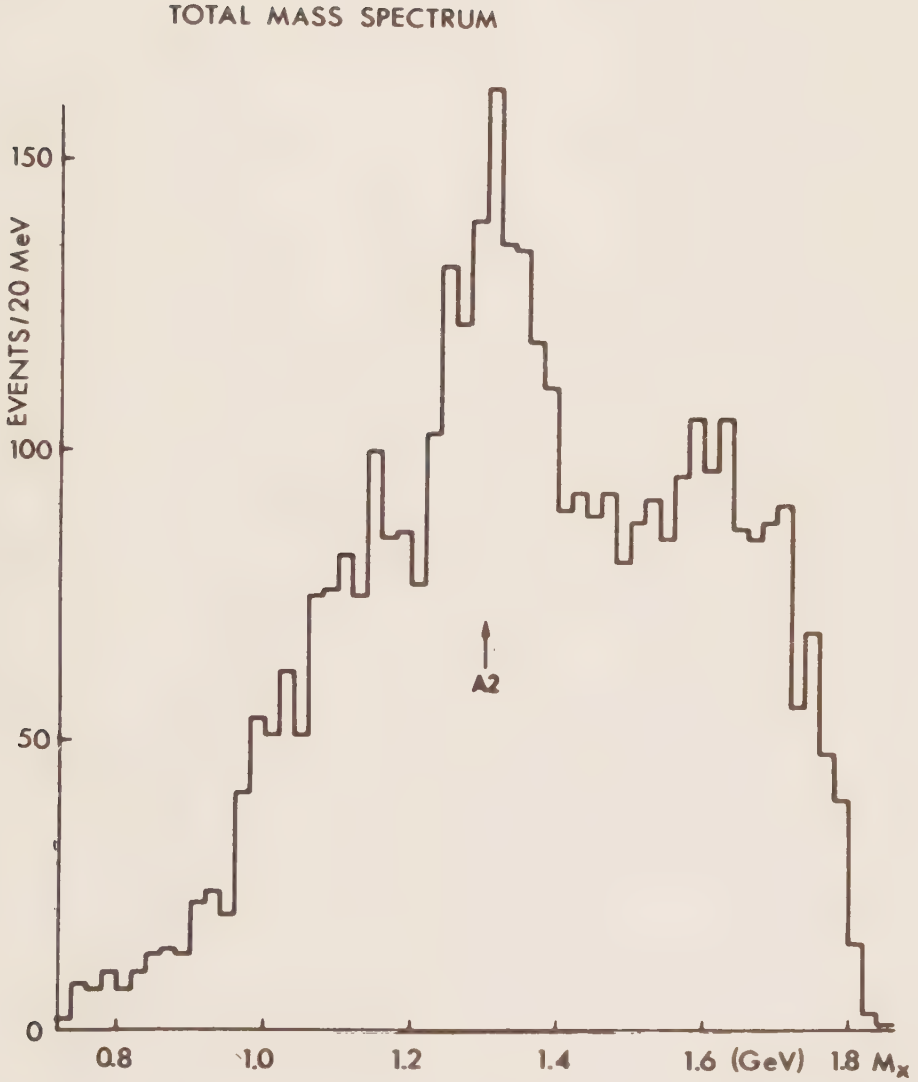
TOTAL MASS SPECTRUM
EVENTS/20 MeV
150
100
50
0
A2
0.8
1.0
1.2
1.4
1.6 (GeV)
1.8 M_x

FIG. 51

Fig. 52 : 401 events survive a χ^2 cut after an all-parameter variation of ΔE.

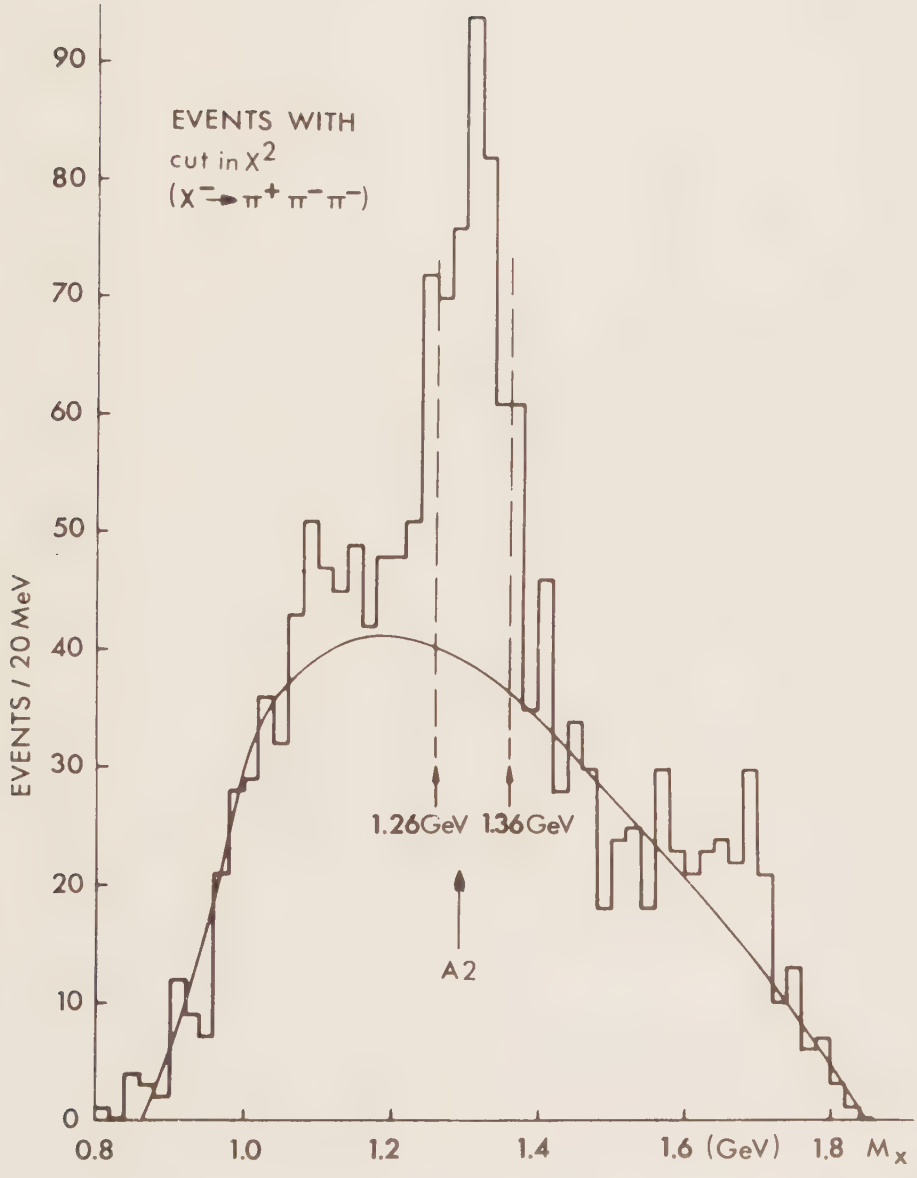
EVENTS WITH
cut in X^2
$(X^- \to \pi^+ \pi^- \pi^-)$
EVENTS / 20 MeV
90
80
70
60
50
40
30
20
10
0
0.8
1.0
1.2
1.4
1.6 (GeV)
1.8
M_X
1.26GeV
1.36GeV
A2

FIG. 52

Fig. 53 : The events cut by χ^2 still show a faint A_2, coming from uncertainties in the cut and possible $K\bar{K}$ decay modes.

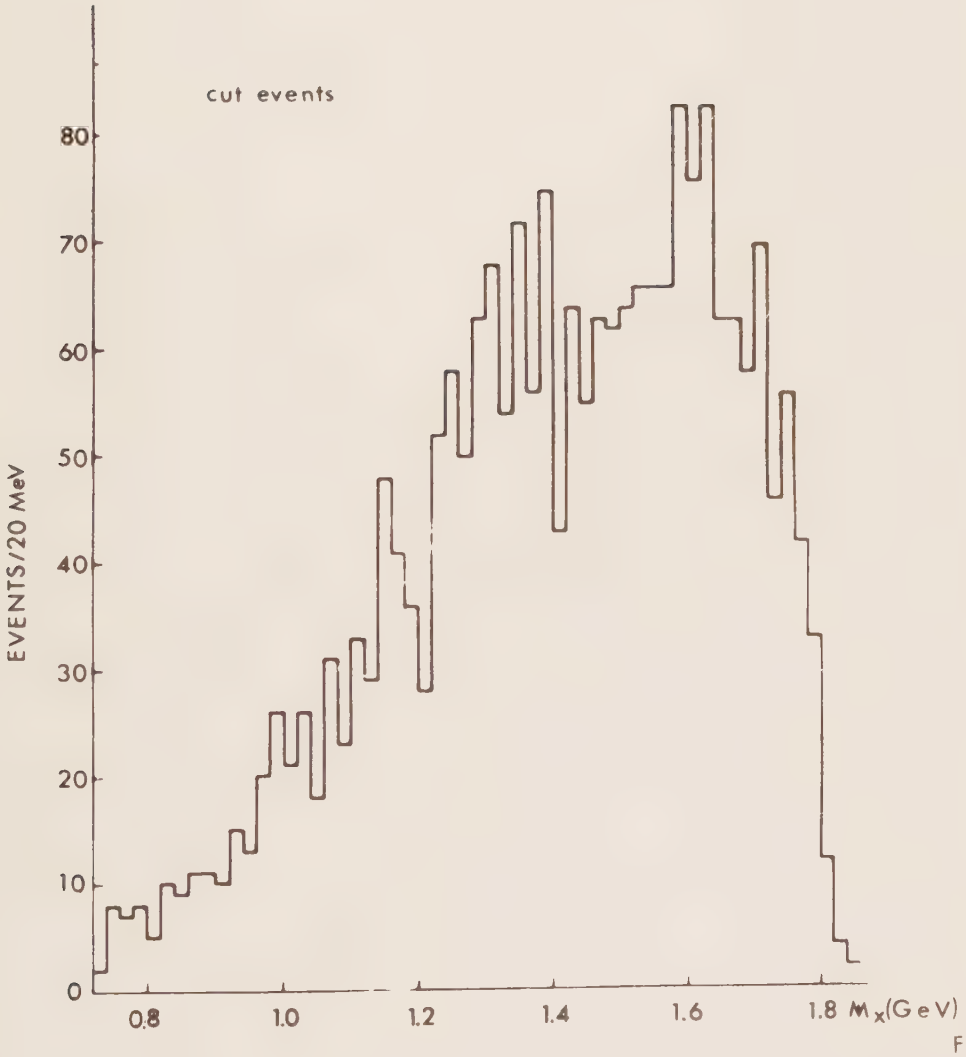
cut events
EVENTS/20 MeV
0
10
20
30
40
50
60
70
80
0.8
1.0
1.2
1.4
1.6
1.8
M_x(GeV)

FIG.53

Fig. 54 A six-folded Dalitz plot for the cleaned sample.

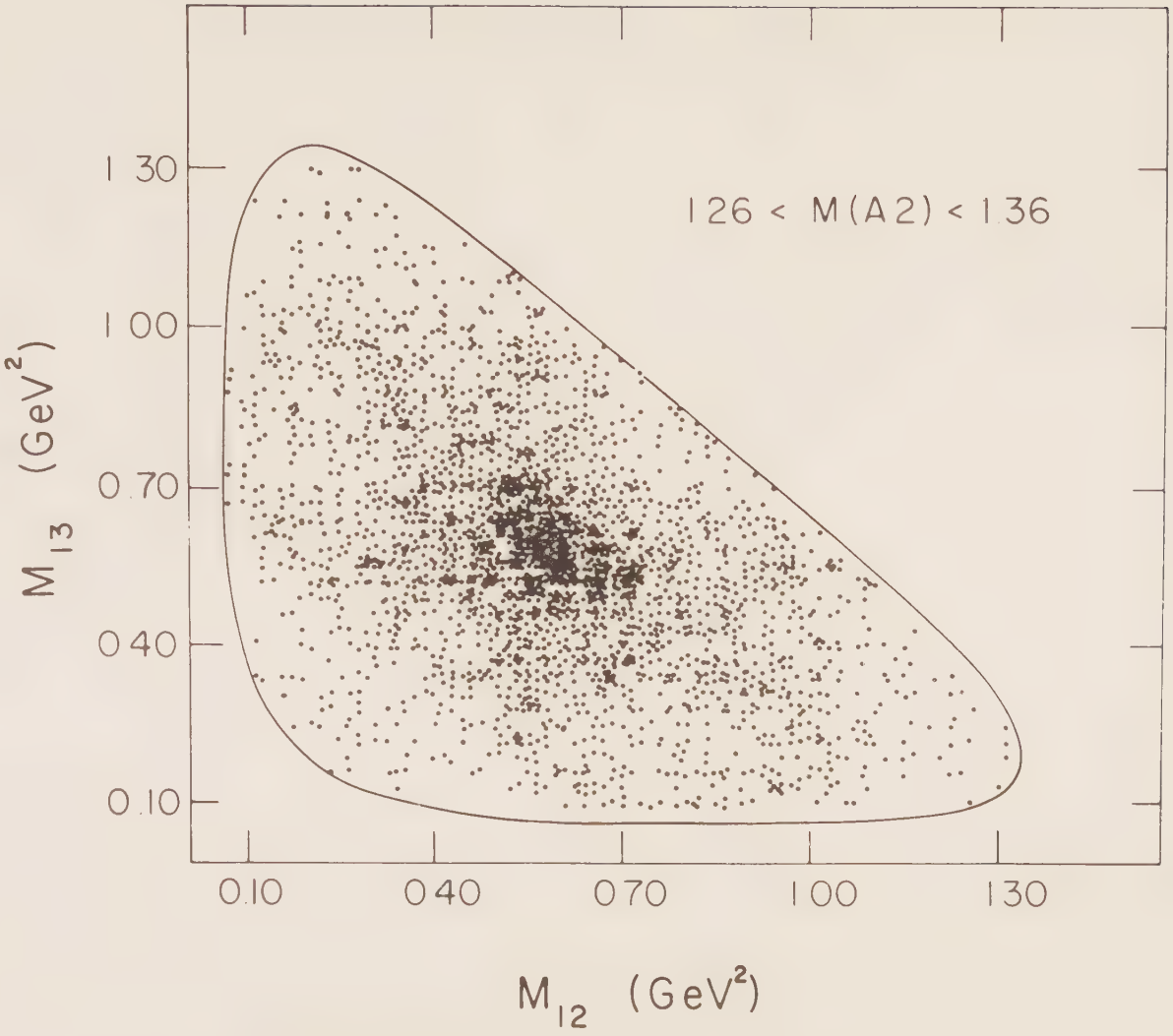

FIG.54 DALITZ PLOT

Fig. 55 : Projection of the six-folded Dalitz plot, showing ρ meson.

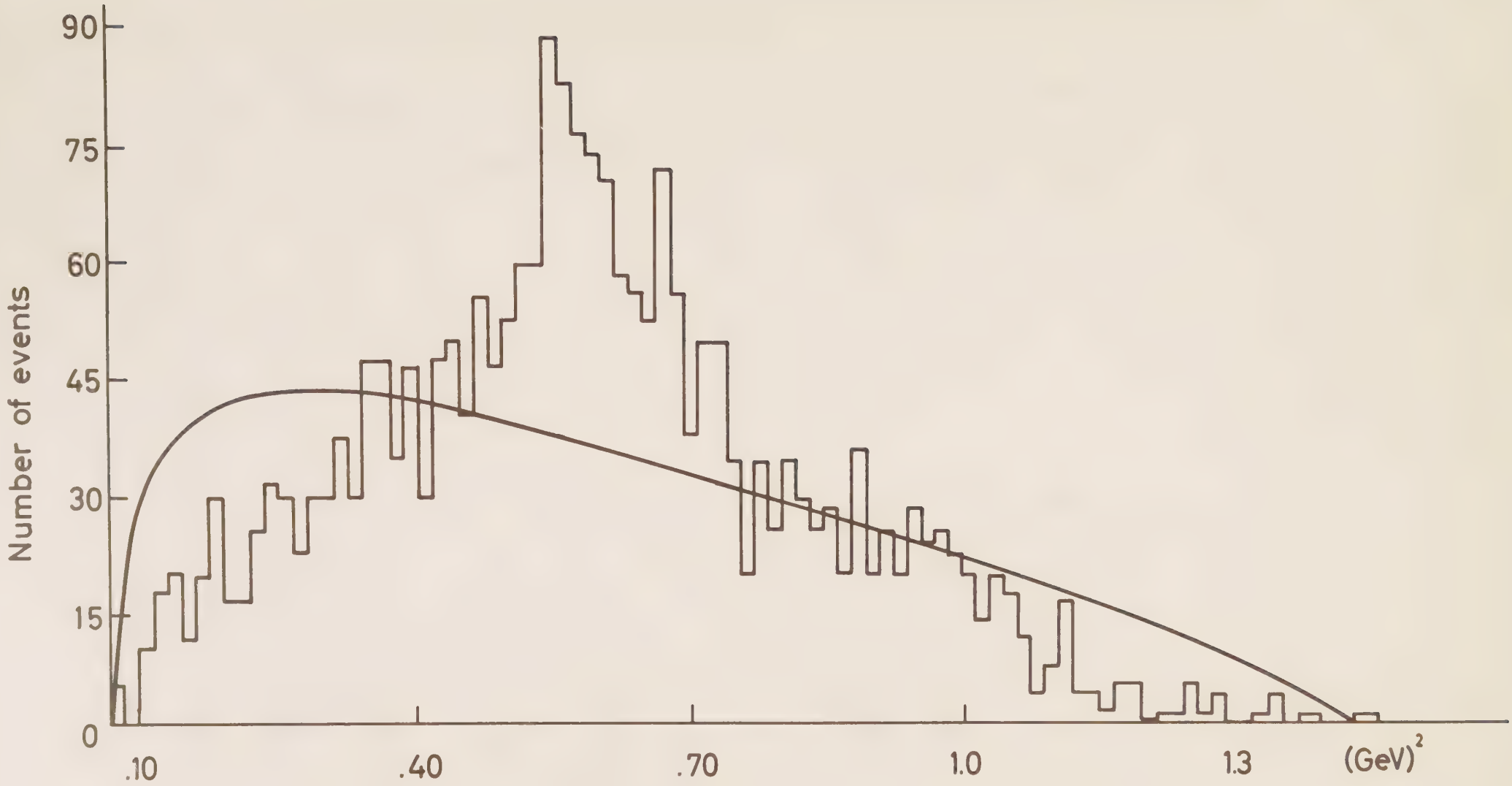

FIG.55

Fig. 56 : Statistical analysis of the Dalitz plot:

a) logarithm of the likelihood values as function of the percentage of resonance and $\rho\pi$ background for $J^P = 2^+$ (left) and 2^- (right);

b) radial density distribution of one sextant of the Dalitz plot, fitted with the theoretical curves for $J^P = 2^+$ [full line with P (χ^2) = 16%] and 2^- [dashed line with P (χ^2) = 0.7%], assuming 50% of resonance.

FIG. 56

STATISTICAL ANALYSIS OF THE DALITZ PLOT

a) MAXIMUM LIKELIHOOD METHOD

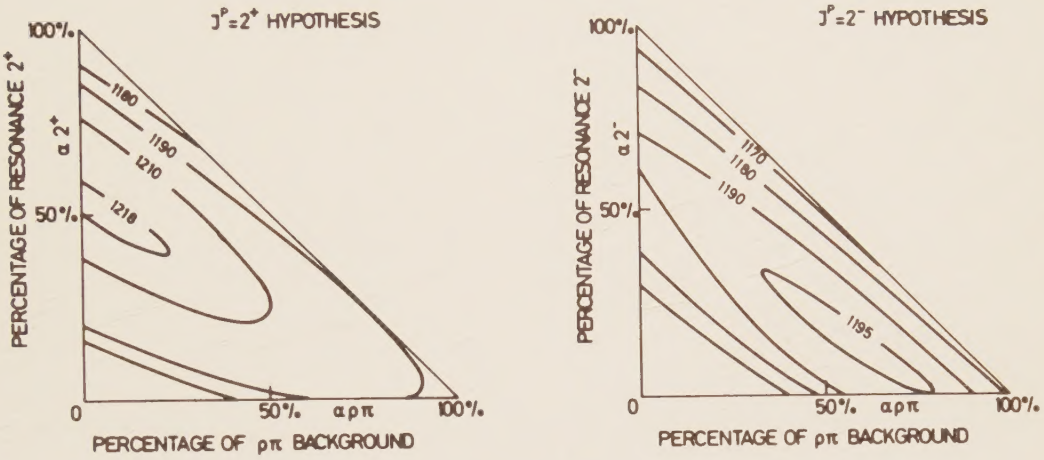

b) X^2 ANALYSIS FOR RADIAL DISTRIBUTION OF ONE SEXTANT